The Effect of Energy Input on the Aggregation Rate in an Oscillating Multi-Grid Reactor

Prepared by
Brian Mathew Willis

A dissertation submitted for the degree of Master of Science in Chemical Engineering

Crystallization & Precipitation Research Unit
Department of Chemical Engineering
Faculty of Engineering and the Built Environment
University of Cape Town

Plagiarism Declaration

1. I know that plagiarism is wrong. Plagiarism is to use another's work and to pretend that it is one's own.
2. I have used the Harvard system for citation and referencing. Each significant contribution to, and quotation in, this report from work, or works, of other people has been attributed, and has been cited and referenced.
3. This report is my own work.
4. I have not allowed, and will not allow, anyone to copy my work with the intention of passing it off as his or her own work.

_____ _____

Acknowledgements

I would like to say the greatest of thanks to Professor Alison Lewis. The guidance and insight which she offered when times were tough and results never made sense were invaluable. Her door was always open for quick and often enlightening unplanned meetings. These would always occur after wrestling with data day in day out and making no tangible progress. She gave me space when I needed it and would apply pressure when necessary.

To Marcos Rodriquez-Pascual, thank you for the hours and hours which you spent in the labs. It was always excellent having you involved in this work as you approached the subject from a different point of view to most others. You were always available for help, and more than glad to do so as well.

The Crystallization and Precipitation Unit could not run without Tracy-Ann Craig and Christine Olsen. Tracy-Ann would make certain I had every and anything I needed to conduct my experiments. She would always be there to reassure us of our work and offer us assistance where ever she could. Christine Olsen, the stationary supplier, the tea and cake, the dinner, the birthday card and the everything for CPU, organiser. The time and effort which she gives to us all in CPU is amazing. Thank you to Christine and Tracy-Ann.

To Michael, Jimmy, Moses, Tim, Craig and Umraan. You are the ones who I would run to when everything was at the worst and nothing would make sense. You too were the people I would share my elation with as well. The hours upon hours we spent together till the birds came up, week in week out, while working on our data or in the labs, will be unforgettable. Your willingness to help out with my work and each others was always appreciated. Thank you for making CPU what it is, a truly special research unit.

Thanks must be given to CPU and the Department of Chemical Engineering for funding the research.

Synopsis

Aggregation is a size enlargement mechanism which can be either desirable or inconvenient depending on the process involved. It involves the coming together or collision of two or more particles to form a larger single particle. It is a mechanism which is poorly understood and much research is still required before the intricacies of the process are fully grasped.

Although it is known that aggregation is influenced by energy input (amongst other factors), the relationship between the two has previously been measured in anisotropic turbulent environments. Thus although aggregation is a function of local energy input, it has yet to be measured in environments where the local energy dissipation is well understood, or else it has been studied in low Reynolds number environments. This thesis aims to address this deficiency by studying the effect of local energy input on the aggregation rate in a well characterised environment of isotropic and homogenous turbulence.

Particle collisions are required to occur before an aggregate can form. If a reactor is running at a low energy input, it may result in a laminar flow regime under which only certain types of collisions are favoured, namely perikinetic collisions (though orthokinetic are possible). At higher energy inputs, in fully turbulent regimes, orthokinetic collisions will dominate and be more frequent.

For an aggregate to form after a collision has occurred, the collided particles need to form a bond or bridge which is strong enough to withstand the hydrodynamic stresses imparted upon them by the liquid. If the shear stresses exceed the strength of the bridge, then particles will be ripped apart and the collision can be considered unsuccessful. The aggregation efficiency is a measure of how often a collision results in an aggregate, and will be dependent on the shear rates generated as a result of energy dissipation.

The turbulence and energy dissipation are defined by the type of reactor used and how the impeller(s) transfer the mechanical energy into fluid. It is important to choose a reactor which can produce a highly turbulent environment, as this will promote collisions, but also a reactor which can effectively and efficiently distributed the energy input throughout the reactor.

Previous studies have taken place in stirred tank reactors, Couette and Poiseuille flow reactors. When studying the effects of shear rates on the aggregation rates, each reactor has advantageous and disadvantageous characteristics.

A stirred tank reactor is one of the most commonly used reactors and is capable of producing very high energy inputs and turbulent flows (especially when baffles are in place). A stirred tank reactor suffers from having regions of extremely high and low energy dissipations. Aggregates are exposed to severe shear forces near to the impeller blades, while dead zones offering very minimal fluid motion also exist limiting the chance of collisions. A Couette flow reactor has a constant shear rate across the reactor while a Poiseuille flow reactor has a well defined velocity profile, hence the shear rate can be calculated easily. Characteristics such as those previously mentioned come at the expense of having to operate at a low Reynolds numbers which result in laminar flow regimes. In comparison, the oscillating multi-grid reactor has the ability to produce nearly isotropic and homogenous turbulence. The energy is dissipated equally through the entire volume of the reactor. In an oscillating mulit-grid reactor, particles experience similar shear forces throughout. Grids of fixed distances apart oscillate on a common shaft to create a highly turbulent environment. The shear rates, generated as a result of the turbulence in an oscillating multi-grid reactor, can be considered analogous to the energy input. It is for these reasons, that the oscillating multi-grid reactor was chosen as the reactor to use for this research, as it satisfies many of the shortcomings of other previously discussed reactors.

Calcium oxalate is used as the test case to determine the effect of shear rates on the aggregation rate. A significant amount of research has been conducted on calcium oxalate, as it forms the main constituent of kidney stones. Calcium oxalate is a salt with a low solubility and a tendency to form aggregates.

Theory and previous research shows that when starting from low shear rates, the aggregation rate will be directly proportional to an increasing shear rate. This is because the aggregation rate can be considered the product of an aggregation efficiency and the collision rate and the collision rate is directly proportional to an increasing shear rate. The aggregation efficiency will remain constant up to a certain shear rate, whereupon the efficiency will decrease with a further increase in the shear rates. The overall effect this has on the aggregation rate with respect to the shear rate, is that there is a linear increase in the aggregation rate up until a maximum is found. At shear rates above where the maximum is found, the aggregation efficiency decrease and the net result is that the aggregation rate decreases. The decrease is observed because the shear forces applied are able to disrupt the temporary bridges formed between collided particles. The particles are not able to spend a sufficient amount of time together to form stable aggregates.

The results from this work show that, at low shear rates of $10s^{-1}$, an aggregation rate constant of $2.52\times10^{-15}m^3.s^{-1}$ was found. The maximum aggregation rate constant was found between $5.37\times10^{-14}m^3.s^{-1}$ and $4.04\pm0.74\times10^{-14}m^3.s^{-1}$ at a shear rates of 40 and $60.1s^{-1}$ respectively. It was also was shown to decrease for higher shear rates. The trends observed in the experimental results are similar to those observed in previous literature. Additional measurement techniques such as optical microscopy and atomic absorption spectrometry were performed on the samples to guarantee the integrity of the data, as well as offer additional insight into the mechanisms involved in the aggregation process. The aggregation rate constants were determined using moments transformations of particle size distributions obtained by using laser diffraction measurement techniques, and an optimisation method to fit an aggregation rate model to the experimental data obtained.

Contents

List of Figures

List of Tables

Nomenclature

Abbreviations

ANOVA Analysis of Variance

ANOVA Analysis of Variance

CSTR Continuous Stirred Tank Reactor

BP Bipyramids

Ca Calcium ion

COD Calcium oxalate dihydrate

COT Calcium oxalate trihydrate

D Dendritic

NY Nylon

OMR Oscillating Multi-Grid Reactor

Ox Oxalate ion

P Platelets

RMS Root Mean Square

rpm Revolutions per minute

Greek Symbols

β_0	Size-independent part of the aggregation kernel	$[m^3.s^{-1}]$
β_0^q	Size-independent part of the aggregation kernel at time q	$[m^3.s^{-1}]$

β_{agg}	Aggregation rate	$[m^3.s^{-1}]$
$\dot{\gamma}$	Shear rate	$[m^2.s^{-1}]$
η	Kolmogorov micro-scale	$[m]$
λ	Taylor micro-scale	$[m]$
μ	Dynamic viscosity	$[kg.m^{-1}.s^{-1}]$
ν	Kinematic viscosity	$[m^2.s^{-1}]$
ψ	Collision effeciency	$[-]$
ψ_0	Packing density (1 - minimum porosity)	[-]
ψ_i	Packing density including the fractal dimension	[-]
ρ	Density	$[kg.m^{-3}]$
τ	Dimensionless time	[-]
τ_n	Residence time	$[s]$
r_{coll}	Collision rate	$[m^3.s^{-1}]$
ϵ	Energy input	$[W.kg^{-1}]$

Roman Symbols

$\boldsymbol{b}$	Body force (gravitational acceleration)	$[m.s^{-2}]$
$\boldsymbol{v}(x,t)$	Velocity	$[m.s^{-1}]$
ΔC	Difference in the concentration and the saturation concentration	$[mg.dm^{-3}]$
$\langle\dot{\gamma}\rangle$	Average shear rate	$[s^{-1}]$
Re_0	Reynolds number for the largest eddy	[-]
Re_α	Reynolds number for the smallest eddy	[-]
St	Stokes number	[-]
C	Concentration	$[mg.dm^{-3}]$
C^*	Saturation concentration	$[mg.dm^{-3}]$

C_1, C_2, C_3	Constants for an oscillating grid	[-]
d_i	Diameter of the i'th particle	$[m]$
d_j	Diameter of the j'th particle	$[m]$
D_f	Fractal dimension	[-]
D_{max}	Max diameter	$[m]$
D_{min}	Minimum diameter	$[m]$
dL	Infinitely small region	$[\#.m^{-3}]$
dN	Total number of particles in the region $[L, L + dL]$	$[\#.m^{-3}]$
f	frequency of oscillations	[Hz]
f_{AR}	Shape factor (Aspect Ration)	[-]
f_{circ}	Shape factor compared to a sphere	[-]
I	Intensity of the measured light	[cd]
i	Index of the i'th particle	[-]
I_0	Intensity of the laser light	[cd]
j	Index of the j'th particle	[-]
J_{ij}^0	Collision frequency	$[m^3.s^{-1}]$
l_0	Charecteristic length of the largest eddy	$[m]$
l_α	Charecteristic length of the smallest eddy	$[m]$
L_i, L_{i+1}	Size interval of the i'th and i'th+1 bin	$[m]$
M	The mesh size of an oscillating grid	$[m]$
m_0	Zeroth moment, total number of particles	$[m^0.m^{-3}]$
m_0^q	Zeroth moment at time q	$[m^0.m^{-3}]$
m_1	First moment, total number of surface area	$[m^1.m^{-3}]$
m_2	Second moment, total suface area of particles	$[m^2.m^{-3}]$

m_3	Third moment, total volume of particles	$[m^3.m^{-3}]$
m_j	j'th moment	$[m^j.m^{-3}]$
n	Number density function	$[\#.m^{-3}]$
n_0	Number of particles at t_0	$[\#.m^{-3}]$
n_i	Number of particles in the i'th bin	$[\#.m^{-3}]$
n_j	Number of particles in the j'th bin	$[\#.m^{-3}]$
n_{tot}	Number of particles	$[\#.m^{-3}]$
R	Collision radius of a sphere	$[m]$
r_i	Radius of the i'th particle	$[m]$
r_j	Radius of the j'th particle	$[m]$
S	Stroke length, the amplitude of the oscillations	$[m]$
s	Dimensionless volume averaged shear rate	[-]
t	time	$[s]$
t_α	Charecteristic time	$[s]$
u_0	The horizontal component of the velocity around an oscillating grid	$[m.s^{-1}]$
u_0	Charecteristic velocity of the largest eddy	$[m.s^{-1}]$
u_α	Charecteristic velocity of the smallest eddy	$[m.s^{-1}]$
w_0	The vertical component of the velocity around an oscillating grid	$[m.s^{-1}]$
z	The distance from an oscillating grid	$[m]$
p	Pressure	$[kg.m^{-1}.s^{-2}]$
A	Absorbance	[-]
B	Birth rate	$[m^{-1}.m^{-3}.s^{-1}]$
D	Death rate	$[m^{-1}.m^{-3}.s^{-1}]$
G	Growth rate	$[m.s^{-1}]$

L	Charecteristic length	$[m]$
M	Molar concentration	$[mol.m^{-3}]$
Re	Reynolds Number	[-]
U	Charecteristic velocity	$[m.s^{-1}]$

Mathematical Symbols

$\frac{D}{Dt}$	Material derivative	$\frac{D}{Dt} = \frac{\partial}{\partial t} + \boldsymbol{v} \cdot \nabla$
∇	Gradient	
div	Divergence	

Chapter 1

Introduction

This thesis primarily presents an investigation into the aggregation of micron-scale particles of slightly soluble salts. Aggregation is a size enlargement mechanism for particles. It can be considered a coming together of particles to form a new larger particle. Aggregation as compared to agglomeration should be considered the stronger of the two mechanisms. Aggregation involves the cementing of two or more particles together, whereas agglomerates only results in the weakly coming together of particles and which can be easily disrupted by hydrodynamic forces. Particle aggregation and the mechanisms which causes aggregation to occur are important to a wide range of processors and industries, so this forms the main driving force for this type of research. A fundamental understanding of the processes involved during aggregation and having the ability to make accurate predictions of the size of the aggregates formed given a particular criterion such as the energy input can only be beneficial when wanting to apply the concepts to different systems. Turbulence within a reactor has a significant effect on how often particles collide, the types of collisions as well as whether an aggregate will be formed as a result of the collisions. With this in mind, the type of reactor and energy input will determine the nature of the turbulence. For this study into the aggregation rate of calcium oxalate, an oscillating multi-grid reactor will be used. The oscillating multi-grid reactor was specifically chosen because of its ability to produce nearly homogenous and isotropic turbulence, which is considered an ideal environment for to facilitate the aggregation of particles. Varying the energy input into the system, will allow for the quantification of the effects of shear rates on the formation of aggregates.

1.1 Scope and Overview

Aggregation is a size enlargement process which has numerous applications in many industries. It is however not very well understood, and often difficult to measure and quantify

results. Factors such as the temperature, supersaturation, ion ratios and well as energy input can all have effects on the rate of aggregation and the type of aggregate formed. In this investigation into the aggregation rate of a slightly soluble salt. Only the effect of the energy input (and as an analogy, the shear rate) on the rate of aggregation will be considered. The energy input and shear forces within a reactor define the types of fluid flows and turbulence produced. The reactor design plays a significant part on the energy dissipation as well. The turbulence effects the rate of collisions, as well as the efficiency of the collisions, and hence the aggregation rate as well. This can be summarised in the following simple expression,,

$$r_{agg} = \psi r_{coll}. \tag{1.1}$$

The number of collisions multiplied by the efficiency of the collisions will results in an aggregation rate. Previous studies have been limited to reactors such as stirred tank reactors (STR)s, Couette and Poiseuille flow reactors. STRs are not ideal reactors as they produce shear rates ranging from very high to very low. Particles within the solutions are subjected to vastly different forces dependent on their location. The Couette and Poiseuille flow reactors have very poor mixing as they have to operate at low Reynolds numbers.

For these reasons it was concluded that the oscillating multi-grid reactor (OMR) should provide an excellent environment to study the effects of energy input on the aggregation rate of precipitates from solution because of its ability to produce nearly homogenous and isotropic turbulence throughout the reactor. The energy input of the OMR can be changed by adjusting the frequency at which the grids oscillate. The higher the frequency the higher the energy input. Changing the energy input affects the nature of the turbulence and also how the suspended precipitates move within the system. Intuitively, at high energy inputs the turbulence becomes more chaotic and the particles in the solution will bump into each other more often than when compared to lower energy inputs. This does not imply that the aggregation rate will increase *ad infinitum* as the energy input increases, since beyond a certain energy input, the efficiency, ψ, will decrease. For two particles to aggregate they need to come together and then spend enough time near one another to form a physical bond (bridge). High energy inputs result in high shear forces and shear forces have the ability to easily disrupt the building of such a bond between two collided particles. There should exist an optimum energy input where the number of collisions and the building of the bonds between particles are balanced in such away that the aggregation rate is maximized in the OMR. The aggregation rate constant of calcium oxalate was determined. There is a wealth of literature on calcium oxalate as it is the main component of kidney stones. The aggregation rate of calcium oxalate monohydrate

(COM) has been studied in both in a Poiseuille and Couette flow reactors as well as STRs.

A study into the aggregation rate of calcium oxalate was conducted in the OMR. Particle size distributions were measured and analysed to determine the aggregation rate constant, among other factors as well. Additionally, techniques such as optical microscopy and atomic absorption spectrometry were used to provide additional information into the mechanisms involved in the aggregation of particles.

Chapter 2

Literature Review and Theory

To obtain a complete understanding of the effects of a varying energy input on the aggregation rate of a slightly soluble salt in a particular reactor, various subjects need to be investigated before hand. A few of these topics will be discussed in detail in this review of the past literature. To develop the understanding of the systems and processes which result in aggregation, we need to first consider how turbulence is defined, and as a result of the turbulence in a system, how suspended particles will interact. Therefore the first few sections of the literature review will cover some theory on turbulence, laminar and turbulent flows, how energy is dissipated in a turbulent system, and the possible kinetics of particles suspended in solution. This will lead to some of the potential mechanisms for aggregation to occur as well. Energy dissipation and the type of turbulence vary greatly between different types of reactors, therefore it is also necessary to understand how the reactor type can effect the type of turbulence produced. The reactor type will also then have an effect on the aggregation rate. A study on calcium oxalate, and the various factors which influence the precipitation and aggregation of calcium oxalate will be investigated. Calcium oxalate is one of the slightly soluble salts which has been used to study aggregation rates in the past. Finally some consideration will be given to the various measurements techniques which are available to aid in the understanding of this system. It is necessary to consider the advantages and disadvantages of one method over another, as well as have a detailed understanding of the underlying technology and theory which these methods implement.

2.1 Turbulence

Turbulence and turbulent flows are present and observable every single day. They can be felt as the wind rushing between buildings and seen when stirring a pot of soup. Turbulent flows are also essential in industrial applications, namely that of effective and efficient

mixing and increasing gas transfer rates. Turbulence can be understood as a concept by the layman, however it is certainly not a simple concept to model. Highly turbulent environments are difficult to accurately predicts and model, and only the simplest problems have analytical solutions.

2.1.1 The Navier-Stokes equations for momentum and mass conservation

In general any flow can be defined by its velocity profile, $\mathbf{v}(x,t)$, $(m.s^{-1})$ which varies with both position and time. Through the application of the laws for the conservation of momentum and mass, equations such as the Navier - Stokes equation were defined. The Navier-Stokes equation can accurately predict simple flows. For incompressible Newtonian fluids, the following partial differential equation can be found,

$$\rho\frac{D\mathbf{v}}{Dt} = -\nabla p + \mu\nabla^2\mathbf{v} + \mathbf{b}, \tag{2.1}$$

where ρ $(kg.m^{-3})$is the density , μ the dynamic viscosity, p $(kg.m^{-1}.s^{-2})$ is the pressure and $\mathbf{b}$ $(m.s^{-2})$ is known as the body forces, such as gravity . The fluid defined in this manner is considered to be a continuum, where the bulk properties also apply to infinitesimally small volume as well. The second equation which needs to be considered is that of the conservation of mass. This simply states, that if a cube of fixed size is defined within the fluid volume, then the rate at which the mass changes will be equal to the sum of the mass entering or leaving the volume through all the sides of the cube.

$$\frac{\partial\rho}{\partial t} + \nabla\cdot(\rho\mathbf{v}) = 0 \tag{2.2}$$

and for constant density it simply reduces to

$$\text{div } \mathbf{v} = \nabla\cdot\mathbf{v} = 0 \tag{2.3}$$

The Navier-Stokes equation shown in (2.1) is highly nonlinear, that is partly why it is so difficult to find analytical solutions for anything but the most simple scenarios.

2.1.2 Laminar flow

Turbulence is a highly effective manner to produce effective mixing and increase collisions of contained particles. In the late 1800's, Reynolds determined a dimensionless parameter to classify when a fluid in a particular system would form turbulent or laminar flow. He

gave his name to the well known Reynolds number,

$$\mathrm{Re} = \frac{\rho U L}{\mu} \tag{2.4}$$

where U $(m^2.s^{-1})$ is the characteristic velocity, and L (m) a characteristic size (Randolph and Larson 1988). It is quite common to write

$$\nu = \frac{\mu}{\rho} \tag{2.5}$$

which is known as the kinematic viscosity and has the unit $(m^2.s^{-1})$. This allows us to express the Reynolds number as,

$$\mathrm{Re} = \frac{UL}{\nu}, \tag{2.6}$$

Laminar flows have Reynolds numbers of below 2000. At these Reynolds numbers very little or even no mixing will occur. As the velocity increases for a set value of ν and L, a transition from laminar into turbulent flow will occur. At low Reynolds numbers, the kinematic viscosity will be the dominant factor determine the type of flow. The kinematic viscosity describes the forces present within fluids and how easily the fluid can flow. A fluid such as honey will have a very high kinematic viscosity, and will not easily transition into a turbulent flow regime. However gasses have higher kinematic viscosities and will easily become turbulent with a small rise in the characteristic velocity. In figure 2.1 the transition from a laminar flow to a turbulent flow can be seen. When a dye tracer is placed in a laminar flow it will follow the stream lines, however the moment the velocity of the fluid increases, and turbulent flow is created, the tracer can no longer follow the stream lines. It quickly become dispersed and mixed within the liquid. Little or no mixing will occur if only a laminar regime is employed within a reactor.

2.1.3 Turbulent flows

Turbulent flows allow for the effective transport and mixing of fluids. Turbulent flows occur at higher Reynolds numbers when compared to laminar flows. For example in a pipe flow, it can be observed that below $\mathrm{Re} < 2300$, the fluid will experience laminar flow. Above $\mathrm{Re} > 4000$ it will be fully turbulent, and in between those two levels it can be considered in a transitional phase between the fully turbulent and laminar flow (Pope 2001). Typically, all reactors used for the study of aggregation will operate at high Reynolds numbers. This allows for sufficient collisions to occur and will exclude the chance of perikinetic aggregation. Figure 2.1 shows that turbulent flows form eddies of various sizes. The eddies whirl and mix the fluid, and disperse the dye tracer as it tries

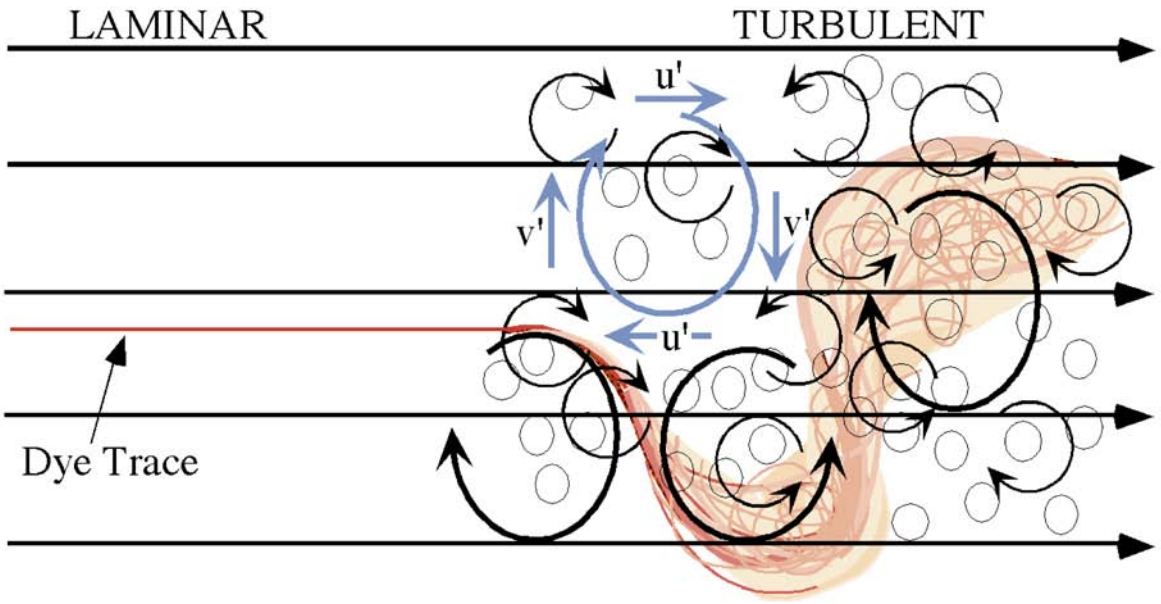

Figure 2.1: A dye tracer placed in the laminar flow initially follows stream lines until it enters a region of turbulent flow where it quickly becomes dispersed within the liquid because of the turbulence. (Nepf,2007)

to follow the movement of the eddies.

2.1.4 Energy cascade , energy dissipation, Kolmogorov micro scales.

Energy dissipation in turbulent flows occurs through the development and motion of the eddies. The increased velocities impart higher shear forces on the fluid and eddies result as a means to dissipate the energy. The turbulent eddies are the swirls of fluid created at high Reynolds number flows, and they vary in sizes. The largest eddies are nearly of the size of L, the characteristic length scale for a system. The characteristic length depends on the type of the experimental setup, and the the agitator used to stir the system. For example, in a stirred tank reactor, L will be D ,which is the diameter of the impeller.

If the Reynolds numbers is defined for each eddy as follows, where l_0 is its characteristic length, then the characteristic velocity will be defined as $u(l_0)$, or u_0 for succinctness, then we have

$$\mathrm{Re}_0 = \frac{u_0 l_0}{\nu}. \tag{2.7}$$

for the largest eddy. This will be comparable to the Reynolds number for the system, since ν is no longer the dominant force in the turbulent system as it was in the laminar flow regime. $u_0 l_0$ are now the dominant terms. It is thought that the energy from the larger eddies is transferred to smaller eddies until such a time that the Reynolds number for the smallest eddy is small enough to be a stable constant size. This happens, because both

$u_\alpha$and l_α decrease, and the kinematic viscosity becomes significant in the determination of Re_α, the Reynolds number of the smallest eddy. This effect is known as energy cascade, and the name is self explanatory as one can think of the energy cascading down to the smaller eddies from the larger eddies.

Along with defining characteristic velocity and length, a characteristic time scale is defined,

$$t_\alpha = \frac{l_\alpha}{u_\alpha}$$

In a multiphase systems consisting of suspended particles in solution, the particles tend to follow the stream lines of the flow. This is especially notable when the particles are smaller than the length of the smallest eddies. The Kolmogorov micro-scale is the length scale of the smallest eddy. It can be determined if the viscosity and energy input of the system are know

$$\eta = \left(\frac{\nu^3}{\epsilon}\right)^{1/4} \tag{2.8}$$

where $\epsilon(W.kg^{-1})$ is the energy input or energy dissipation . The Stokes number is a dimensionelss number and can then be used to determine whether particles of diameter, d, will follow the stream lines of the fluid flow. The Stokes number is defined as,

$$\mathrm{St} = \frac{t_\alpha u_0}{d}.$$

If a particles Stokes number for particle, is $\mathrm{St} \ll 1$, then the particle will follow the fluid flow. If $\mathrm{St} \gg 1$, it will not follow the stream lines. For example, at a typically used energy dissipation of 0.1 W/kg within a oscillating multi-grid reactor, there should not be eddies of length smaller than 56 micron in water. This implies that particles less than approximately 50 microns will follow the stream lines of the flow. Consequently, this also implies that inertial effects can be ignored for particles smaller than the Kolmogorov micro-scale.

2.2 Nucleation and Aggregation

The nucleation of nanometer size particles will only be briefly discussed as it does not form any significant part of this work. The driving force for nucleation in any precipitation system is the supersaturation. The higher the supersaturation, the greater the likelihood for nucleation to occur. Of more importance is to clearly define what aggregation is. The aggregation of particles should be considered the coming together of particles for a long enough time such that a strong enough crystal bond can form which will not be broken by shear forces. Particles can come together in more than one way. Particles

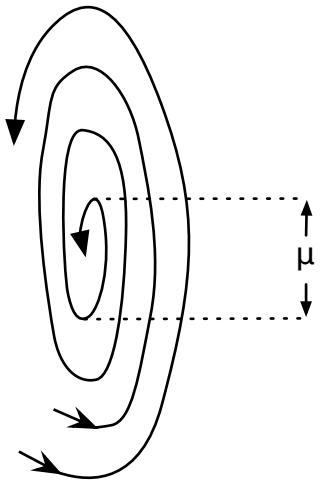

Figure 2.2: The Kolmogorov micro-scale, a measure of the smallest scale of turbulence. In this case, the smallest eddy.

may come together by traveling along the same stream lines long enough to form the bond, or through a collision where there will be a transfer of momentum. The factors which significantly effect the aggregation are the turbulence (causes of the collisions), the saturations (provides the materials for permanent bonds to form), and the typical electrostatic forces, such as v.d. Waals force.

2.2.1 Supersaturation

The supersaturation acts as the driving force for nucleation. The supersaturation is analogous to the concentration at fixed temperatures, and often concentrations are used instead. From figure 2.3 , the solubility curve defines the concentration required to saturate a solution. If this point is define as C^* ($mg.dm^{-3}$), then the supersaturation of a solution will occur when concentrations of above C^* are created. A measure of the supersaturation is the difference between the saturation concentration and the actual concentration

$$\Delta C = C - C^*$$

where C is the measured or calculated concentration. Supersaturated solutions can be made by cooling a saturated solution or by mixing two solutions which result can in a compound of lower solubility. Depending on the level of saturation achieved, the solutions can be either undersaturated, which will result in nothing being precipitate out, or it may be in the metastable zone, where seeding could result in precipitates being formed and finally the solution may be in the region above the metastable limit where spontaneous

nucleation will occur (eventually).

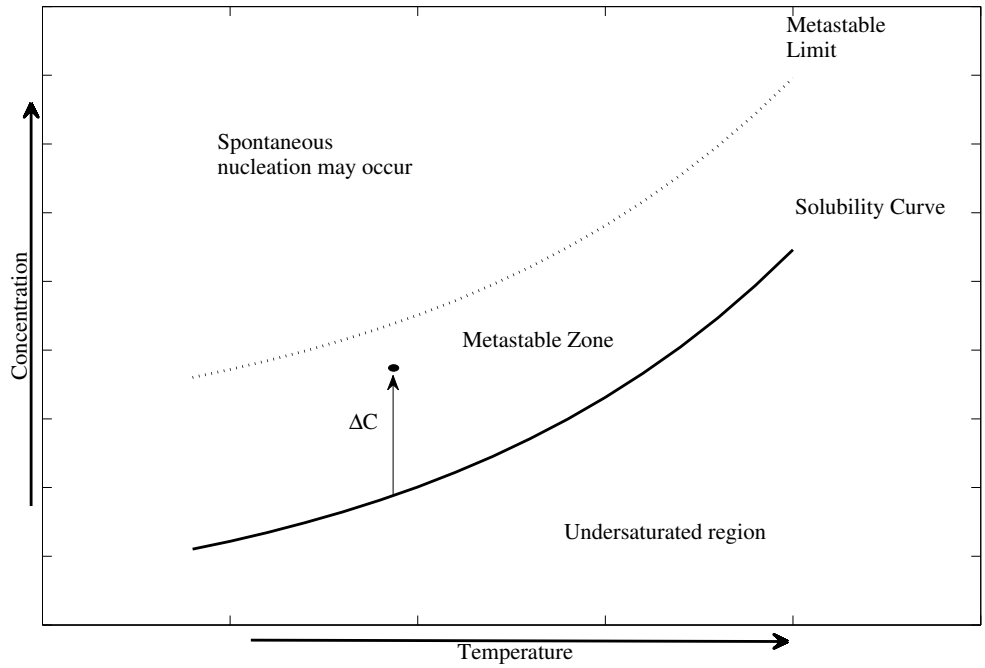

Figure 2.3: A typical solubility curve showing the regions of under saturated, metastable and supersaturated solutions.

2.2.2 Particle Kinetics

A theory for the aggregation of small particles was first proposed by Smoluchowski (1918). It was the first time that a mathematical model was developed to describe the collisions and interactions between two similar particles and was the preeminent theory for numerous years. In this paper, Smoluchowski, describes the coagulation of identical spheres through interactions caused by Brownian motion and shear flows. For shear flows of particles of similar sizes he found the collision frequency,

$$J_{ij}^{0} = \frac{1}{6}\dot{\gamma}(d_i + d_j)^3 n_i n_j,$$

where $\dot{\gamma}$ is the shear rate and d_i and d_j are the diameters of the particles i and j and of concentrations, n_i and n_j. Smoluchowski's model was basic as it only dealt with simple shear flows, however it had set a standard to be followed on later by the likes of Saffman and Turner (1956). In their 1956 paper, they developed on the existing model, generalizing it to more complex flows, like those in a stirred tank reactor. Their theory dealt with what type of "collisions" occurred, as well as the underlying flows which

caused such collisions. The mechanics which are in effect to create an aggregate are complex, however to formulate a model, simplifications have to be made. Fundamentally, a "collision" between two particles which results in an aggregate forming should not be thought of as two billiard balls colliding and sticking together. It should however be considered a *coming together* of two particles (Rodriguez-Pascual 2013), after traveling in close proximity and forming a physical bond between themselves, hence the necessity to distinguish it from collisions and the connotations that come with it. Whether a "collision" is successful and an aggregate forms, generally depends on the particles staying together long enough for the bond to form.

To determine if particles will spend the required length of time together to form a bond, necessitates the need to understand the fluid flows, and how particles travel within the fluid themselves. Saffman and Turner (1956) determined that for particles of size r_i and r_j, and of concentrations, n_i and n_j, the collision frequency between two particles can be described as follows

$$J_{ij}^0 = 1.30 \left(\frac{\epsilon}{\nu}\right)^{1/2} (r_i + r_j)^3 n_i n_j. \tag{2.9}$$

This equation allowed for a greater variance in the size of the colliding particles with $(1 \leq r_i/r_j \leq 2)$ as the only condition. In simple shear flow, van Smoluchowski showed that the aggregation of particles can be modelled using the population balance equation,

$$\frac{dn_i}{dt} = \frac{1}{2} \sum_{j=1}^{i-1} J_{i,i-1}^0 n_i n_{i-j} - n_i \sum_{j=1}^{\infty} J_{ij}^0 n_j, \tag{2.10}$$

where J_{ij}^0 is the collision frequency between particles i and j. These ideas were eventually developed further to model large systems of interacting particles.

2.2.3 Types of Aggregation

Aggregation can be split into two sub categories, that of perikinetic aggregation and orthokinetic aggregation. Perikinetic implies the aggregation occurs by means of the random motion of particles (Brownian motion), and the natural diffusion which occurs in a liquid. This can also be This type of motion is typically only observed in systems which do not experience high levels of turbulence, for example such as when a laminar flow regime is present. The stochastic movement of particles as described through their Brownian motion allows for collisions to occur even in a laminar regime when particles are expected to simply follow the stream lines and is shown in figure 2.4a. Orthokinetic aggregation covers the aggregation more likely to occur in turbulent systems. Orthokinetic aggregation is due to the shear forces imparted to the liquid. In certain laminar flows it is possible for collisions to occur due to a difference in the velocities within a reactor. For

example in a pipe flow reactor, the fluid at the center of the pipe travels the fastest and the fluid along the wall theoretically has a zero velocity as depicted in figure 2.4b.

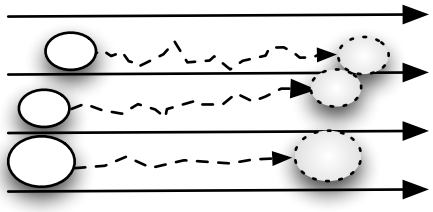

(a) Perikinetic aggregation in laminar flow.

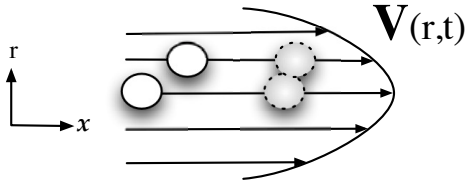

(b) Orthokinetic aggregation in laminar (pipe) flow due to the velocity differences across the profile of the pipe.

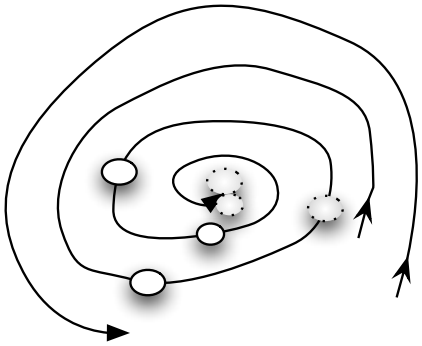

(c) Orthokinetic Aggregation in the center of an eddy (Particle trajectories overlap the stream lines and are not visible.)

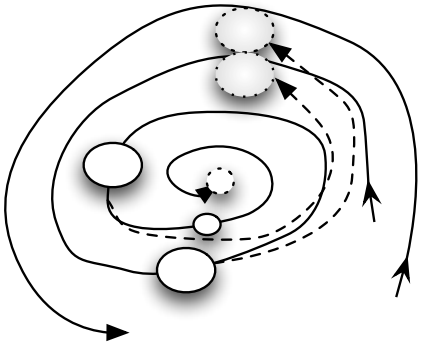

(d) Orthokinetic Aggregation due to the inertial effects of larger particles at higher Stokes numbers.

Figure 2.4: The various types of aggregation which can take place in laminar and turbulent flows. The solid spheres represent the initial position of the particles, with the dashed line spheres representing their position after a moment of time has past.

A particle traveling in the center of the reactor will have a greater velocity than a particle away from the center. This difference in their velocities can result in the particles colliding. Particles may also come together in the center of an eddy as depicted in figure 2.4c. The particles follow the stream lines until the smallest eddy where they may gather for long enough periods for aggregation to take place. Finally if particles become larger and their Stokes number exceeds one then the particles will lose their ability to follow the stream lines of the fluid and inertial effects may take over. Large particles deviate from the streams lines and can collide with smaller particles with Stokes numbers of less than one which are still able to follow the stream lines of the fluid flow. This type of aggregation is depicted in figure 2.4d.

2.2.4 Morphology and Fractal Dimensions

The morphology of the particles can effect the effectiveness of the collisions to form aggregates. If we consider ψ_0 to be the packing density, which describes how tightly the aggregated particles are packed together, then, for perfect spheres, the following equation for the collision radius of a particle was derived,

$$R = r(1/\psi_0)^{1/3}. \tag{2.11}$$

Equation 2.11 however has to be modified for particles which do not form perfect aggregates. Tambo and Hozumi (1979) have shown that aggregated particles have a tendency to form fractal like geometries and not tightly packed spheres. This forced the introduction of an additional factor into the above equation, denoted the fractal dimension, D_f. It was shown by Kusters et al. (1997) that the updated collision radius is now,

$$R_i = r(i/\psi_0)^{1/D_f}. \tag{2.12}$$

after defining the new packing density as

$$\psi_i = \psi_0(R_i/r)^{D_f-3}. \tag{2.13}$$

The experiments run by Tambo and Hozumi show that the floc density decreases with increasing floc size. Alternatively stated, the porosity increases with increasing floc size. This has a significant effect on the collision rate and the likelihood of a successful collision. Fractal aggregates were found to increase in size at a greater rate when compared to spherical aggregates. This implies that the collision radius increases faster as well. Jiang and Logan (1991) found this to be true, as well as noticing that the total number of particles decreased faster than compared to particles of constant density (volume increasing proportionally with increasing mass). Koh et al. (1984) found the total number of particles present in the solution obeyed the following exponential equation,

$$n_{tot} = n_0 \exp(-s\tau). \tag{2.14}$$

Where n_0 is the initial concentration and s is a dimensionless volume averaged shear rate. τ is the dimensionless time variable. This allows for the prediction of the total number of particles as the experiment progresses. If it is found that the particles, when analyzed under a microscope do not form nice spheres (the shape factor is not approximately $\pi/6$) but in fact more porous objects, it would be necessary to fit predicted PSDs with the inclusion of the a fractal dimension.

2.2.5 Population Balance Equations and Particle Size Distributions

The population balance equation for a well mixed batch system expressed in a form that shows the dependence on the length , L, of the particles is given by Randolph and Larson (1988),

$$\frac{\partial n}{\partial t} + G\frac{\partial n}{\partial L} = B - D. \tag{2.15}$$

In (2.15), n is the number density function (the population density) or the instantaneous change in the number of particles contained in an infinitesimally small region of size dL. It is possible to then write,

$$n(L) = \frac{dN}{dL}. \tag{2.16}$$

where dN is the cumulative number distribution (total number of particles). If we consider the particles to be spherical, then L will represent the diameter of the particle. B and D are birth and death functions respectively. These take into account the possibility of particles appearing into and disappearing from a discrete phase space.

2.2.6 Determination of the Aggregation Rate Constant

The aggregation rate primarily depends on two actions, the number of collisions occurring, and the efficiency of the collisions. These two actions together result in the aggregation rate, and can be summarised succinctly in the following formula as proposed by *Hounslow et al. (2001)*,

$$r_{agg} = \psi r_{coll}. \tag{2.17}$$

r_{coll} is rate of collisions and ψ is the efficiency of the collisions. This efficiency describes how often two or more collided particles form a strong enough crystal bond to form a new aggregate. r_{agg} is the total aggregation rate which will be determined through the analysis of the particle size distributions and moment transformations as described below.

2.2.6.1 Moments

It is convenient and easy to find the moments of any probability density function, and likewise a particle size distribution. The only difference between the two is that the area under a probability density function must sum to one, and the area under the PSD will represent the total number of particles. The one has been normalized, and the other has not. The moments of the PSD can be calculated as follows,

$$m_j = \int_0^\infty n(L) L^j dL \qquad \text{for } j = 0, 1, 2... \tag{2.18}$$

It should be apparent then that m_0, the zeroth moment represents the total number of particles, m_1 the total length, m_2 the total area and m_3 the total volume of the particles, give or take some shape factor depending on the actual shape of the particles.

The population balance can be expressed using moments, and for size independent growth and aggregation, we are able to attain the following pair of equations (Bramley et al. 1996),

$$\frac{dm_0}{dt} = -\frac{1}{2}\beta_0 m_0^2 \tag{2.19}$$

$$\frac{dm_3}{dt} = 3Gm_2. \tag{2.20}$$

Hence, it is possible to attain the growth and aggregation rate constants from an experimental PSD in the following manner. We first discretize the integral for finding the moments, equation (2.18),

$$m_j = \sum_0^k n(\bar{L_k}) \bar{L_k}^j \Delta L_k \tag{2.21}$$

where for $\bar{L_k} = \frac{L_i + L_{i+1}}{2}$, the average of the upper and lower bound of a size interval, and $\Delta L_k = L_{i+1} - L_i$, the width of the interval. The maximum value of k will be $(i-1)$. One less than the number of intervals from the experimental data. It is also possible to solve equations (2.19) and (2.20) using numerical techniques.

2.2.6.2 Optimization Scheme to find the Best-Fit Zeroth-Moment Curve

A best fit value of β_0 and G can be found such that the predictions made by the size independent model and the experimental data is minimised. The differential equation of the form $\frac{dx(t)}{dt} = ax(t)$, which is similar to equation (2.19), can be expressed numerically by approximating the derivative as follows, $\frac{dx(t)}{dt} \approx \frac{x(t+\Delta t) - x(t)}{\Delta t} + \mathcal{O}(h)$ ($\mathcal{O}(h)$ is shorthand for higher order terms, which are not required to find an accurate result in this work). This approximation is only first order accurate, however it is sufficient for the analysis of the experimental data to come. It is derived from the simple Taylor expansion of a function $f(x)$ around the point x,

$$f(x+h) = f(x) + hf'(x) + \frac{1}{2}h^2 f''(x) + \dots$$

It can be seen that this can be written as if terms of the order h^2 and above are ignored

$$f^{'}(x) = \frac{f(x+h) - f(x)}{h} + \mathcal{O}(h).$$

If we now consider $f(x)$ to be m_0 at time t, $f(x+h)$ to be m_0 at time t plus an small time later,d h is Δt, and $\mathcal{O}(h)$ to be very small, then from equation (2.19),

$$\frac{m_0(t+\Delta t) - m_0(t)}{\Delta t} = -\frac{1}{2}\beta_0 m_0(t)^2. \tag{2.22}$$

In a numerical scheme $m_0(t)$ will be represented as m_0^i the value of m_0 at the i'th iteration, and $m_0(t+\Delta t)$, a small time step (Δt) forward representing one iteration, will be the predicted value of m_0 at the $i+1$ iteration, denoted as m_0^{i+1}, and this is shown as follows, where m_0^{i+1} is eventually made the subject of the formula,

$$\frac{m_0^{i+1} - m_0^i(t)}{\Delta t} = -\frac{1}{2}\beta_0 (m_0^i)^2, \tag{2.23}$$

$$m_0^{i+1} = m_0^i - \frac{1}{2}\beta_0 (m_0^i)^2 \Delta t \tag{2.24}$$

The same can be shown for equation (2.20), and the final result is given below,

$$m_3^{i+1} = m_3^i + 3G m_2^i. \tag{2.25}$$

The optimisation scheme is described in detail in the results and analysis chapter, §4.2.6. A function is determined which measures the total distance between the expected and observed values of m_0. This function is then minimised and the value of β_0 at the minimum is then the optimised value to be used.

2.3 Comparison of Reactors

Reactors form an integral part of all chemical processes. The design of the reactor can significantly affect the resultant product, hence it is essential that the most appropriate reactor be chosen for a particular purpose. From §2.4.1.3 and the theory on how the hydrodynamics of the system can influence the aggregation of particles, it is essential to evaluate the reactors used in literature. A large variety of reactors have been used in the study of the aggregation rate of calcium oxalate, these include, the use of a magnetic stirrer in a flask (Bramley et al. 1996), a baffled and jacketed CSTR (Collier and Hounslow

1999; Kusters et al. 1997; Kusters 1991), a Poiseuille flow reactor (Mumtaz and Hounslow 2000) and also a Couette flow reactor (Hollander et al. 2002; Hollander 2002). Each reactor was chosen for a specific reason, and these will be discussed below.

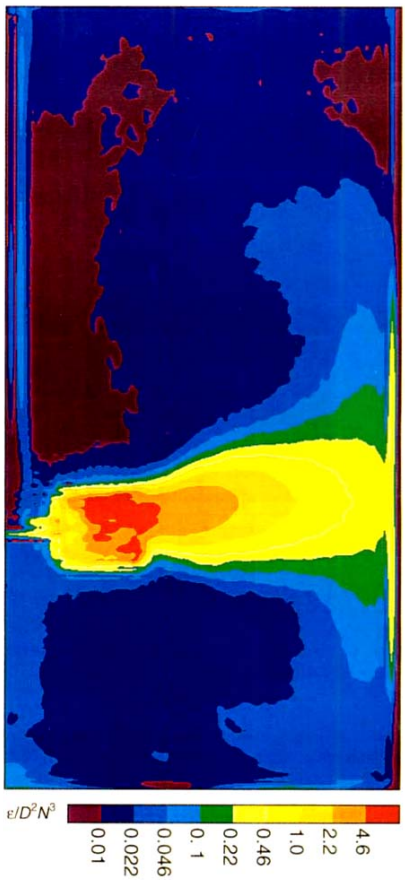

Figure 2.5: The nondimensionalised energy dissipation around a Rushton blade impeller in a baffled CSTR. The red and yellow colours represent zones of high energy dissipation, the darker blue colours represent those of low energy dissipation.(Derksen and Van den Akker 1999)

2.3.1 Continuously Stirred Tank Reactor

CSTRs are one of the most frequently used reactors. This is because they provide excellent macro mixing. The energy input for CSTRs has been well defined and studied (Pope 2001), and computational fluid dynamic models of the hydrodynamics of a CSTR, including situations with multiphase flow have been modeled (Lindenberg et al. 2008). However, for aggregation systems there are certain characteristics of the CSTR which are undesirable. The energy dissipation, through the formation of turbulence in the fluid, and the creation of eddies is limited to regions very near to the impeller (Derksen and Van den Akker 1999). This is observable in figure 2.5. The red and yellow colours show regions of high rates of energy dissipation. This will correspond to highly turbulent regions, with

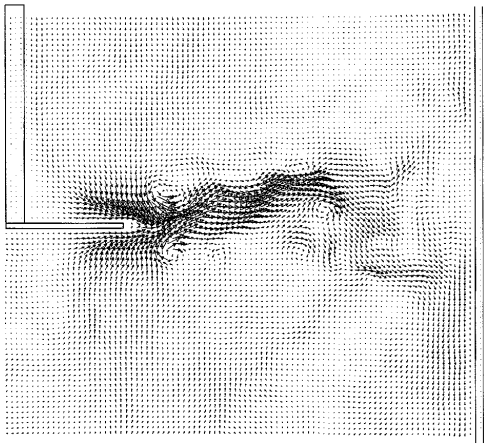

Figure 2.6: Velocity field of a vertical cross section of a baffled CSTR. (Derksen and Van den Akker 1999)

steep velocity gradients and large shear rates. What is also noticeable is that, a small distance away from the impeller, there is little to no energy dissipation, as represent by the darker blue and maroon colours. The velocity field as represented in figure 2.6 shows similar information. The changes in the velocity near to the impeller are much greater than a small distance away from the impeller. The effect of such a velocity field in a system where aggregation is desirable is significant. From previous sections it is known that turbulence, is in general, necessary for aggregation to occur. This is because turbulence increases the likelihood of collisions between particles. However, if the velocity gradients are to significant, and the shear rates are very large, aggregates can quite easily be broken apart. This is likely near to the impeller. The non-uniformity of the velocity field inside a CSTR is a far from ideal environment wherein to study the effect of energy input on the aggregation of particles.

2.3.2 Poiseuille Flow Reactor

A Poiseuille flow reactor, also know as a pipe flow or plug flow reactor, has a very well defined velocity profile throughout the reactor. The type of flow in this reactor is laminar flow when operated at a Reynold's number of less than 2000. The maximum velocity of the fluid is at the center of the pipe, and the minimum is near the walls of the pipe. The velocity profile forms a well defined parabola shape as in figure 2.7. It is also easy to calculate the shear rate at any point in the reactor. This means that there is no turbulent energy dissipation and no mixing. Particles have to be be produced before they enter the reactor in a Y-mixer or similar device. The only manner in which particles can collide is either through perikinetic aggregation, or because of particles traveling at different velocities. There is also no way to discriminate with respect to the shear rate

when taking a sample at the bottom of the reactor. Samples are taken from the base, over the entire diameter of the pipe, which is freely open. Hence only an average shear rate calculated for a certain flow rate can be used when comparing the aggregation rate against the shear rate. Aggregation can only occur for as long as the pipe length is, as there is no recycle stream.

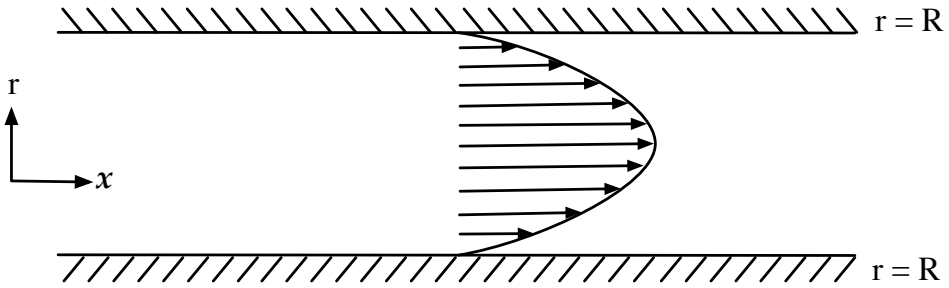

Figure 2.7: The velocity profile in a Poiseuille flow reactor. It forms a parabola, with the maximum velocity in the center of the pipe.

2.3.3 Couette Flow Reactor

A Couette flow reactor is one which has two concentric cylinders, with the fluid region between the cylinders. One of the cylinders is made to rotate along its vertical axis. At low Reynolds numbers the resultant velocity profile has a constant gradient along the radial axis between the inner and outer cylinders. The greatest fluid velocity is next to the wall of the inner cylinder. This is guaranteed by the no slip condition. The lowest, is at the outer wall which is not moving, with a constant decrease in the velocity between the inner and outer wall. At low Reynolds numbers, the flow is actually laminar flow. There is no mixing, and aggregation can only occur through tangential forces, perikinetic collisions and collisions due to the velocity differences between two particles traveling parallel to each other.

A velocity profile with constant gradient such as depicted in figure 2.8 , will have a constant shear rate between the two cylinders. This is a desirable phenomenon when investigating the effect of shear rates on the aggregation of particles. However, because this reactor produces laminar flow, there is no mixing. Particles have to be produced in another reactor, such as a CSTR before they can be introduced into the Couette flow reactor. Secondly, the type of aggregation in this reactor is significantly different to that of a highly turbulent environment.

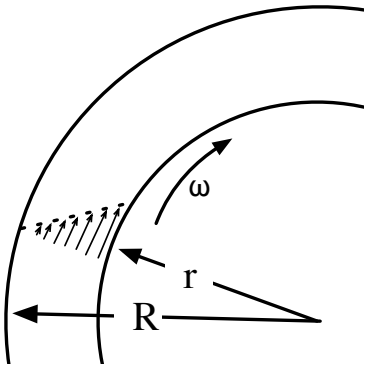

Figure 2.8: Velocity profile of a Couette flow reactor. The inner cylinder rotates with an angular velocity of ω (rad.s^{-1}).

2.3.4 The Oscillating Multi-Grid Reactor

Oscillating grid reactors were developed from concepts and ideas gained from investigating reactors with fixed grids placed in the path of fluid flow. It was noted that the fixed grids produce nearly isotropic and homogenous turbulence when fluids were passed through them (Rouse and Dodu 1955). This setup is not ideal since it would require the transport of a large amount of fluid around the reactor from the outlet back into the inlet. The same turbulence can be created if the fluid is kept stationary and instead the grid moves. This can easily be imagined by a simple transformation from one reference frame to another. Single oscillating grids have since been used because of the type of turbulence they produce, the well controlled energy dissipation and the zero mean flow rate in the reactor. Stirred tank reactors produce regions of extremely high turbulence (around the impeller) and other areas of low turbulence. The turbulence in a stirred tank is considered very anisotropic and in-homogenous. This causes problems when trying to make predictions and apply models. The properties of the flow change greatly throughout. To reduce such problems, a new type of experimental reactor was introduced in the 1950s by Rouse and Dodu. It has been continued by the likes of Thompson and Turner (1975), where they made use of 2 oscillating grids, and later by Bache and Rasool (2001), who introduced a 19 grid oscillating reactor.

The multi-grid oscillating reactor is a very suitable reactor to use when experimental setup that will produce very predictable turbulence is desired (Hopfinger and Toly 1976; de Silva and Fernando 1994). It has the ability to produce homogeneous and isotropic turbulence. A great amount of time has been spent on classifying factors such as the energy dissipation (Bache and Rasool 1996, 2001), as they have important effects on particle kinetics and the aggregation of particles. They managed to show that the energy input slightly away from a grid is

$$\epsilon = 15\nu\frac{u_o^2}{\lambda^2} \tag{2.26}$$

where λ is the Taylor micro scale, which is a length smaller than l_0, where the eddies first feel the effect of the kinematic viscosity and is largely related to the Reynolds number. u_0 is related to the frequency of oscillations in the reactor. The Reynolds number was also determined, and it depends on the frequency,f ,of the oscillations, and the length of the stroke, S,

$$\mathrm{Re} = \frac{fS^2}{\nu}. \tag{2.27}$$

The OMR is unique in its ability to produce nearly isotropic and homogenous turbulence. This is an ideal type of turbulence for mixing and aggregation of particles. This is because each and every particle will experience similar forces and number of collisions. It can be shown that the turbulence is nearly isotropic and homogenous by looking at the RMS velocity profile along the length of the reactor. There is a small net change in the RMS velocity along the column, and is much less than one would observe in a CSTR.

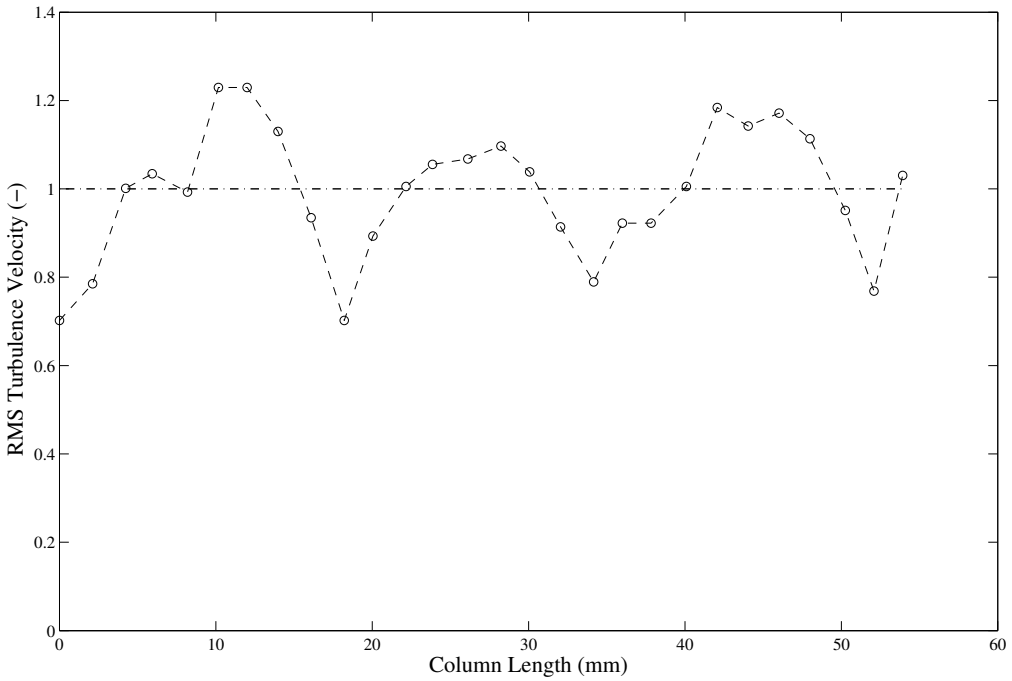

Figure 2.9: RMS velocity profile along the length of the OMR. (Bache and Rasool 2001)

From figure 2.9 it should be observed that the nondimensionalised RMS velocity varies by no more than 14% along the length of the reactor. The velocities are normalised by dividing them by the RMS velocity. This is much less than when compared to the varied turbulence in a stirred tank reactor. Extremely high shear rates are found near the impeller blades but they drop off significantly a small distance away. In an unbaffled reactor this is even more noticeable, as a result of the solid body rotation of the fluid(Madhrani

2008; Rielly et al. 2007).

2.3.4.1 The Maximum and Average Shear Rate in an OMR

The changes in the horizontal and vertical velocities at a distance z from an oscillating grid can be expressed as,

$$u_0 = C_1 s^{3/2} M^{1/2} f z^{-1}, \tag{2.28}$$

$$w_0 = C_2 s^{3/2} M^{1/2} f z^{-1}. \tag{2.29}$$

Where $C_1 = 0.22$ and $C_2 = 0.25$ are constants and M is the mesh size (Hopfinger and Toly 1976; de Silva and Fernando 1994). The integral length scale, the size of the largest possible eddies is

$$l_0 = C_3 z \tag{2.30}$$

where $C_3 = 0.1$.

It is possible to estimate the shear rate if we know the energy dissipation, ϵ, and the kinematic viscosity of the solution,ν, as follows,

$$\dot{\gamma} = \sqrt{\frac{\epsilon}{\nu}} \tag{2.31}$$

where the energy dissipation can be found as

$$\epsilon_0 = \xi \frac{u_0^3}{l_0} \tag{2.32}$$

and $\xi = 0.8$. Substituting equation (2.28), (2.29) and (2.32) into equation (2.31), the following expression for the shear rate can be found,

$$\dot{\gamma} = \sqrt{\frac{\xi C_2^3 S^{9/2} M^{3/2}}{\nu C_3} f^3 z^{-4}} \tag{2.33}$$

$$= \sqrt{\frac{\xi C_2^3 S^{9/2} M^{3/2}}{\nu C_3}} f^{3/2} z^{-2}. \tag{2.34}$$

The following properties characterize the OMR used in this research. The mesh size, M, is 0.008m. The mesh spacing is 0.018m and finally the stroke, S, is 0.02m. By inserting these values into equation (2.34) and using the value of the kinematic viscosity of water

at room temperature, it can be shown,

$$\dot{\gamma} = 0.00148 f^{3/2} z^{-2}. \tag{2.35}$$

As proposed it should be possible to determine the average shear over the desired region. Integrating equation (2.35) over the domain of a to b ,

$$\begin{aligned} \bar{\dot{\gamma}} &= \frac{0.00148 f^{3/2}}{b-a} \int_a^b z^{-2} dz \\ &= \frac{0.00148 f^{3/2}}{b-a} \left[-z^{-1} \, \Big|_a^b \right] \\ &= \frac{0.00148 f^{3/2}}{ab}. \end{aligned} \tag{2.36}$$

This will be indeterminate if $a = 0$. To initially quantify a relationship between the shear rate and the energy input, equation (2.35) a representative region within the space that each grid moves through will be used. Values of $a = 0.01$m and $b = 0.02$m away from the grid.

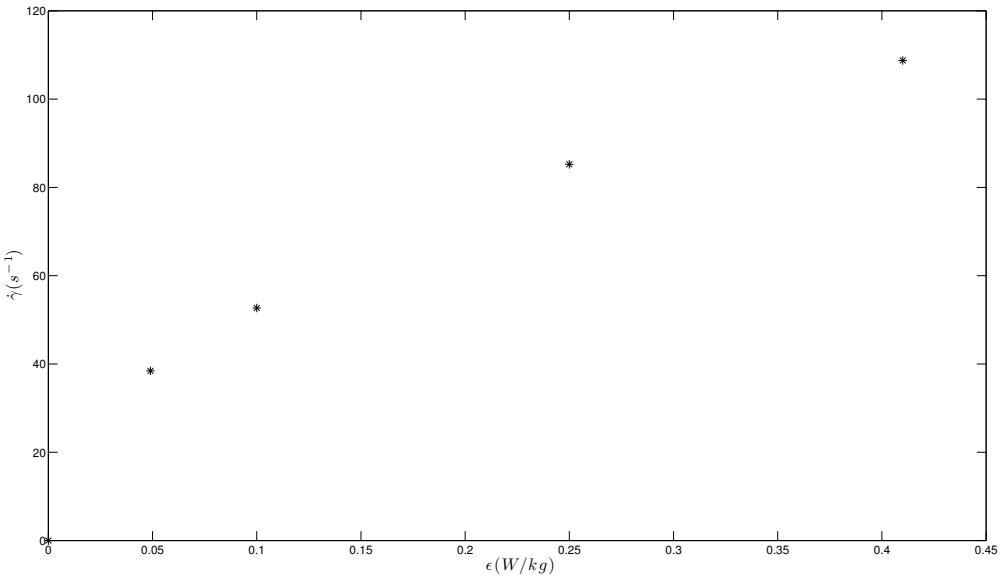

Figure 2.10: The average shear rate in an oscillating multi-grid reactor at various energy dissipations.

2.4 Calcium Oxalate

Calcium Oxalate has been used as one of the test systems wherein to study growth and aggregation since the 1970's (Finlayson 1978). Among the many reasons as to why calcium oxalate has been extensively studied, which include it being a sparingly soluble salt with a tendency to aggregate (Babić-Ivančić et al. 1985), the most pertinent reasons is because it is one of the main constituents of kidney stones (Prien and Jr. 1968; Vermeulen and Lyon 1968) in humans. Because of this, a sound understanding of the mechanisms involved in the growth and aggregation of calcium oxalate is therefore necessary.

Calcium oxalate (CaC_2O_4) is a white powder and can exist as many different forms, the most notable and stable of which is calcium oxalate monohydrate (COM, $CaC_2O_4 \cdot H_2O$), also known as whewelite. COM is a monoclinic crystal. There also exist two additional metastable hydrates, calcium oxalate dihydrate (COD, $CaC_2O_4 \cdot (2+x)H_2O; \quad x < 0.5$) and the trihydrate (COT,$CaC_2O_4 \cdot (3-x)H_2O; \quad x \leq 0.5$) which are tetragonal and triclinic respectively.

2.4.1 Factors Influencing the Precipitation of Calcium Oxalate Hydrates

There are numerous ways to influence which hydrate of calcium oxalate is predominantly formed, these include, but are not limited to, adjusting the pH and temperature, the concentration of reactants, the ionic strength of the solution, and the type of mixing regime employed. The effect of reactant concentrations will be considered first.

2.4.1.1 The Effect of Reactant Concentrations and Aging on the Formation of Calcium Oxalate Precipitates

An extensive experimental and computational study on the effect of initial reactant concentrations was carried out by Babic-Ivancic and colleagues (1985). The initial concentrations of the reacting ions were ([Ca]=$1 \times 10^{-5} - 3 \times 10^{-1}$mol.dm^{-3} and [Ox]=$1 \times 10^{-5} - 1 \times 10^{-1}$mol.dm^{-3}) . The precipitates were formed in a high ionic strength, 0.3 mol.dm^{-3} sodium chloride solution, with a pH of 6.5±0.2 and operated at a temperature of 25 $^\circ$C. Once precipitation had occurred, the solutions were also aged, to see if there were any relative changes in the proportions of the hydrates. The solutions were also aged after precipitation had occurred for various times ranging from 3-30 min, 2-3 hrs , 24 hrs and 30 days. This was to note the stability of the various hydrates, and the effect of initial concentrations on the stability. The results can be summarised in a series of plots and tables.

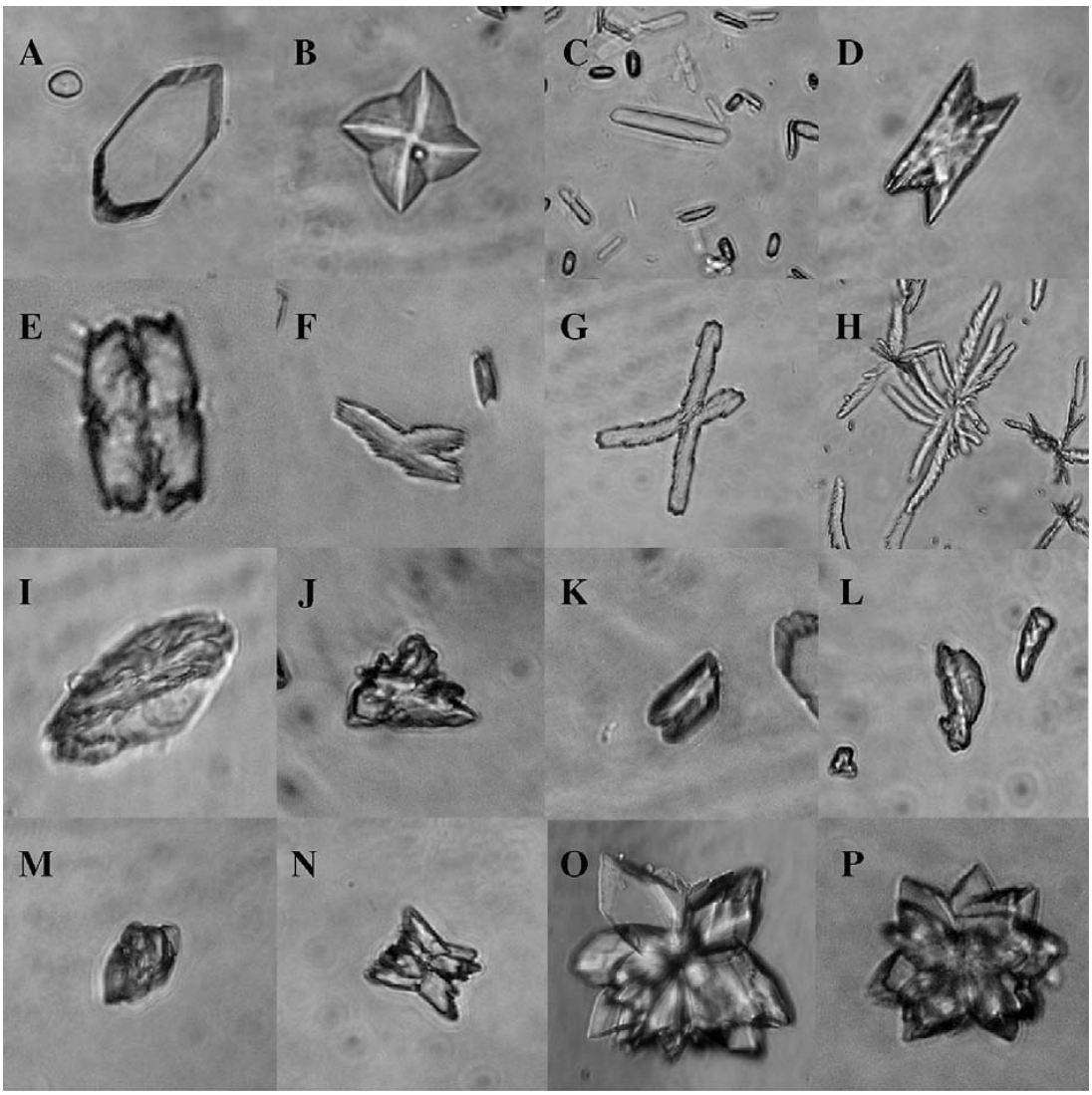

Figure 2.11: Optical microscope images of the various morphologies and hydrates of calcium oxalate. A. Monoclinic COM. B. Weddelite COD. C. COT. D. and E. COM Twinning. F. - H. Dendritic COM. I. - M. Unknown morphologies of calcium oxalate. N. - P. COM aggregates. (Thongboonkerd et al. 2006)

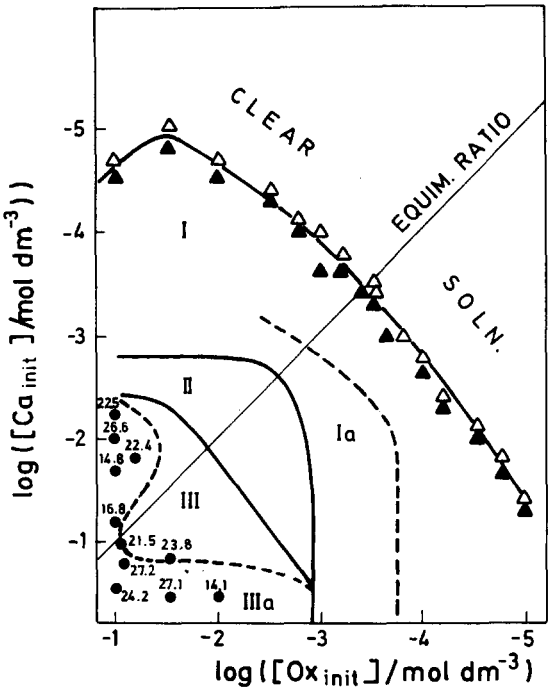

Figure 2.12: Precipitation diagram of calcium oxalate hydrates with respect to initial reactant concentrations after a period of 24 hrs has passed.(Babić-Ivančić et al. 1985)

Figure 2.12 shows the effect of the reactant concentrations on the formation of various hydrates and their morphologies. The resultant precipitates were all measured after a period of 24 hours. The open (△) and filled (▲) triangles represent experimental data which represent the metastable boundary where a precipitate was not formed and formed respectively. Region I refers to platelets of COM. Region Ia represents a region where both the COM platelets (P) and octahedral bipyramids (BP) of COD where found. Region II shows dendritic (D) COM, region III is microcrystalline aggregates of COM, and IIIa microcrystaline COD aggregates with various amounts of water content, represented by the (•) points in wt%. The concentrations below which heterogenous nucleation occurs, the growth was determined to be controlled by a surface mechanism and only compact COM and COD crystals are formed. At the slightly higher supersaturations when dendritic like crystals of COM are formed, this is due to diffusion limited growth. Regions of very high supersaturations, III and IIIa, and above the point the critical point for homogenous nucleation (figure 2.13), is where the microcrystalline aggregates of COD were found.

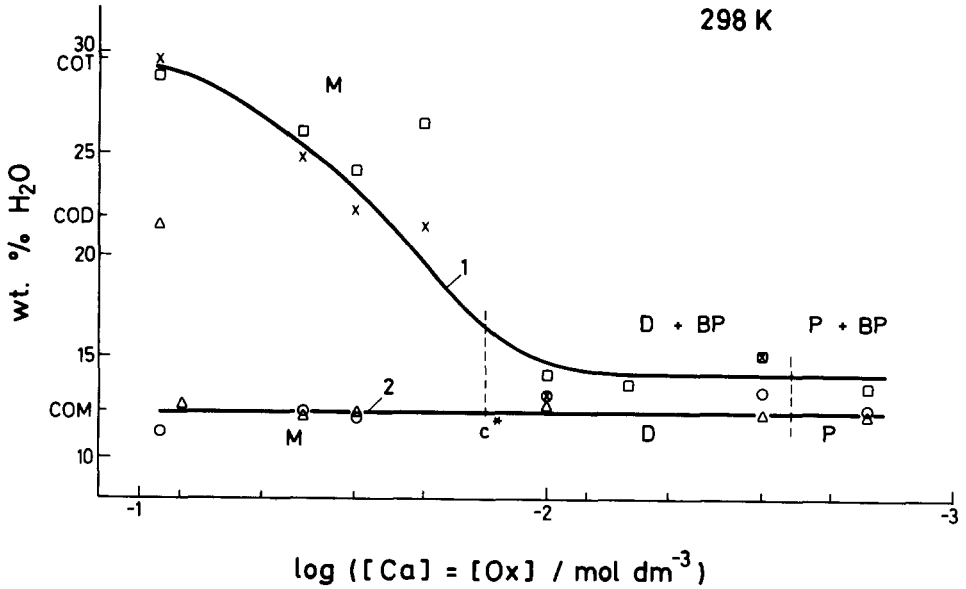

Figure 2.13: The water content present in the calcium oxalate precipitates relative to the initial concentrations as well as showing the effect of aging of the precipitates. The □ represent experimental data for aging times of 3-30 min, × 2-3hrs, △ 24hrs and ○ 30 days. c^*represents the experimental point at which heterogenous nucleation will occur.(Babić-Ivančić et al. 1985)

Next it is shown that, when equal amount of calcium and oxalate ions are reacted, that the waters of hydration depend on the initial concentration. From figure 2.13 it can be seen that at higher concentrations, microcrystalline aggregates of COT and COD are favoured. At low concentration of less than 0.01M both (D) COM and (BP) COD are found. Below 0.001M P COM and BP COD are found. It is also evident that in general all the hydrates will transform down into the stable COM form by 24hrs however they appear to be stable for up to 3hrs.

The stability over an extended time period has significant consequences in the treatment of samples. If samples are kept for longer than 24hrs, it can nearly always be assured that COM will be the only precipitate. A point from this body of work is that the rate of transformation of the COD into COM depended on the ratio of the [Ca] to [Ox] ions. If either were in excess, it would inhibit the transformation of COD into COM. The solubility product of the three hydrates was also found and it was shown that the COT is the most soluble, and COM the least, with COD falling between.

2.4.1.2 The Effect of Temperature (Kinetics) on the Formation of Calcium Oxalate Precipitates

Temperature has a significant effect on all crystallization processes. This is because it has a direct influence on the solubility of salts in solutions, and is often used to determine

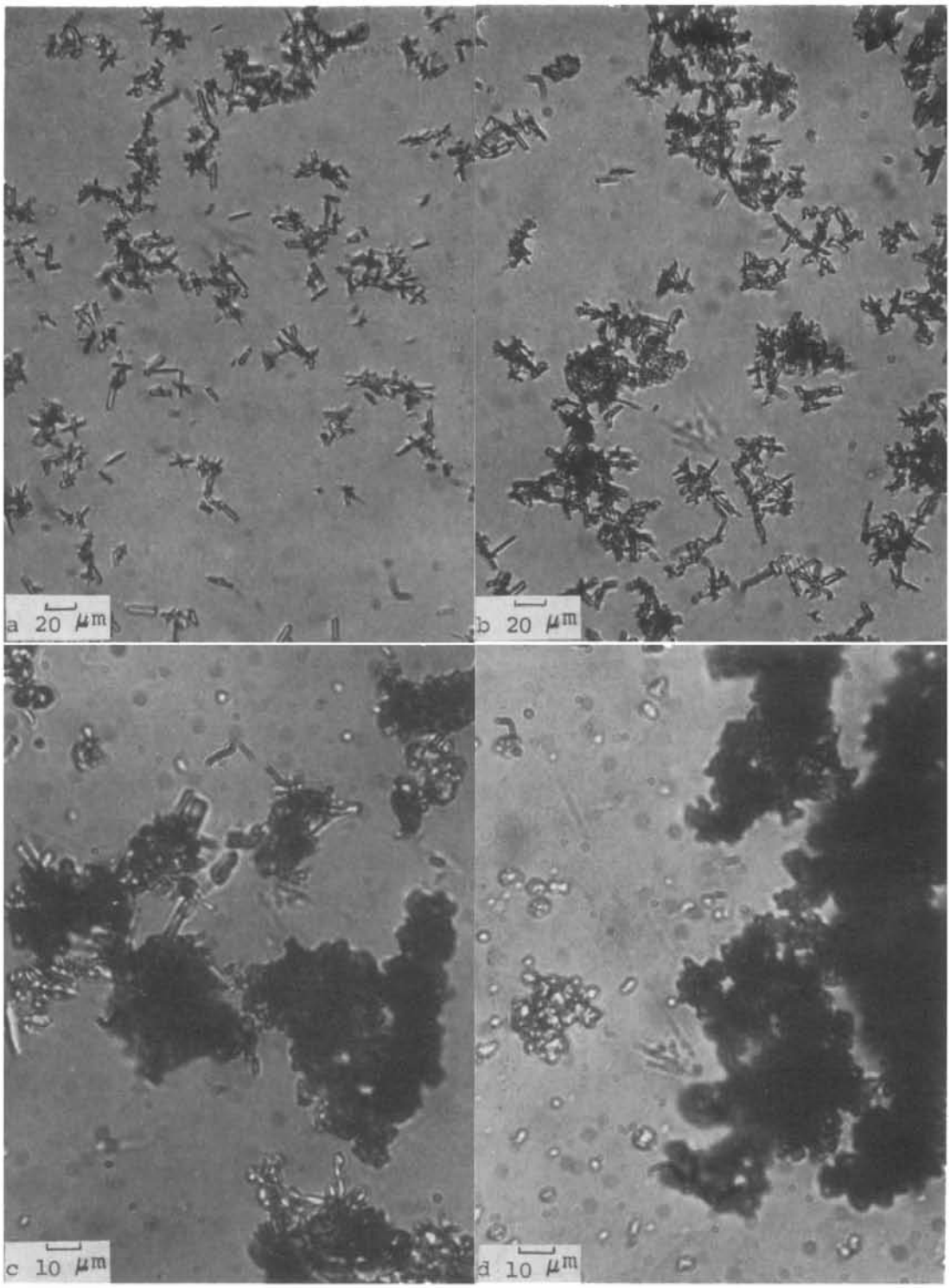

Figure 2.14: The effect of aging on samples. a. COT crystals after 18 minutes. b. Agglomerates of COT crystals after 56 hrs. c. COM and COT crystals after 72 hrs. d. COM crystals after 120 hrs. (Nancollas and Gardner 1974)

Temperature ($^\circ$C)	Composition of Precipitates
9	Only COT
25	95% COT, 5% COM
37	20% COT, 80% COM
45	Only COM

Table 2.1: Temperature dependences of calcium oxalate hydrates in an MSMPR reactor

the supersaturation of a solution as well. As already expressed in §2.4.1.1, each of the hydrates of calcium oxalate have different solubility products. A knowledge of how each of their solubility products change with respect to changes in the temperature is of importance. What can be attained from measuring the effect of the temperature on the types of precipitates formed is whether it is kinetic effects over thermodynamics factors which determine the form of calcium oxalate precipitated. In the work by Garside and colleagues (1982) they investigate the nucleation and growth kinetics of calcium oxalate hydrates in temperatures ranging from 9 $^\circ$C to 45 $^\circ$C. This occurred a steady state MSMPR crystallizer where the solution was always kept at a high supersaturation (about the saturation values for both COM and COT). Using x-ray diffraction, they were able to characterise which hydrate of calcium oxalate was formed at the various temperatures.

From Table 2.1 it is apparent that, in an unseeded system, that there is a definite temperature dependence of the form of the hydrate precipitated from solution. At lower temperatures (9 $^\circ$C) only COT is formed. At higher temperatures (45 $^\circ$C) only COM is formed. And in-between it is found that a mixture of both COT and COM. At standard temperature (25 $^\circ$C) it was found that mostly COT was formed. Further investigations where done into determining the linear growth rates as well as the nucleation rates of COM and COT.

The number density, n, was plotted against the crystal sizes, L in figure 2.15. Then using the following relationship, it was possible to evaluate the data, and determine the crystal growth rate,

$$n = n^0 e^{(-L/G\tau_n)} \tag{2.37}$$

where n^0 is the value determined for when L=0, and G is the linear growth rate and τ_n is the residence time as determined by their experimental setup. By far, the highest proportion of crystals are smaller than 20 μm. The slope of the curve for the 45 $^\circ$C run has a much steeper gradient compared to the 9 $^\circ$C run. By measuring the slope, they were able to determine the linear growth rate. And subsequently the nucleation rate using the following relation,

$$B^0 = n^0 G. \tag{2.38}$$

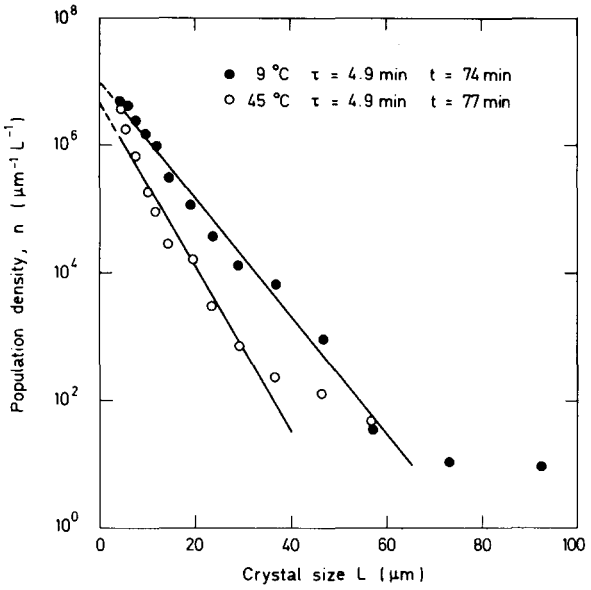

Figure 2.15: A steady state density plot, showing the particle density, n ($\mu m^{-1}L^{-1}$) against the crystal size in L (μm). (Garside et al. 1982)

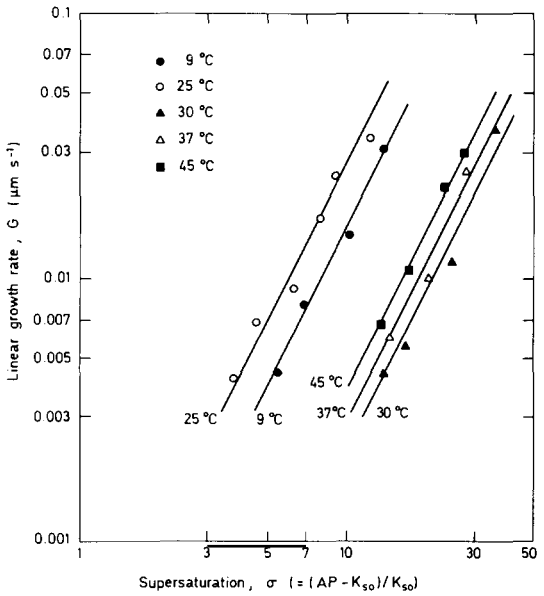

Figure 2.16: The linear growth rate is determined as a function of the supersaturation for various temperatures. The • and ○ are for 9 ° C and 25 ° C respectively. More importantly, the precipitate is predominantly COT. The ▲, △ and ■ are for the temperatures of 30 ° C, 37 ° C and 45 ° C respectively, and are predominantly composed of COM. (Garside et al. 1982)

From figure 2.16, for any of the temperatures depicted, a definite trend can be observed. The linear growth rate of the crystals has a well defined dependence on the initial supersaturation found from the slope of the data depicted in figure 2.15. As the supersaturation increases, so does the linear growth rate. In addition to this trend, there are also noticeable differences between the required supersaturation required to attain the linear growth rates at the various temperatures, as well as the form of calcium oxalate precipitated. The equivalent linear growth rates of COT, obtained at the lower temperatures of 9 $^\circ$C and 25 $^\circ$C when compared to those for predominately COM at temperatures above 30 $^\circ$C, were obtained at much lower supersaturations than those for COM (Supersaturation is temperature dependent.).

The results obtained when a mix of the hydrates COT and COM were formed where not always entirely explainable. The reason assumed was because when the majority of one hydrate was present, calculations were made using quantitative properties of the single hydrate in majority. None-the-less, when only one hydrate of either COM or COT was found, then the data suggested that the formation of the hydrates was to be dependent on the kinetics of the system, and not thermodynamically controlled. This is particularly apparent because of the presence of the thermodynamically unstable COT being formed at lower temperatures and a range of supersaturations.

2.4.1.3 The Effect of the Type of Mixing on the Formation of Calcium Oxalate Precipitates

Few studies have directly investigated the type of mixing and the effect it has on which hydrates are formed. However some startling results have arisen when it has been considered. In the papers of Brečević et al. (1986); Skrit et al. (1987); Thongboonkerd et al. (2006) they consider the effects of the type of stirring as well as the order of addition of the reagents, among other kinetic effects, on the formation of COM, COD and COT. In the paper by Skrit et al. (1987), they investigated the effect of no stirring, magnetically stirring, mechanically stirring and finally first with a magnetic stirrer until precipitates were formed, and then changing to a mechanical stirrer. They also operated at a range of temperatures and concentrations. A summary of the finding by Skrit et al. (1987) are given in table 2.2.

It was found that when a magnetic stirrer was used, even when it was first used until nucleation was observed and then a mechanical stirrer was used, it would result in the precipitation of COT only, except in one of the 10 experiments. In every experiment where only a mechanical stirrer was used, two or three of the hydrates were found. This shows a clear indication that the type of stirring can greatly effect the type of precipitate

Initial Reactant Concentration $c_{\text{init}} \times 10^{-4}(\text{mol.dm}^{-3})$ $c_{\text{init}}(\text{Ca})=c_{\text{init}}(\text{C}_2\text{O}_4)$	Temp. ($^\circ$ C)	Method of Stirring	Composition
7.0	25	Mixed	COT
9.0	25	Magnetic	COT
9.0	25	Mechanical	COM,COT
10.0	15	Magnetic	COT
10.0	20	Magnetic	COT
10.0	25	Magnetic	COT
10.0	25	Mechanical	COM,COD,COT
10.0	25	Mixed	COT
10.0	25	None	(COM,COD)>COT
10.0	30	Magnetic	COT
10.0	37	Magnetic	COM<COT
12.0	25	Magnetic	COT
12.5	10	Mechanical	COM,COD,COT
12.5	15	Mechanical	COM,COD,COT
12.5	25	Mechanical	COM,COD,COT
12.5	37	Mechanical	COM $\ll$ COT
12.5	45	Mechanical	COM,COT
13.5	25	Magnetic	COT
13.5	25	Mechanical	COM,COD,COT
16.0	25	Magnetic	COT
16.0	25	Mechanical	COM,COD,COT

Table 2.2: Characterisation of the hydrates formed for various temperatures, concentrations and methods of agitation. Mixed refers to initial stirring with a magnetic stirrer until nucleation, then using a mechanical stirrer. All solutions where buffered with NaCl , $c(\text{NaCl}) = 0.3\text{mol.dm}^{-3}$. The compositions where determined via optical microscopy, x-ray diffraction analysis and thermogravimetric analysis. (Skrit et al. 1987)

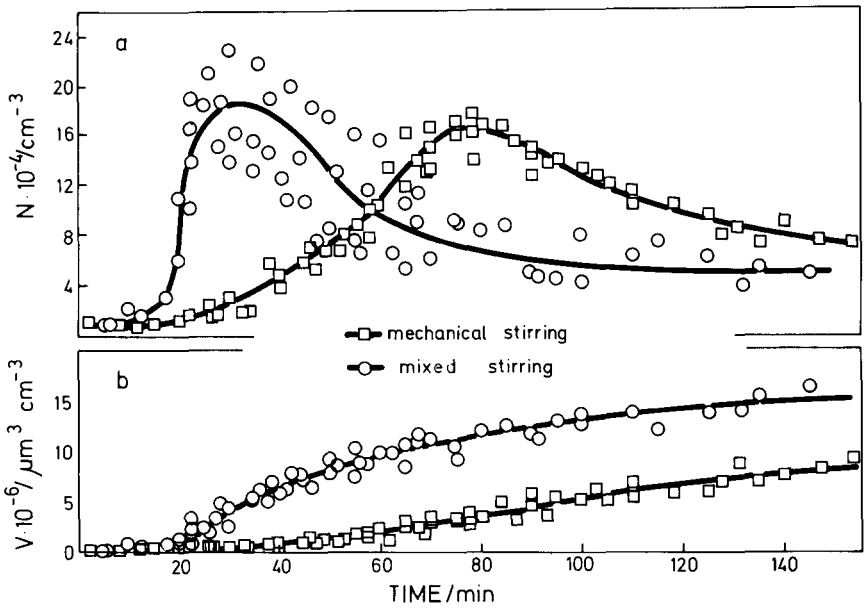

Figure 2.17: The total number and volume of particles for mechanical stirring (□) and magnetic stirring (○). $c_{\text{init}}(\text{Ca})$=$c_{\text{init}}(\text{C}_2\text{O}_4) = 7 \times 10^{-4}\,\text{mol.dm}^{-3}$,$c(\text{NaCl}) = 0.3\,\text{mol.dm}^{-3}$ and at 25 ° C.(Skrit et al. 1987)

formed. It was also shown that the small changes in the initial supersaturation had only a negligible effect on the morphology and type of hydrate of calcium oxalate formed.

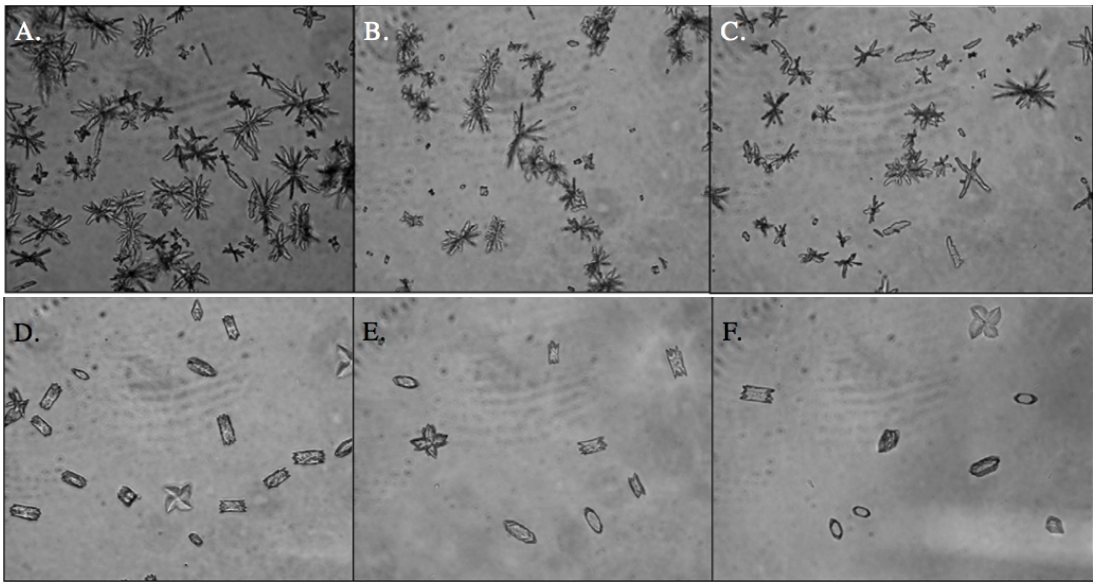

Figure 2.18: Solutions of $5 \times 10^{-3}\text{mol.dm}^{-3}$ CaCl_2 and $0.5 \times 10^{-3}\text{mol.dm}^{-3}$ $\text{Na}_2\text{C}_2\text{O}_4$ were mixed. (A) to (C) is when the $\text{Na}_2\text{C}_2\text{O}_4$ solution was added to the CaCl_2 solution, and (D) to (F) was when the CaCl_2 solution was added to the $\text{Na}_2\text{C}_2\text{O}_4$ solution. The left, center and right pictures represent experiments conducted at 4 ° C, 25 ° C and 37 ° C respectively. (Thongboonkerd et al. 2006)

From figure 2.17, it is evident that the type of stirring also effects the rate of precipitation. The maximum number of particles precipitated during a mixed stirring regime peaked 50 minutes prior to the mechanical stirring experiment. The data for the mixed stirring proved to be more erratic. When considering the volume of precipitate formed, the mixed stirring also produced a significantly larger amount of precipitate. Thongboonkerd et al. (2006) considered the effect of changing the order of which the reagents are added together and conducted a set of experiments at 4 °C, 25 °C and 37 °C. The solutions were incubated overnight, and the resultant crystals were observed under an optical microscope. From figure 2.18, it is evident that the order of adding one solution to another had significant consequences on the morphology of the crystals which were precipitated from solution. When the $Na_2C_2O_4$ solution was added to the $CaCl_2$ solution, which had a concentration 10 times higher than the $Na_2C_2O_4$ solution, dendritic COM crystals were formed. When the $CaCl_2$ solution was added to the $Na_2C_2O_4$ solution, monoclinic and twinned COM crystals were precipitated along side weddelite COD crystals. As expected, at the lower temperatures, more crystals can be observed compared to the higher temperatures. The significant differences in the morphologies of the crystals formed because of the order they were added to one another, shows how the role of mixing can be in attaining the correct type of precipitates.

2.5 Particle Sizing Methods

There are a multitude of particle sizing techniques for the one micron and bigger particles. Some of the most developed methods are those of laser diffraction (e.g., Malvern Mastersizer), the electrozone counter (e.g. Coulter Counter) and optical microscopy among others. Each of the methods have their advantages and disadvantages, such as a high sensitivity to particle volumes or numbers and a greater range of particle sizes in which they can work to name but a few. Laser diffraction, electrozone counting, optical microscopy and image analysis will be discussed below, with a particular interest given to the technique of laser diffraction.

Particle sizing is a straight forward concept, however numerous difficulties and choices will need to be made the moment the choice of sizing technique is made. The different techniques can provide very different results. The manner in which the user chooses to interpret the data also has significant implications. The output from a particle sizer is a particle size distribution. These distribution can either be a number based distribution or a volume based distribution. The methods of electrozone counter, optical microscopy and image analysis all produce number based distributions. Each particle is counted and sized individually by the equipment.

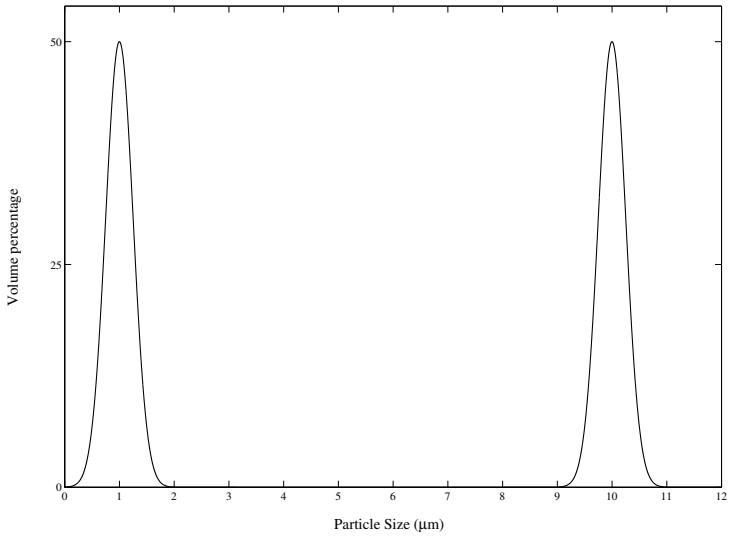

Figure 2.19: Volume percentage particle size distribution representing 1000 1μm particles and one 10μm particle.

Laser diffraction produces a volume based distribution. It is possible to convert from one distribution to another, however any error in the data is compounded. A comparison of the two different types of distributions and how particle size data is represented on each one is shown below. Consider that in a particular sample there is one spherical particle with a diameter of 10 μm, the equivalent number of 1 μm spherical particles would be 1000. It is clear from figures 2.19 and 2.20 that the data attained from identical samples can be manipulated to represent very different results. It is important then to choose the one which best represents the data and what should be attained from the data. The volume based distribution favours larger particles as compared to the the number based distribution, which favours numerous smaller particles.

The technique used to convert between the number based and volume based distribution is discussed else where. Another consideration which needs to be made is which measurement is chosen to represent the data and the particle size. Since most particles are not perfect spheres, a choice has to be made as to which equivalent sphere is used to represent the particle size. The equivalent sphere is the term given to a sphere which represents a certain characteristic of the measured particle. These characteristics can be the weight (which will include the density of the material), the volume, the surface area and potentially the shape as well.

Figure 2.21 graphically depicts the various manners in which the size of a particle can be represented. The choice of which equivalent sphere is best to use is dependent on what the data needs to represent as well as what the purpose of the measurements are for. One of the most common equivalent spheres used is d_v, the sphere with the equivalent volume

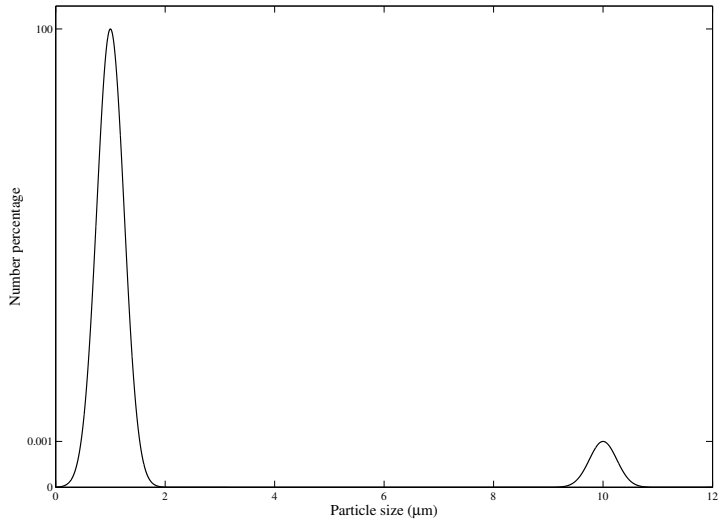

Figure 2.20: Number percentage particle size distribution representing 1000 1μm particles and one 10μm particle. The 10 μm has been exaggerated significantly, else it would not be visible as it represents only 0.1% of the particles by number.

as the particle.

2.5.1 Laser Diffraction

Laser Diffraction is a technique which uses a laser and a series of detectors to measure particle sizes. It was developed into a commercial product in the 1960's by Malvern Instruments Ltd. It works on the principle that when an object (particle) is placed in the path of a laser beam, a diffraction pattern is created as shown in figure 2.22. This diffraction pattern can be used then to resolved the size of the particle which caused it. This is an indirect particle size measurement.

2.5.1.1 Volume of Solids Concentration (Beer-Lambert Law)

The volume of solids in solution, a measurement of the fraction or percentage of the total volume which is occupied by the particles (solid material), is a measurable quantity attainable during laser diffraction particle size measurements. It is an indirect measurement of the concentration which is obtained by measuring the decrease in the intensity of an incident beam which is shone through a sample cell. If the intensity of the incident beam, I, is known before it enters the sample cell as depicted in figure 2.23, and the intensity is measured upon exiting the sample cell which has a known width, l (mm), then it is possible to relate the decrease in the energy to the concentration of solids in solution. The decrease in the intensity is due to the absorbance of the solids in solution. The relation-

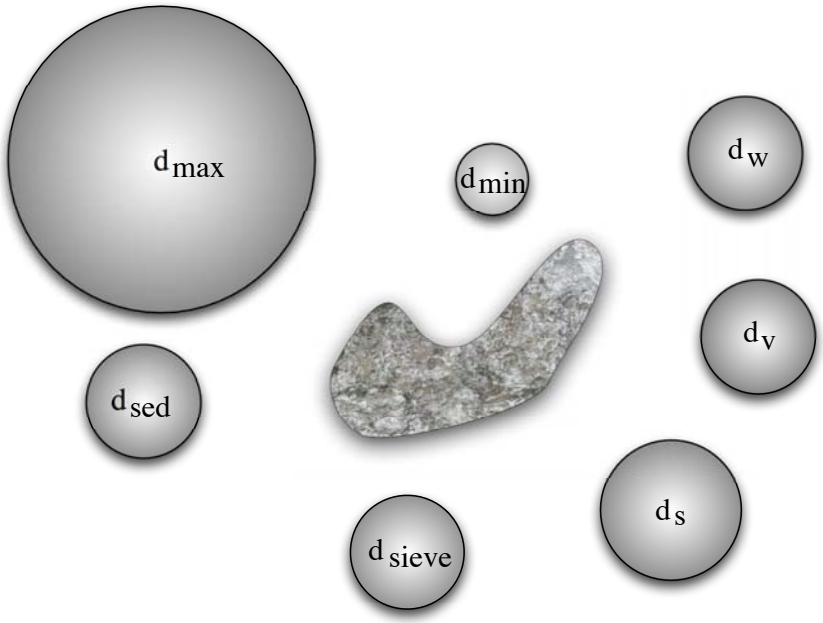

Figure 2.21: The various equivalent spheres which can be used to represent the size of a measured particle. d_{max} is the sphere with a diameter the same as the maximum length of the particle. d_{min} , a sphere equivalent to the minimum length. d_w, sphere with the equivalent weight. d_v, sphere with the equivalent volume. d_s, sphere with the equivalent surface area. d_{sieve}, sphere with the same sieve size. d_{sed}, sphere with the same sedimentation rate.

ship between the decrease in the intensity when compared to that of the incident light and the concentration of solids is expressed for *homogenous* solutions by the Beer-Lambert law,

$$\log_{10}\left(\frac{I_0}{I}\right) = \epsilon l c,$$

where ϵ is characteristic to the measured material.

The ratio of the intensity from the incident light to the measured light is often called the absorbance,

$$A = \log_{10}\left(\frac{I_0}{I}\right).$$

2.5.1.2 The Malvern Mastersizer 2000s

The Mastersizer 2000s is a particle sizer built by Malvern Instruments Ltd. It employs laser diffraction to measure particle sizes in the range of 0.02μm up to 2000 μm (2 mm). This extremely wide particle size range in which the Mastersizer is able to operate in, allows it to be used in many industries and processes. The Mastersizer 2000s can operate in both a wet and dry dispersion mode, of which the wet dispersion technique is the typical method used. Wet dispersion requires particles to be suspended in solution before

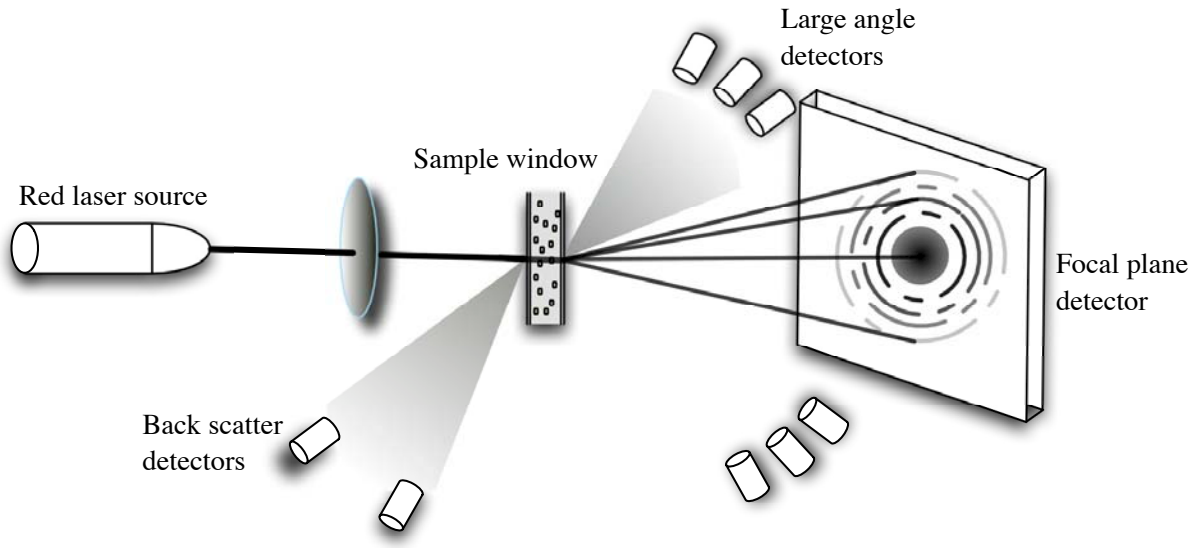

Figure 2.22: The internal setup of the laser, sample cell, detectors and lenses which are used to measure the size of particles.

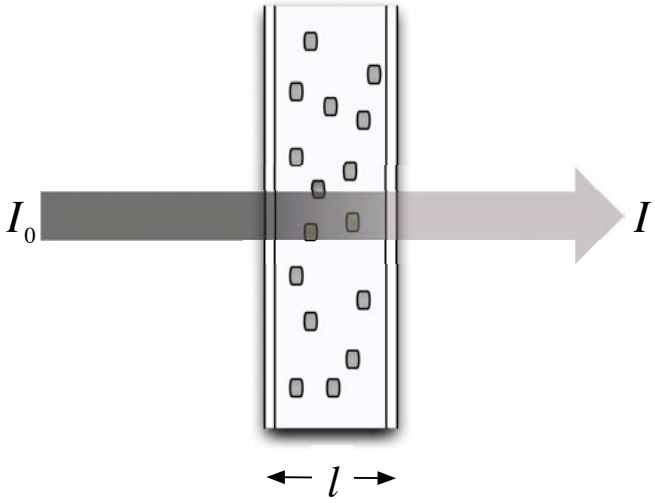

Figure 2.23: When incident light, I_0, is shone through a sample cell, the measure light energy, I, can be related to the concentration, c, of the solution via the Beer-Lamberts Law, if the path length of the light through the cell, l (m), and the absorptivity, ϵ, are known.

they can be measured. Various wet dispersion units can be used to push the solution into the sample cell through which the laser is shone. Powders and other samples can also be measured dry. The powders are aerated and blown through the sample cell and measured in the same manner as particles suspended in solution.

The Mastersizer can be operated online or individual samples can be processed. It can measure particle sizes with an uncertainty of only 1%, however if a sample has both large and small particles, the results will always be favoured towards the larger particles. This is because the method employed, measures projected areas and outputs volume based particle size distributions. Concentrations of solids in solution need to be kept below 1% for the Mastersizer to produce accurate representations of the particle sizes. This is because at too high concentrations, secondary and tertiary scattering can occur. This means when the laser light is scattered by more than one particle. Highly porous particles will also result in an overestimation of the volume fraction results. Their true volume which they occupy will be less than the measured volume calculated from the absorptivity of the light energy and their projected areas.

2.5.2 Electrozone Counting

This device was initially developed to count blood cells, but it has found other applications such as particle counting and sizing. Particles are suspended in a conductive solution. A small aperture is placed into the sample cell through which the conductive solution along with the particles are pumped. Two electrodes are placed on either side of the aperture. When a particle passes through the aperture, it is registered as an increase in the resistivity of the solutions. The duration for which this occurs as well as the change is resistance are recorded. This measurement is then related to the volume of the particle. Once a statistically significant number of particles have been measured, a particle size distribution is produced. This method of particle sizing is called the Coulter principle, named after company which developed the technology, Beckman Coulter Inc.

2.5.2.1 The Coulter Counter

The Coulter Counter, which is the device developed by Beckman Coulter Inc, has numerous advantages of the laser based sizing methods, but at the same time has many disadvantages as well. One of the main advantages is this method is able to produce number based particle size distributions because it counts and sizes particles individually. This is important as there will be no additional error introduced into the results since this distribution is of the correct basis already. The Coulter Counter can measure particles in the range of 0.5 μm and 1600 μm (1.6 mm). Though it can only do a small portion of

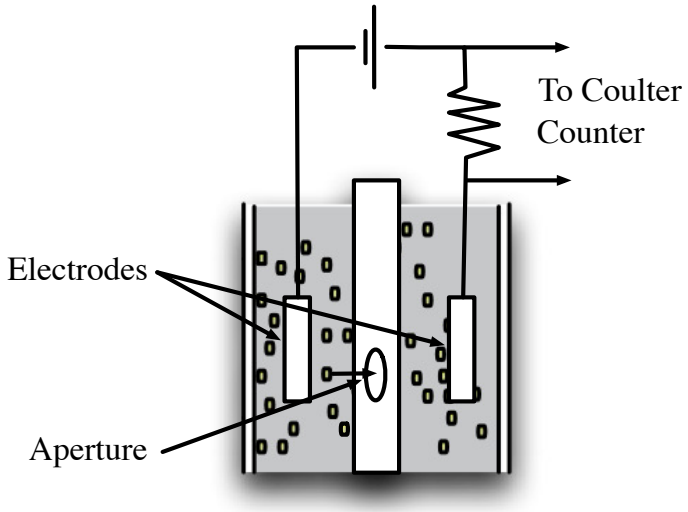

Figure 2.24: A basic representation of the Coulter principle which is used to count and size particles. The blue arrow represents the flow of particles through the aperture.

this range at any single time as it depends the the aperture size used. Apertures range from 20 μm and larger. The effective range for a particular aperture is from about 2% of the aperture size, up to about 60%. In general, particles smaller than 2 μm prove very difficult measure, and apertures get clogged up very quickly. The Coulter Counter is highly sensitive to any electrical disturbance, it requires very low dilutions (0.01% - 0.1% v/v), and becomes less sensitive near the lower limit of the device.

2.5.3 Optical Microscopy

This technique involves using an optical or electron microscope to image particles contained in a sample. Software is then able to analyse the image and count and size the particles. This technique often generates beautiful images of particles which can convey a great deal of information about their morphology. This method has some significant limitations as the sample sizes from which to derive a particle size distribution will be a fraction of the previous two techniques. This immediately means the the uncertainty in the results will be greater. This method is also very time consuming, as images need to be in sharp focus, a great deal of images need to be taken, and the processing time on the images can also be significant. The particle sizes can be incorrectly represented if there are overlapping particles and this can further influence the accuracy of the results generated by this method. Sample to be prepared for imaging by an electron microscope cannot be sensitive to or degrade under the conditions of a vacuum, hence only samples which are completely anhydrous can be imaged.

2.6 The Effect of Energy Input on the Aggregation Rate

2.6.1 The Test Case of Calcium Oxalate

The effect of energy input on the aggregation of calcium oxalate has been investigated and modeled in the past. Hounslow et al. (1988) developed a set of discretized population balance equations to model aggregation that included a term for the aggregation kernel. The aggregation kernel describes mechanisms involved in the aggregation of particles. Calcium oxalate was chosen as a test case for the model. They found that in a batch of constant volume, the aggregation of calcium oxalate was correctly predicted by the model if a size-independent aggregation kernel was chosen. Their model found excellent agreement between the modeled moments and the moments obtained from the particle size distributions. Size independent fits were also assumed by Bramley et al. (1996), when proposing a new method to extract aggregation rates from experimental data.

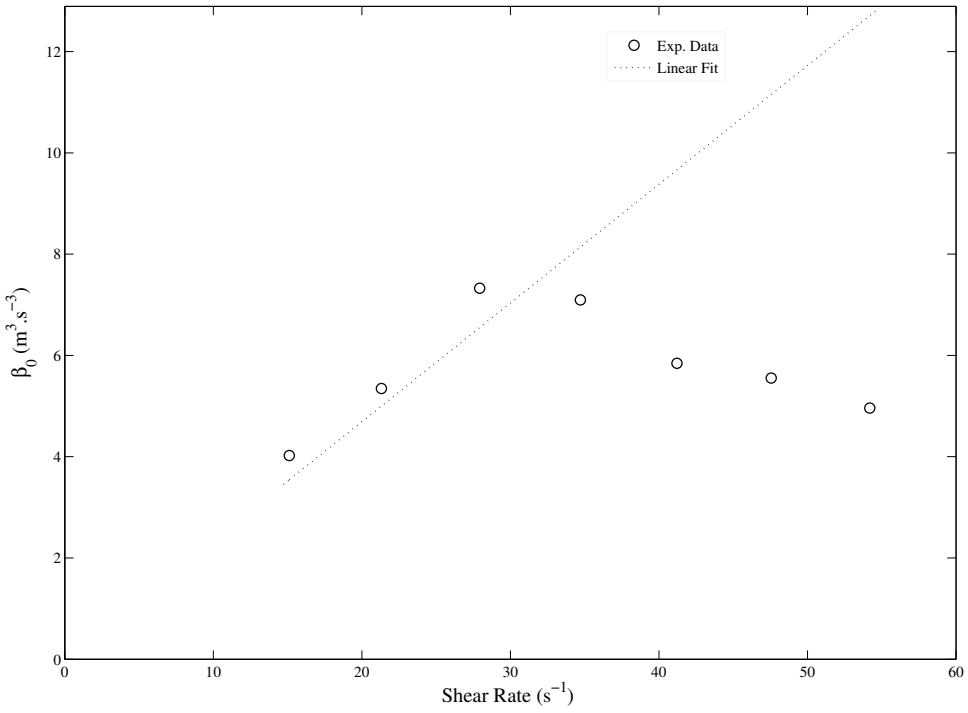

Figure 2.25: The aggregation rate constant as a function of the shear rate in a Couette flow reactor. (Hollander 2002)

A good fit was found between the experimental work and the model which assumed a size independent aggregation kernel. The aggregation rate constant as a function of the

energy input was studied by Hounslow et al. (2001); Bramley et al. (1997) and Hollander (2002). Hounslow et al. (2001) found that the rate of agitation (energy input) increased the possible number of collisions and therefore creates the opportunity for aggregation to occur, however it also has the limiting factor, that above a certain energy input, the aggregation rate constant decreases. The decrease in the collision efficiency is the predominant factor at higher energy inputs and and overall decrease in the aggregation rate constant is observed. This can be observed in the experimental results in figure 2.25 .

A maximum in the aggregation rate constant is observed between the shear rates of approximately 28 s^{-1} and $35s^{-1}$. A linear fit was applied to the four lowest shear rates. This was done as theory predicts that the aggregation rate is directly proportional to the shear rate up till the point at which the maximum aggregation rate constant is observed. The linear fit to the data was poor, with an R^2-value of only 0.75.

Hollander and co-workers(2002) used a Couette flow reactor to study aggregation in the calcium oxalate system by developing non-intrusive measurement techniques. The advantage of the Couette flow reactor is that it can be operated at constant shear rate across the region of interest. However, this is only possible at low Reynolds numbers in the laminar flow region. The low Reynolds numbers mean that there is very little turbulence and minimal mixing. Because of the lack of mixing, the experimental design had to be changed significantly. Seed particles were first prepared separately in a baffled stirred reactor and then introduced into the Couette flow reactor. The measured aggregation rate constants reported in this work only apply to systems with a very low energy input.

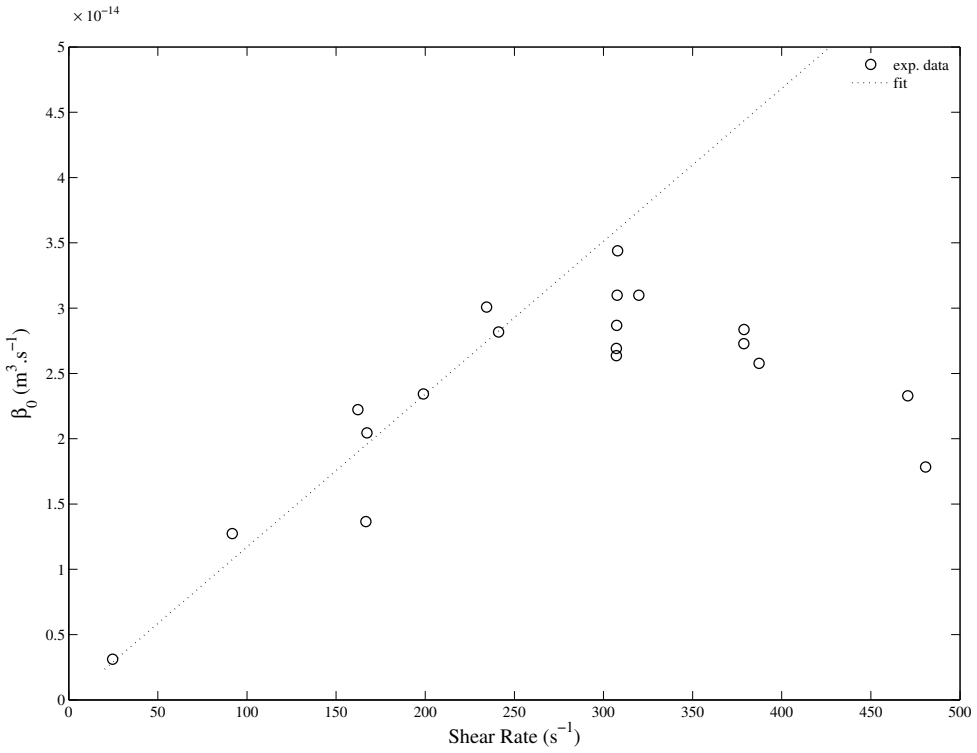

Figure 2.26: The aggregation rate constant of calcium oxalate for various shear rates found in a Poiseuille flow reactor. (Mumtaz and Hounslow 2000)

Mumtaz and Hounslow (2000) conducted similar experiments in a Poiseuille flow reactor, which has a well-defined velocity profile (parabolic) and predictable hydrodynamic conditions. The reactor develops a flow field that has a high shear at the wall of the reactor and zero shear in the center, which translates to a zero velocity at the wall, and a maximum in the center. Because of these flow characteristics, an average shear rate across the pipe had to be assumed. In their work the shear rates were varied from as low as $19s^{-1}$ all the way up to $480s^{-1}$. They found a maximum aggregation rate constant at $\langle\dot{\gamma}\rangle = 300s^{-1}$, which is much higher than previously found. Their linear fit to the experimental data up to the point that the maximum aggregation rate constant was found was significantly better than that of Hollander with an R^2-value of 0.92. At shear rates above $300s^{-1}$, they found that the aggregation rate constant decreased.

2.6.2 In Nearly Isotropic and Homogenous Turbulence

The coagulation of 3.9 μm polystyrene microspheres using a single oscillating grid was studied by Brunk and co-workers (1998). Initially a monodisperse solution of particles was introduced into the reactor. By monitoring the decrease in the number of singlet particles, the coagulation rate could be determined as a function of time and energy

input. Via direct measurements of the PSD and a comparison to theoretical modes, the coagulation rate was shown to depend significantly on particle interactions and the shear rate. The turbulence in this reactor is isotropic, however since only a single grid was used, the turbulence decays rapidly away from the grid. Derksen (2012) modeled the aggregation of mono-sized spherical particles of Kolomogorov scale in a homogenous isotropic environment. He showed, using direct numerical simulations, that the PSDs depended on both the power input as well as the strength of the forces acting between particles.

2.7 Summary

The purpose of this review of the relevant literature was to determine where there is a gap in the literature as well as guide the experimental procedures and methods required to investigate the problem at hand. The aggregation of particles has indeed been well studied in the past. Among the many factors which can have an effect on the aggregation, the turbulence and hydrodynamic forces experienced by the particles in solution is one of the most important. Therefore, it is just as important to understand the type of turbulence and shear forces as a function of the energy input present in the various reactors.

The oscillating multi-grid reactor provides an reactor wherein to study the aggregation of particles because it produces nearly homogenous and isotropic turbulence. This means that all the particles in the solution will be experiencing similar forces throughout the reactor. The RMS velocity is small across the reactor as well. The test system is that of calcium oxalate. It has been already been significantly studied in a wide variety of reactors, however never in an OMR. From the literature on calcium oxalate, it is evident that the treatment of the sample can greatly influence what is ascertained from them. An important consideration is the formation of the various hydrates of calcium oxalate, of which the monohydrate is the thermodynamically stable form. The precipitates have been shown to suffer from aging. If samples are kept for periods of longer than 24 hours, any hydrate other than that of COM will decompose into the monohydrate. The typical sample preparation methods used for scanning electron microscopy or x-ray diffraction, the filtering and drying of samples, including being placed under a vacuum, will potentially cause the decomposition to the monohydrate for of calcium oxalate. The sampling techniques chosen to investigate the effect of energy input on the aggregation rate of calcium oxalate in the OMR is laser diffraction to determine the particle size distribution, and additional techniques like optical microscopy and atomic absorption spectrometry will be implemented to charecterise the hydrates of calcium oxalate formed as well as determine the amount of calcium ions remaining in solution after precipitation. The particle size

distributions will be analysed using moment transformations to determine the aggregation rate constant for various energy inputs.

Chapter 3

Materials and Methods

The experiments to determine the effect of energy input on the aggregation rate of calcium oxalate precipitates were conducted in the oscillating multi-grid reactor. The OMR provided one of the most ideal setups to investigate the effect of energy input and shear rates on the aggregation of precipitates. For various reasons to be discussed in a later chapter, only unseeded experiments will be conducted. Particle sizing techniques were used to determine particle size distributions at various time intervals. As particles aggregate, so should there be a change in the particle size distributions. Using various mathematical transforms, it was possible to determine the aggregation rate constant of calcium oxalate. The OMR was operated at various energy inputs, and the aggregation rate constant was determined for each energy input.

3.1 Preparation of the Solutions

Solutions of calcium chloride ($CaCl_2$) (Merk, South Africa) and sodium oxalate ($Na_2C_2O_4$) (Sigma-Aldrich Co., Germany) were prepared to concentrations of 0.01M and 0.001M respectively for the main set of experiments. Some additional concentrations were used to visually monitor the rate of nucleation. This is discussed below in §3.2.1. The solutions were buffered up to an ionic strength of 0.16M by the addition of sodium chloride (NaCl) (Merk, South Africa). All solutions were prepared using de-ionized water. For initial testing, small 5 liter batches of solutions were prepared. These solutions were prepared in 5 liter Schott bottles stirred with a magentic stirrer for a minimum of 3 hours. Large, 45 liter batches of solutions were also prepared in 50 liter drums to be used for repeat experiments. A hole was made in the lids of the drums to allow a mechanical stirrer to be used for the mixing. Once mixed the hole in the lid was sealed to prevent any evaporation. For consistency and repeatability of experiments, it was more ideal to prepare large batches of solution.

3.2 Preliminary Experiments

3.2.1 Induction Time

Some preliminary experiments were carried out to determine the effect of concentrations of the $CaCl_2$ and $Na_2C_2O_4$ on the induction time. The following solutions were prepared to ionic strengths of 0.16M by the addition of NaCl. $50ml$ of the $CaCl_2$ solution is placed in a small Erlenmeyer flask with a magnetic stirrer spinning vigourously. The $Na_2C_2O_4$ was poured in, and a timer was started. Calcium oxalate forms a white precipitate and nucleation was easily observed. The moment the solution became slightly opaque, the time was recorded. Experiments where conducted at the laboratory temperature of $\sim 21\,^{\circ}$C.

	$c_{\text{init}}(\text{Ca})$	$c_{\text{init}}(C_2O_4)$
1.	0.01M	0.001M
2.	0.02M	0.002M
3.	0.06M	0.006M
4.	0.08M	0.008M
5.	0.05M	0.002M

Table 3.1: Solutions prepared to measure the rate of nucleation of $Ca_2C_2O_4$ for various concentration of $CaCl_2$ and $Na_2C_2O_4$

3.2.2 Characterisation of Hydrates using Optical Microscopy

Using solutions prepared in the same manner as in §3.1, bench top experiments were conducted to determine whether it was possible to use the optical microscope to charecterise the form of calcium oxalate which is precipitated when the $CaCl_2$ solutions was mixed with the $Na_2C_2O_4$ solution. As above, $50ml$ of each solution was placed in a Erlenmeyer flask and stirred vigourously with a magnetic stirrer. Once nucleation was observed, samples were pipetted onto glass slides and photographed under the microscope. Experiments were conducted at the laboratory temperature of $\sim 21\,^{\circ}$C.

3.3 Experimental Setup

The OMR has a volume of 10 liters and contains 19 evenly spaced circular grids with a square pattern. The OMR has two inlets at the top of the reactor. One was used to feed the mixed solutions into the reactor, the second, as the inlet for the recycle stream. The additional specifications for the OMR are given in 3.2. The solutions were pumped from their respective storage containers using a single peristaltic pump. Silicone tubing of equal lengths were connected to a Y-mixer, with the peristaltic pump placed between

the Y-mixer and the reactor. This setup up ensures that equal amounts of each solution are fed into the reactor. Secondly the Y-mixer, the length of the tubing after the Y-mixer as well as the high flow rate, guarantees that the two solutions will be well mixed when they enter into the reactor. The peristaltic pump which operates on the recycle stream is switched on as soon as the reactor begins to fill to avoid the effect of gravitational settling and to create a small net flow rate through the reactor. Peristaltic pumps are one of the more ideal pumps when dealing with flocs and aggregates as they produce very low shear rates. Capsules of the solution are drawn into the pump head under vacuum and they are pulled through the pipe until they exit the pump head. With a large enough internal diameter of the pipe (80 mm Watson-Marlow tubing) the effect of pumping on the formation of aggregates is reduced further. The reactor takes approximately nine and a half minutes to fill to a volume of 10 liters. By this point nucleation has already occurred. The grids are then made to oscillate at the desired frequency for the duration of the experimental run. All experiments were operated at atmospheric pressure and at the temperature of the laboratory, which was ± 21 $^{\circ}$C.

Reactor Specifications	
Diameter	180 mm
Height	380 mm
45^o conical base	
Number of grids	19
Distance between grids	20 mm
Stroke	18 mm
Mesh size	8 mm
Bar diameter	1 mm

Table 3.2: Oscillating Multi-Grid Reactor Specifications

Sampling occurred at the base of the reactor, using a small tap connected to the recycle stream. The peristaltic pump on the recycle stream had to be switched off when taking a sample. Approximately 150 ml of solution was drawn under gravity. This is to avoid imparting any further hydrodynamic stresses on the particles suspended in solutions. It can be assumed that the mixture inside the reactor is a homogenous mix and therefore removing 150ml of solution will not affect the concentration of particles remaining in the reactor. The sample then was also assumed to be representative of the conditions in the reactor at that point in time. 100 ml of the solution was be used to determine the particle size distribution. The remainder of the sample was to be used for optical microscopy and atomic absorption spectroscopy. Samples were taken every 10 minutes and the experiment was run for a duration of 60 minutes, with the zeroth minute being when the reactor was full.

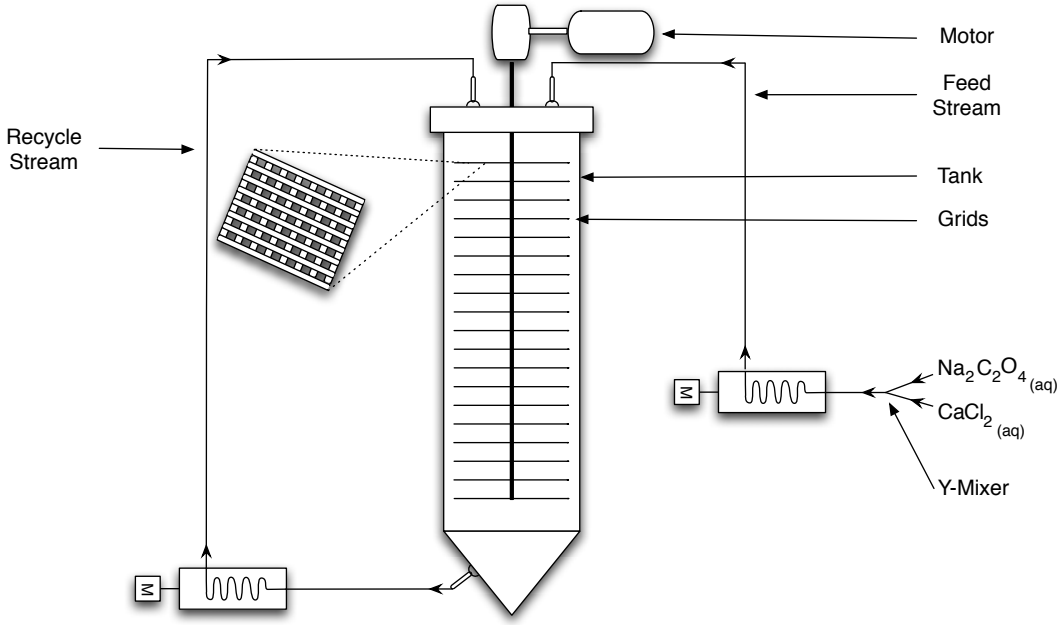

Figure 3.1: Experimental setup of the oscillating multi-grid reactor.

	$\langle\dot{\gamma}\rangle$
1	10.00
2	30.00
3	40.00
4	60.15
5	72.13
6	91.42
7	126.77

Table 3.3: Operating shear rates inside the OMR

After the experiment had reached completion, the reactor was drained and the solution disposed of. The reactor was washed 3 times with tap water, and once with deionised water, each time allowing the water to flow through all the tubing.

3.3.1 Operating Conditions

The oscillating multi-grid reactor can operate at various energy inputs. The energy input is adjusted by adjusting the frequency of the oscillations of the grids. From the relations as described in §2.3.4.1, it is possible to estimate an average shear rate over the region swept out by each grid. The OMR was operated at the averaged shear rates as shown in table 3.3.

To quantify the effect of varying the energy input (shear rate) on the aggregation rate of calcium oxalate, experiments were conducted between average shear rates of $10\,s^{-1}$ up

to 126 s^{-1}. Volume based particle size distributions will be found using laser diffraction techniques for samples taken every 10 minutes for a duration of 60 minutes.

3.4 Particle Sizing and Characterization

3.4.1 Malvern Mastersizer S

The Malvern Mastersizer S was used to determine the particle size distribution of the samples. The Malvern Hydro 2000SM small volume dispersion unit was used as well. This unit allows for small volumes of sample to be used. It was not possible to use one of the more typical wet dispersion units as the obscuration was too low when the samples were added, and the results would not have been reliable. The normal operating procedure for the Malvern Mastersizer requires the user to input the refractive index and absorption of the particles to be sized as well as the refractive index of the dispersant, in this case it was that of water. The large volume dispersion unit has a volume of 800 ml, and would consume too much of the solution for the experiment to operate reliably. Secondly, to obtain the required level of obscuration, would require the addition of more sample than the unit was capable of holding, and some of the sample and dispersant would be lost to the overflow.

The Malvern Mastersizer was setup up with the Hydro 2000SM small dispersion unit. It has a low shear impeller, which also acts as the pump to move the sample into the optical cell for measurement. The impeller has to operate between 2500 RPM and 3000 RPM to pump the solution through the optical cell. For consistency it was operated as near to 2500 RPM as possible.

To be able to calculate number based distributions from volume based distributions it would normally be essential to know the volume of the sample used. However, it was found that only when undiluted samples were used in the particle sizer, without any dispersant, was the obscuration high enough for results to be accurate. The small volume dispersion unit was always washed three times with deionized water. This also washes out the optical cell inside the equipment. A background reading was also taken with deionized water and allowed to drain afterwards. The sample was then added, and the impeller turned on. The sample was then analysed for eight seconds (8000 sweeps), and this was repeated three times. The software determines a particle size distribution from the light scattering data for all three runs, as well as using the refractive indexes and absorption. The small volume dispersion unit is drained and prepared for the next sample.

3.4.2 Optical Microscopy

It is possible to classify the type of hydrate formed using optical microscopy. Basic particle sizing is also possible, as well as determining the shape factors for the various particles. An Olympus© BX-60 optical microscope and an attached digital camera was used for these purposes. A small drop of the sample was placed on a microscope cell counting chamber. This chamber has a small depression of 100 μm in depth. This prevents any aggregates from being damaged when a cover slip is placed on the slide. The microscope was fitted with a 40X magnification objective lens and a 10X magnification eye piece, with a total magnifying power of 400X. This allows for crystals of approximately 5 μm in size to be identifiable.

3.4.3 Atomic Absorption Spectrometry

Atomic Absorption Spectrometry (AAS) was used to find the concentration of calcium ions [Ca^{2+}] in the original $CaCl_2$ and NaCl solution, as well as in the samples drawn from the reactor. All samples were filtered through 0.22 μm NY syringe filters to remove precipitated material. The original calcium chloride solution was diluted 20 times with deionised water, and the samples after precipitation had occurred were diluted down 10 times. This was done for two reasons, firstly diluting the sample would decrease the likelihood of any further precipitation occurring after the samples were drawn and secondly, the measurement equipment has a predetermined range of concentration in which it can operate. If the absorbance was higher than that of the machine's specifications and out of the range of the standard curve, then samples needed to be diluted down with deionised water such that concentrations fell within the measurable range.

Chapter 4

Analysis and Results

In this chapter the analysis of the experimental data as well as the results will be presented with minimal comments. A full and complete discussion of the results is left for Chapter 5.

4.1 Preliminary Experiments

Preliminary experiments were conducted to determine the induction time with respect to initial concentrations of the solutions as well as determining whether optical microscopy is an adequate method to charecterise the various hydrates of calcium oxalate. All of the preliminary experiments were conducted in small Erlenmeyer flasks and stirred with magnetic stirrers.

4.1.1 Induction Time

The results from the induction time experiments and the dependence on the original concentrations of the reagents are given in table 4.1.

	$c_{\text{init}}(\text{Ca})$	$c_{\text{init}}(\text{C}_2\text{O}_4)$	Induction time (s)	
1.	0.01M	0.001M	4.5 min	$\pm$6.8
2.	0.02M	0.002M	69.3	$\pm$2.9
3.	0.06M	0.006M	3.1	$\pm$1.3
4.	0.08M	0.008M	$\sim$0	-
5.	0.05M	0.002M	30.1	-

Table 4.1: Results of the bench top induction time experiments for various concentration of $CaCl_2$ and $Na_2C_2O_4$.

It is apparent that, at low concentrations, the induction time is much greater than at higher concentrations. This is expected, as the supersaturation of the mixed solutions

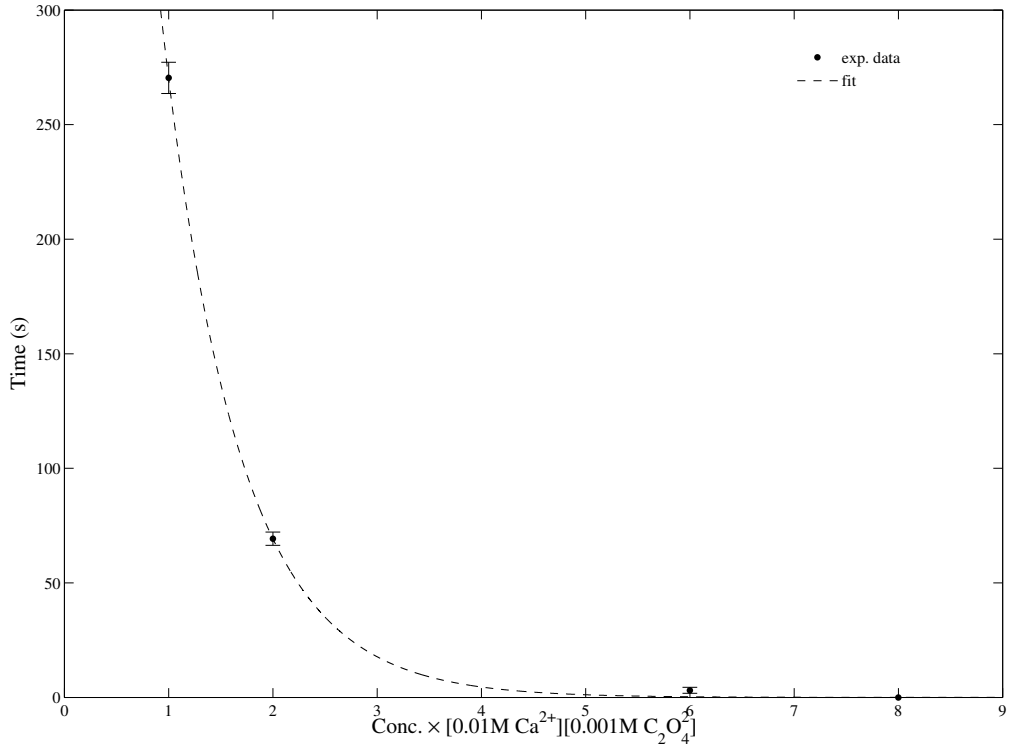

Figure 4.1: The induction time plotted as a function of the concentration represented as multiples of $[0.01\mathrm{M}Ca^{2+}][0.001\mathrm{M}C_2O_4^{2-}]$.

will be much greater at higher concentration of the reagents. The result in experiment (4.) shows near spontaneous nucleation. Concentrations of less than those of in (1.) were not tested as they will fall below relevant literature values. In figure 4.1, a power law curve is fitted to the data, resulting in the following relationship between the induction time and the concentrations,

$$t_{induction} = 3 \times 10^{-3}([\mathrm{Ca}^{2+}][\mathrm{C_2O_4}^{2-}])^{-0.99}. \tag{4.1}$$

4.1.2 Characterisation of Hydrates using Optical Microscopy

The following images were captured using the optical microscope after allowing for the nucleation of precipitates to be formed. At magnification of 200X , it is possible to determine the type of hydrates formed.

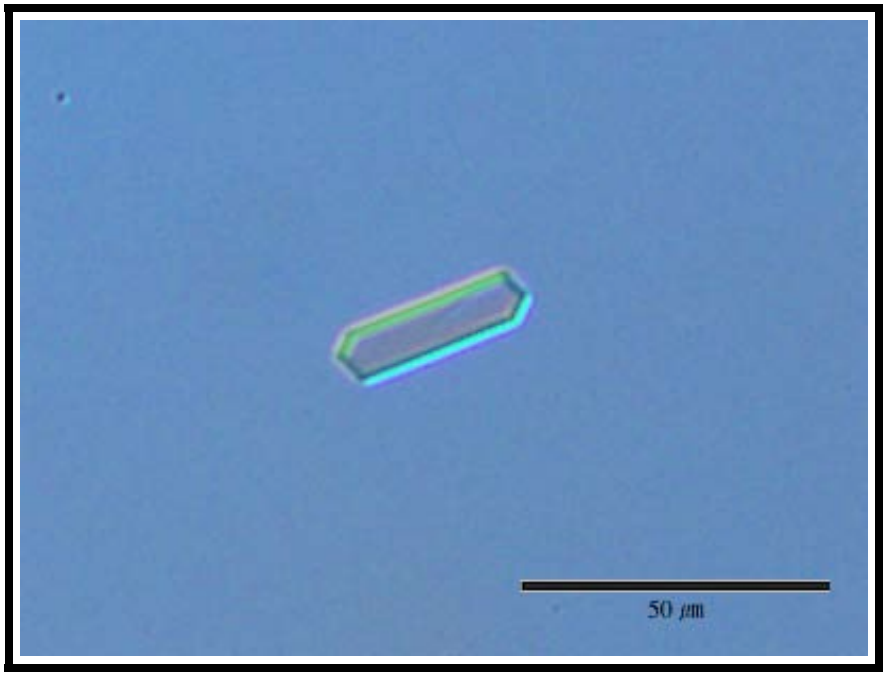

Figure 4.2: Single COM crystal.

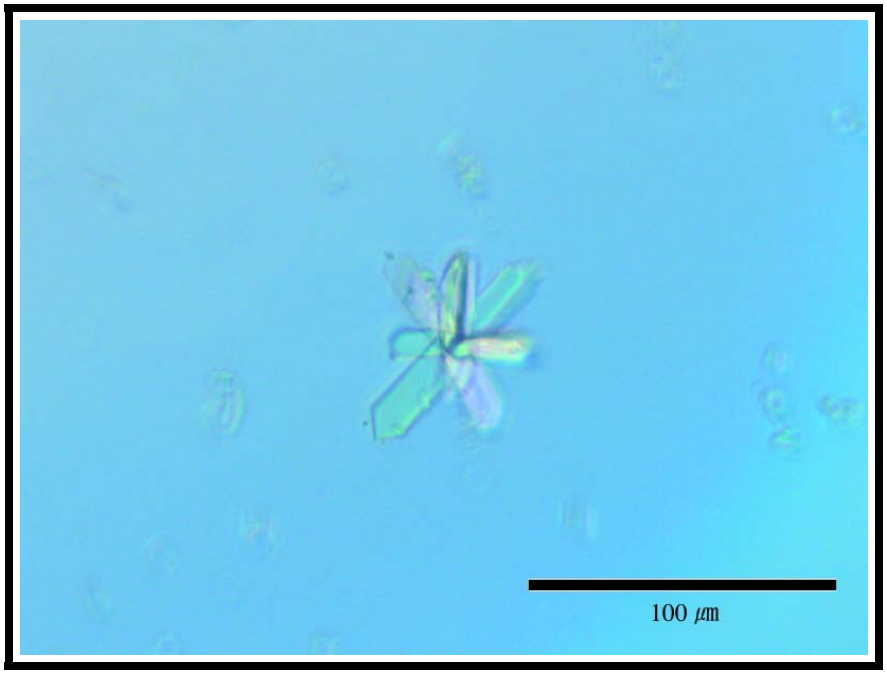

Figure 4.3: A weak aggregate of COM crystals.

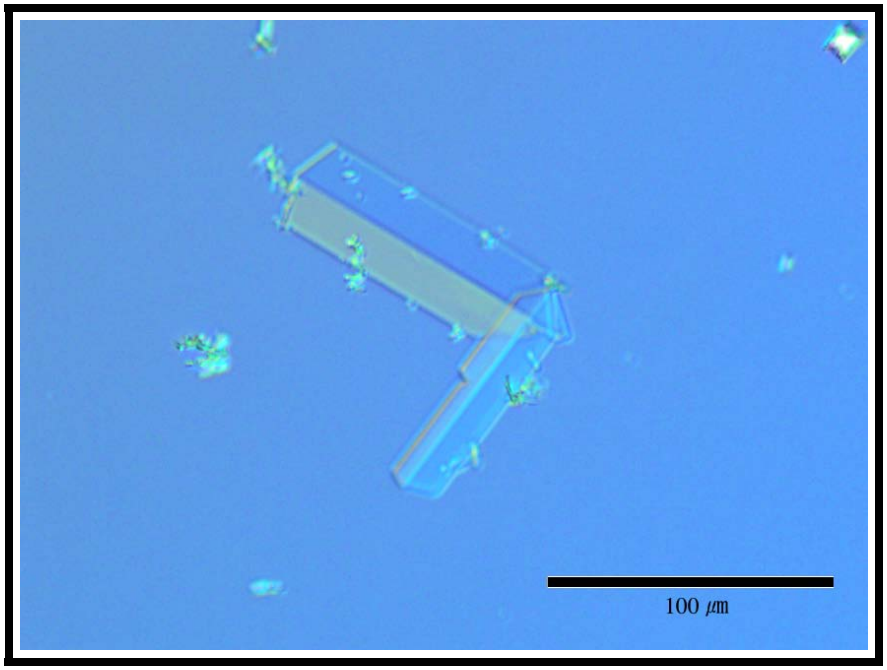

Figure 4.4: COM crystal with microcrystalline aggregates attached.

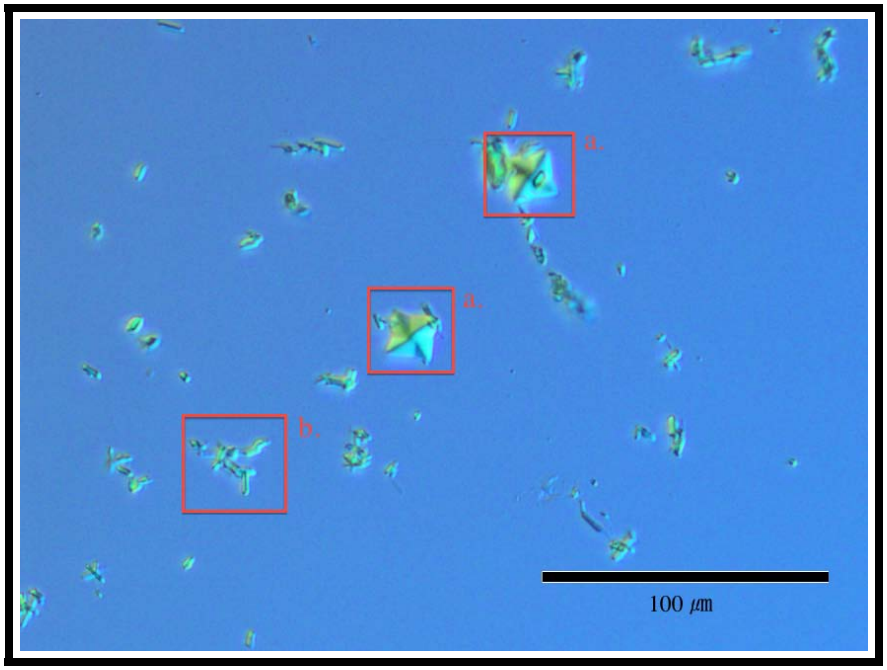

Figure 4.5: a. COD crystals are easily seen by their octahedral bipyramidal structure. b. This could be microcrystalline aggregates of COD or COT.

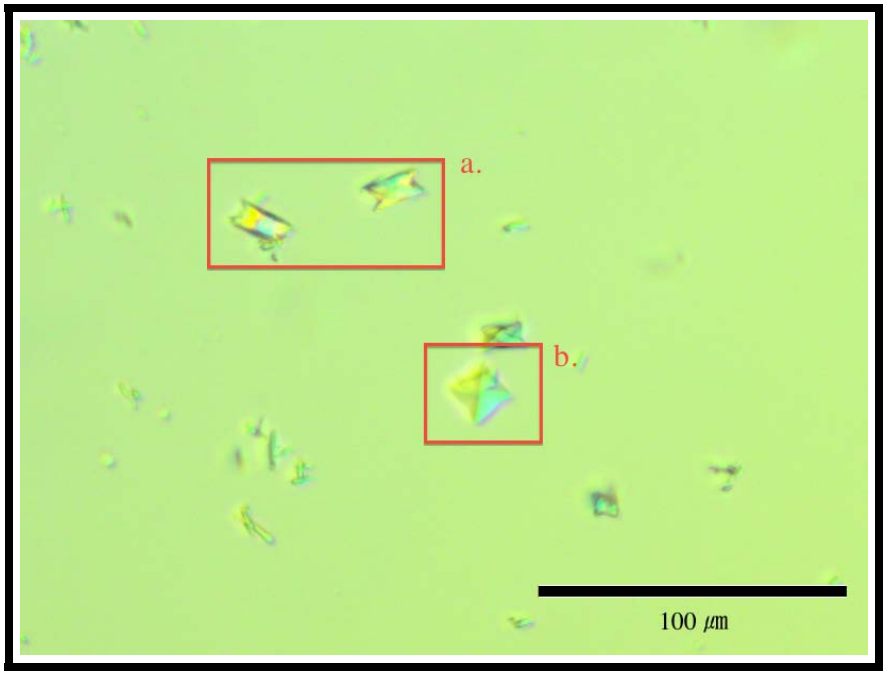

Figure 4.6: a. Twinned particles of COM. b. BP COD

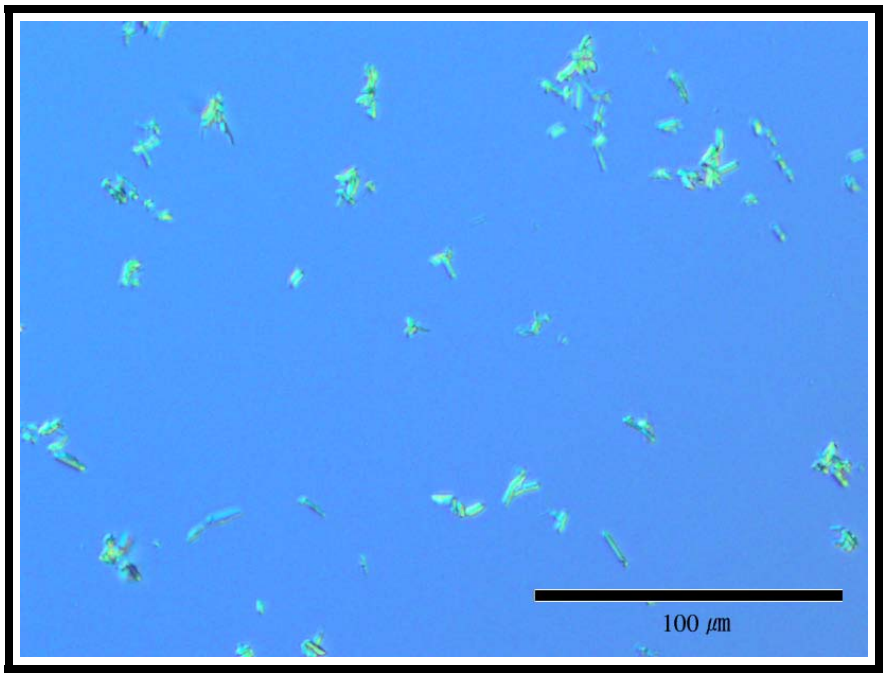

Figure 4.7: Needle like COT crystals.

4.2 The Effect of Energy Input on the Aggregation Rate

The volume based distributions were transformed to number based distributions under the assumption that the particles were spherical (shape factors are discussed in §4.2.4.1), as shown in figure 4.8. As described in §2.2.6, moments were found for the distributions and this allowed for the calculation of the aggregation rate constant.

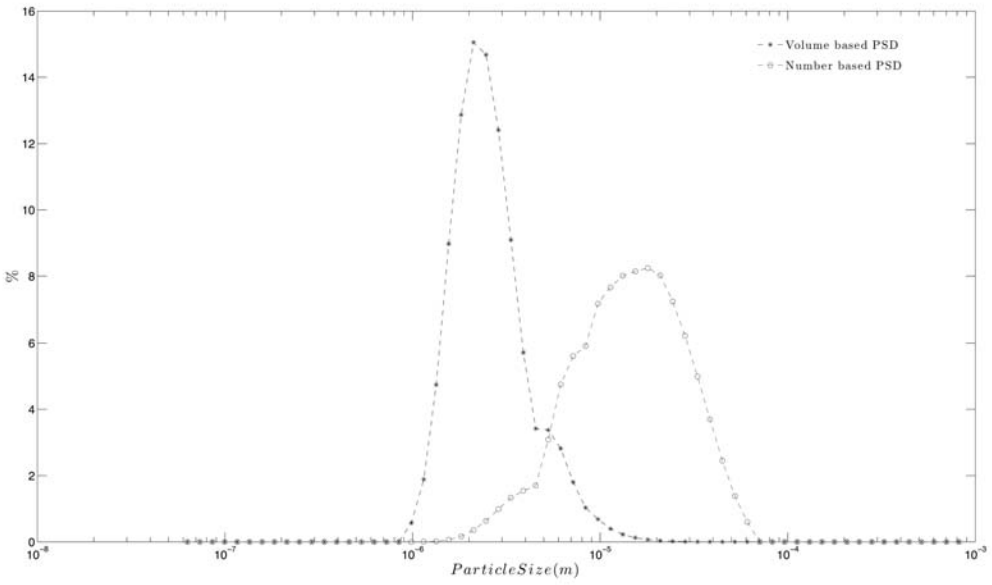

Figure 4.8: A volume based PSD transformed to a number based PSD.

4.2.1 Particle Size Distributions

A selection of particle size distributions are shown in figure 4.9. Each subplot shows the change in the particle size distribution over the 60 minute duration of the experiment. In figure 4.10, the PSDs are represented in a different manner. These plots are used to depict the shift, narrowing and decrease in the PSDs during aggregation. The colour scale represents the number of particles.

4.2.2 Total Numbers of Particles, m_0

The zeroth moment, which represents the total number of particles, is represented in two different manners in figures 4.11 and 4.12. The first plot has been nomalised with respect to the value of m_0 at t_0. It allows for the differences in the rates of change of m_0 to be

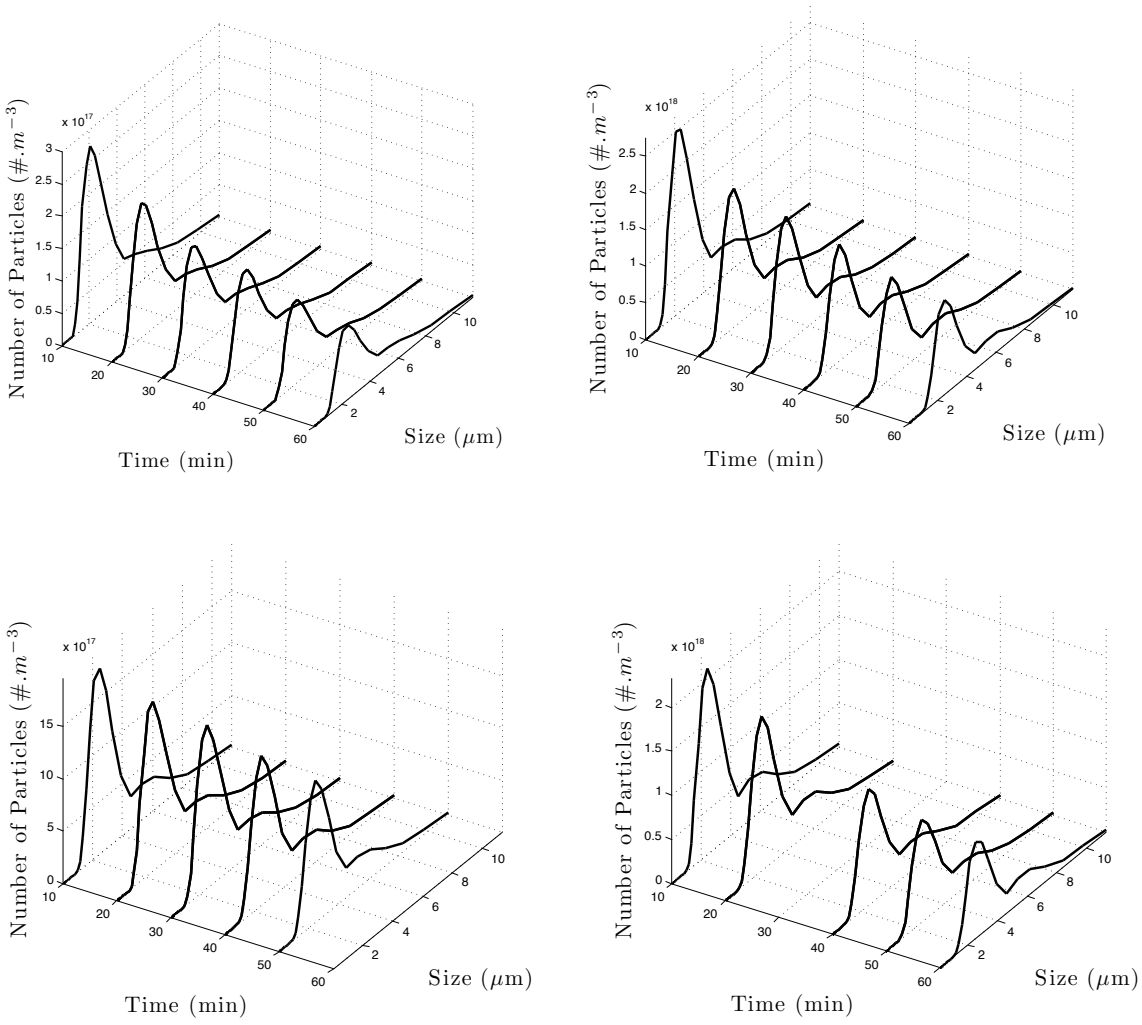

Figure 4.9: Particle size distributions by number for various shear rates. Clockwise from top left, the particle size distributions for shear rates $60s^{-1}$,$72s^{-1}$,$91s^{-1}$ and 127 s^{-1}.

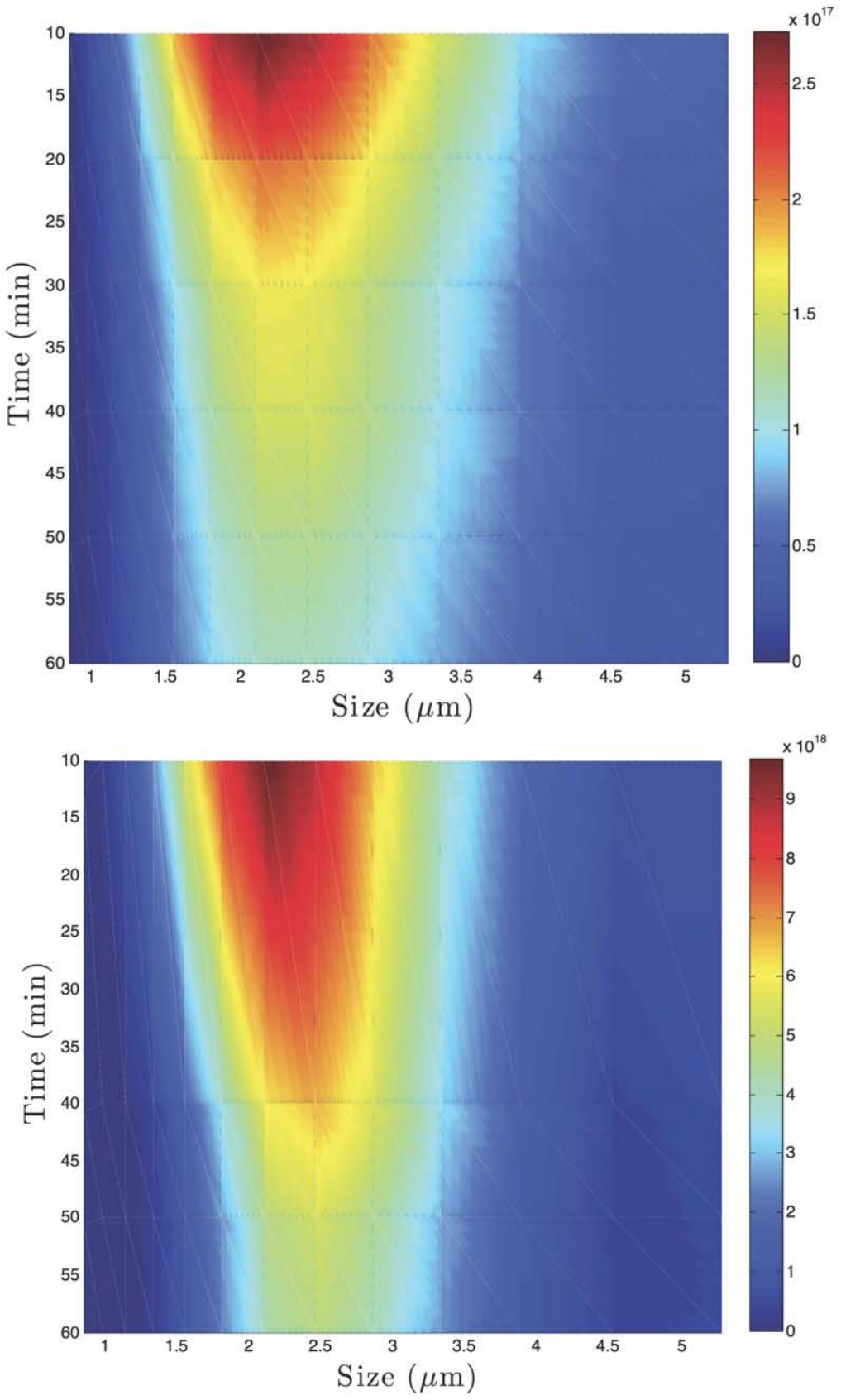

Figure 4.10: Particle size distributions represented in a manner to emphasize the shift of the peak to larger particle sizes as well as a narrowing of the distribution as the experiment progresses. The top plot is for a shear rate of $60s^{-1}$ and the bottom, $91s^{-1}$.

compared between experiments, regardless of the initial values of m_0. The second plot depicts the total particle numbers for the various sample times.

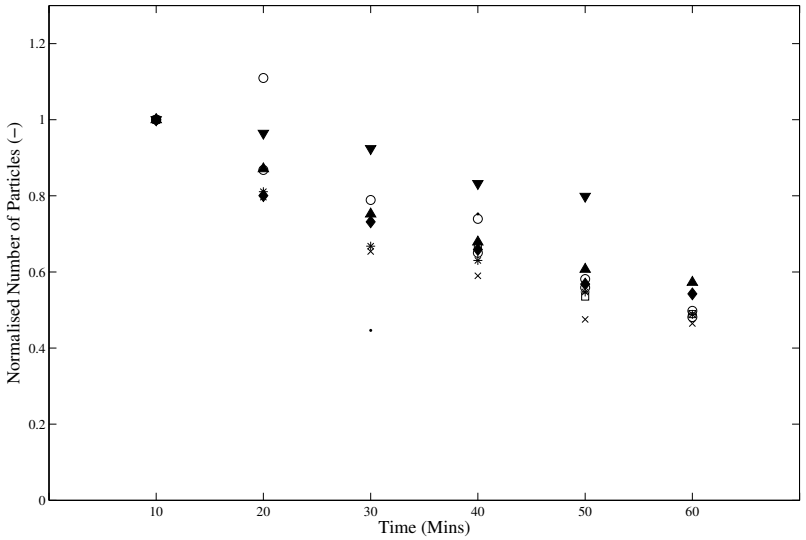

Figure 4.11: The normalised (with respect to the $t = 10min$) total number of particles as a function of the time. The following shear rates are represented, $10s^{-1}$ (○),30 s^{-1}(□),$40s^{-1}$(×),$60s^{-1}$(+,∗),$72s^{-1}$(⧫),$91s^{-1}$(▼) and 127 s^{-1}(▲).

4.2.3 Total Volume of Particles, m_3

The third moment represents the total volume of all the particles in the sample. Figure 4.13 shows the percentage volume fraction of solids as determined from the Malvern Mastersizer. The average volume of solids calculated from all the data in figure 4.13 is $0.0060\% \pm 0.0002\%$. The normalised total volume with respect to the total volume of the initial sample is shown in figure 4.14. The normalised plot allows for comparisons and trends to be more easily observed. Finally the total volume of the particles is depicted in figure 4.15.

4.2.3.1 ANOVA Analysis

An ANOVA analysis was performed on the data from the experiments. In particular, what was of interest was whether the volume of particles was statistically conserved (after taking into account the measurement errors). A single factor ANOVA analysis was performed on all of the the volume of solids fractions data as depicted in figure 4.13. A second ANOVA test was performed on a subset of the data. Only the 10, 20 and 30 minutes samples results were considered. The null hypothesis for both ANOVA tests is;

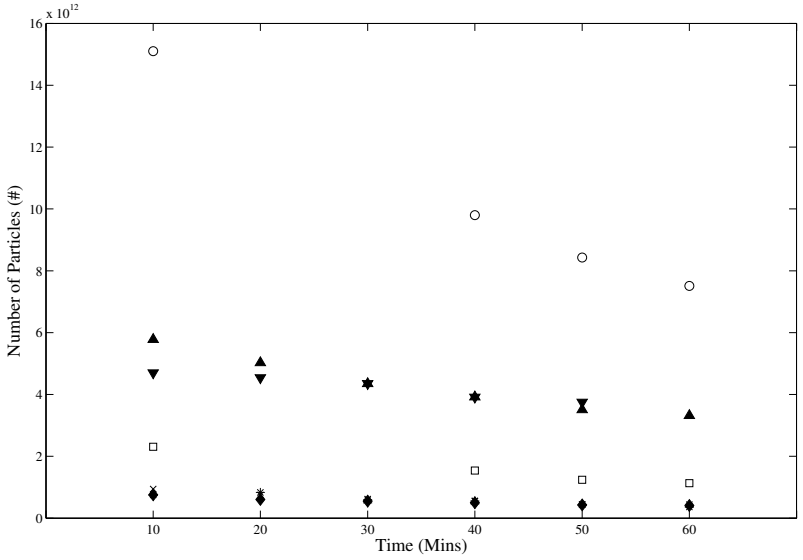

Figure 4.12: Total number of particles, m_0, as a function of the time . The following shear rates are represented, $10s^{-1}$ ($\circ$), 30 s^{-1}($\square$), $40s^{-1}$($\times$), $60s^{-1}$(+,$*$), $72s^{-1}$($\blacklozenge$), $91s^{-1}$($\blacktriangledown$) and 127 s^{-1}($\blacktriangle$).

Sample time (mins)	Mean (% $\times 10^{-3}$)	Variance (% $\times 10^{-6}$)
10	6.60	1.67
20	6.77	1.87
30	6.50	2.02
40	5.97	1.76
50	5.31	1.58
60	5.00	1.50

Table 4.2: Means and variances are calculated across the data set for each sample time. These are used during the ANOVA analysis

H_0: There is no significant difference between the volume of solids fraction with respect to sampling time.

H_1: One of the volume of solids fractions for a sample time is significantly different.

The results from the tests are shown in tables 4.3 and 4.4.

4.2.4 Optical Microscopy

An optical microscope with a magnification of 200X or 400X times was used to identify the type of hydrates of calcium oxalate formed as well as determine a shape factor of the particles using built in image analyzing software.

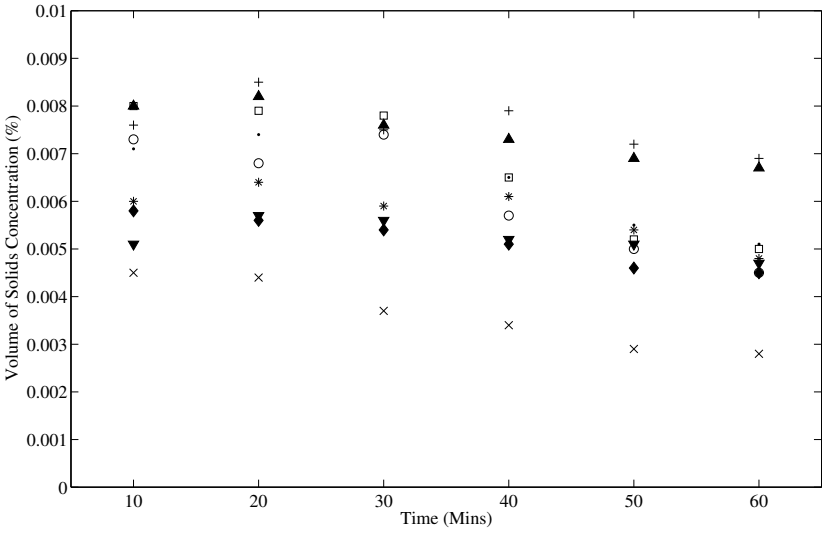

Figure 4.13: Total volume of solids expressed a percentage of the solutions. The following shear rates are represented, $10s^{-1}$ (○), 30 s^{-1}(□), $40s^{-1}$(×), $60s^{-1}$(●,+,∗), $72s^{-1}$(⧫), $91s^{-1}$(▼) and 127 s^{-1}(▲).

Source of Variation	SS	degrees of freedom	MS	F	p-level	F crit
Between Sample Times	2.40×10^{-5}	5	4.81×10^{-6}	2.78	0.028	2.99
Within Sample Times	8.31×10^{-5}	48	1.73×10^{-6}			
Total	1.07×10^{-4}	53				

Table 4.3: One way analysis of variance test on the volume of solids fraction of all the data at the 2.5% significance level.

4.2.4.1 Shape Factor

The shape factor was determined for 36 particles chosen from a series of images taken throughout the experimental runs. This includes the images shown in figures 4.16, 4.17 and 4.18. The shape factor, f_{circ}, was determined using the following formula,

$$f_{circ} = \frac{4\pi A}{P^2}, \tag{4.2}$$

where A is the projected area of the particle and P the measurable perimeter. A

Source of Variation	SS	degrees of freedom	MS	F	p-level	F crit
Between Sample Times	3.27×10^{-7}	2	1.63×10^{-7}	0.088	0.91	3.40
Within Sample Times	4.44×10^{-5}	24	1.85×10^{-6}			
Total	4.48×10^{-5}	26				

Table 4.4: One way analysis of variance test on the volume of solids fraction of all the 10, 20 and 30 minute data at the 5% significance level.

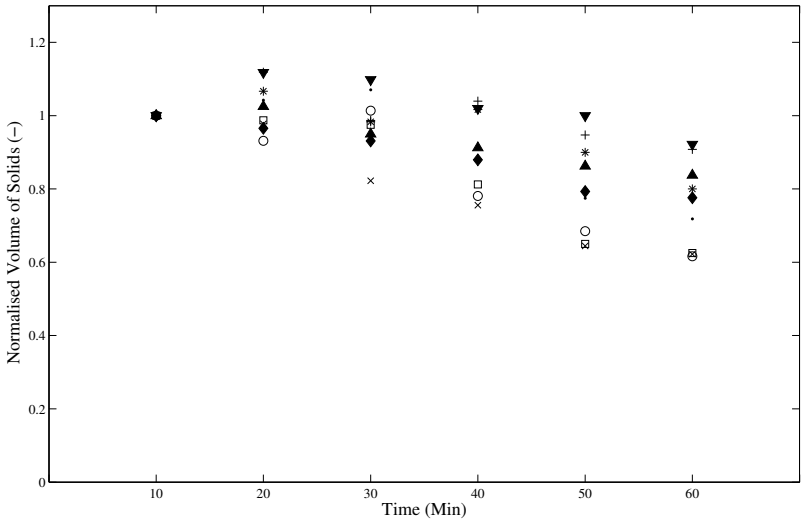

Figure 4.14: The normalised volume of solids with respect to the volume of solids calculated at $t = 10min$, the first sample. The following shear rates are represented, $10s^{-1}$ (○), 30 s^{-1}(□), $40s^{-1}$(×), $60s^{-1}$(•,+,∗), $72s^{-1}$(⧫), $91s^{-1}$(▼) and 127 s^{-1}(▲).

perfect sphere or circle will have a value of 1 for f_{circ} . The aspect ratio, f_{AR} ,is another measure of the shape of a particle. It is the ratio of the minimum width to the maximum length of the particle.

$$f_{AR} = \frac{D_{min}}{D_{max}}, \tag{4.3}$$

where D_{min} is the minimum width of the particle and D_{max} is the maximum length. The aspect ratio will also have a value of 1 if the width and length are the same. The data aquired is shown in table 4.5.

4.2.5 Concentration of Calcium in Solution

AAS was performed on all samples. The samples were diluted to avoid further precipitation as well as to bring the concentrations of calcium into the measurable range of the equipment. The results from the AAS for samples taken at 10 min, 20 min and 60 min are presented in figure 4.19. The concentration of calcium remains constant for the duration of the experiment. This is as expected, since from the induction time experiments in §4.1.1, nucleation would have occurred by the time the first samples are taken. At constant temperature, it is valid to assume that there should be no dissolution of the precipitated material.

[1]Refer to apprendix C for how the measurement error of mean was propagated from the error in the measurement of each sample as represented by the RSD values.

	$D_{min}(\mu\text{m})$	$D_{max}(\mu\text{m})$	$P(\mu\text{m})$	$A(\mu\text{m}^2)$	f_{circ}(-)	f_{AR}(-)
1	17.81	40.19	98.28	372.55	0.48	0.85
2	23.33	30.81	95.46	398.26	0.55	0.92
3	29.72	32.61	114.56	466.70	0.45	0.95
4	20.85	39.53	115.52	423.97	0.40	0.85
5	8.18	21.98	52.01	127.71	0.59	0.87
6	9.42	26.89	62.73	200.20	0.64	0.85
7	9.19	52.75	115.35	308.27	0.29	0.93
8	27.98	40.12	116.36	403.85	0.37	0.89
9	37.07	45.19	148.70	911.37	0.52	0.93
10	5.88	18.39	44.12	74.39	0.48	0.92
11	6.63	20.03	46.49	97.36	0.57	0.88
12	16.49	24.84	84.35	228.77	0.40	0.92
13	6.17	12.72	31.87	56.42	0.70	0.90
14	6.34	15.23	36.73	72.13	0.67	0.85
15	17.76	23.82	70.69	214.24	0.54	0.90
16	15.63	30.14	87.33	223.65	0.37	0.86
17	9.11	26.15	61.97	166.04	0.54	0.90
18	10.01	45.24	103.73	307.20	0.36	0.93
19	10.96	19.29	54.79	125.93	0.53	0.87
20	15.49	23.32	73.13	225.55	0.53	0.89
21	16.04	32.42	81.61	321.25	0.61	0.87
22	13.74	24.50	62.48	214.84	0.69	0.86
23	12.15	17.33	46.88	108.67	0.62	0.89
24	7.11	18.67	43.83	100.46	0.66	0.85
25	7.25	16.17	40.42	74.39	0.57	0.88
26	9.03	28.61	67.41	192.82	0.53	0.89
27	32.09	66.80	196.57	839.96	0.27	0.89
28	24.93	40.58	110.12	580.37	0.60	0.88
29	16.60	32.50	83.63	261.02	0.47	0.86
30	9.62	17.90	44.74	102.36	0.64	0.87
31	11.48	19.86	52.02	152.47	0.71	0.88
32	11.88	27.68	75.80	269.12	0.59	0.95
33	16.85	32.99	84.52	342.32	0.60	0.84
34	9.37	35.82	82.12	231.62	0.43	0.90
35	9.17	26.16	60.39	171.16	0.59	0.87
36	12.44	27.87	69.56	264.47	0.69	0.87
				mean	0.53±0.002	0.89±0.0002

Table 4.5: The shape factors for a selection of 36 particles. Presented is the circularity and the elongation.

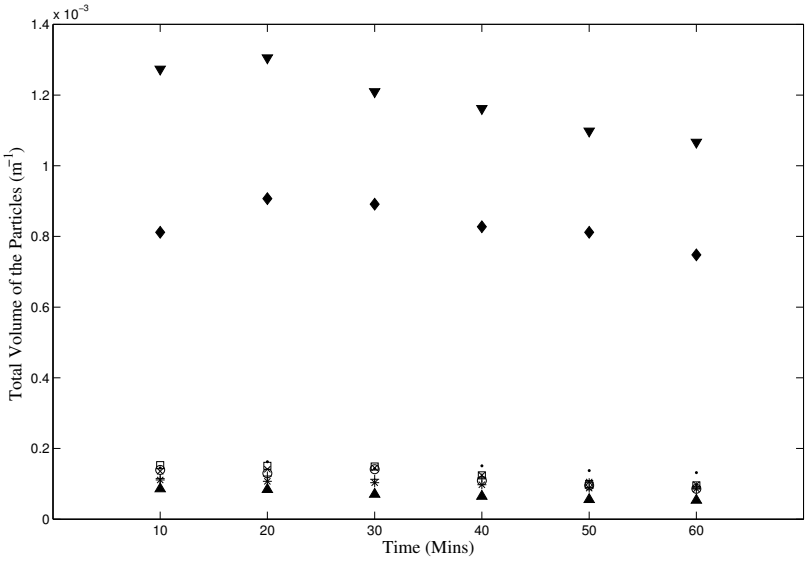

Figure 4.15: Total volume of solids. The following shear rates are represented, $10s^{-1}$ (○), 30 s^{-1}(□), $40s^{-1}$(×), $60s^{-1}$(•,+,∗), $72s^{-1}$(⧫), $91s^{-1}$(▼) and 127 s^{-1}(▲).

Sample	A.A.S. Conc (mg/l)	RSD	Conc. (mg/l)	
1.	17.17	0.3%	343.4	±1.0302
2.	17.05	0.8%	341.4	±2.728
3.	17.61	1.3%	352.2	±4.5786
mean			345.53	±1.809[1]

Table 4.6: Initial of concentrations of Ca^{2+}in solution before the calcium chloride and sodium oxalate solutions are mixed.

4.2.5.1 Derived Volume Fraction

It is possible to derive the volume fraction of solids contained in a sample since the concentrations of the calcium ions in solution were measured before and after the solutions were mixed and calcium oxalate was precipitated. A simple mass balance was used to determine the mass of the calcium precipitated out of solution as calcium oxalate monohydrate. This was found by calculating the difference between the initial average concentration of calcium ions in the solution as shown in table 4.6, and the concentration of calcium ions remaining in the solution (figure 4.19) after nucleation has taken place. Then using the density of calcium oxalate monohydrate ($2.12g.cm^{-3}$), the following volumes of solids as a fraction of the total samples were calculated and the results are shown in table 4.7. These can be directly compared to the solids volume fraction as calculated via laser diffraction. A t-test is shown in table 4.8. It allows for a comparison of the means from the two different methods.

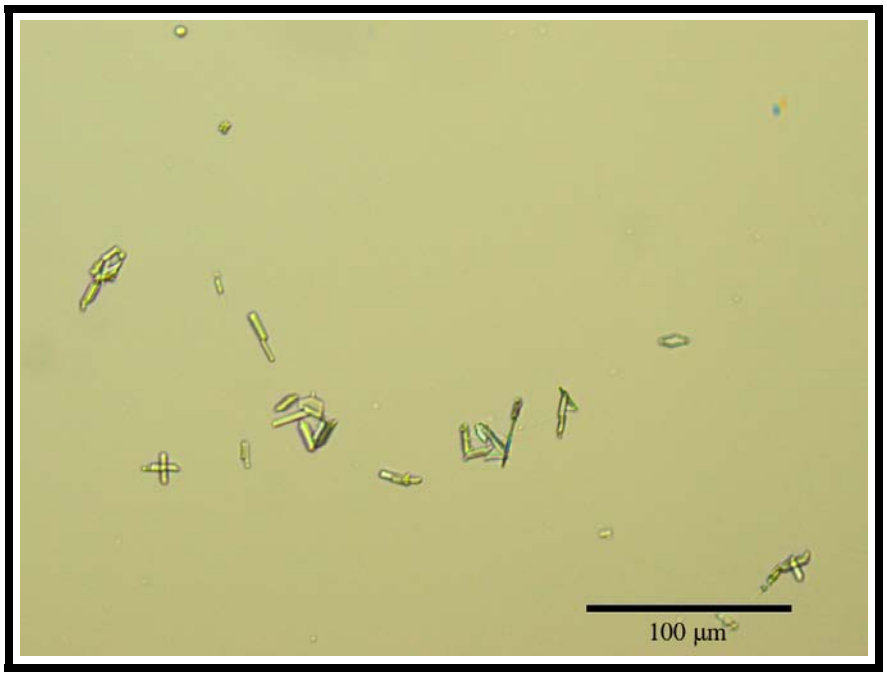

Figure 4.16: Weakly aggregated COM crystals with possibly some needle like COT crystals.

Ca Precipitated (mg)	Mols ($\times 10^4$)	M($Ca_2O_4 \cdot H_2O$) (g)	Volume (cm^3)	Solid Fraction (%)
35.3	8.81	0.13	0.06	0.0058
9.5	2.38	0.03	0.02	0.0016
22.2	5.55	0.08	0.04	0.0037
16.5	4.11	0.06	0.03	0.0027
66.0	1.65	0.24	0.11	0.0109
35.0	8.74	0.13	0.06	0.0058
40.8	1.02	0.15	0.07	0.0068
			mean	0.0053 ± 0.0011

Table 4.7: Volume of solids fraction as calculated from the AAS data.

4.2.6 Determination of the Aggregation Rate Constant

The aggregation rate constant for calcium oxalate as a function of the shear rate was determined using the moment transformations of the particle size distributions as described in §2.2.6. A brute-force optimisation scheme was used, because the simulation could be run quickly and only a single minima would be present. Aggregation rates constant varying from $\beta_0 = 1 \times 10^{-18}$to 1×10^{-10}, were tested, and the model is used to predict the values of m_0. For each β_0 tested, an optimisation function is used to determine how well the resulting curve fitted the data. This is typically known as the optimisation function. In this case, the optimisation function is the function to be minimised. . The sum of the difference between the predicted values of m_0 for a given β_0 and the observed (experimental)

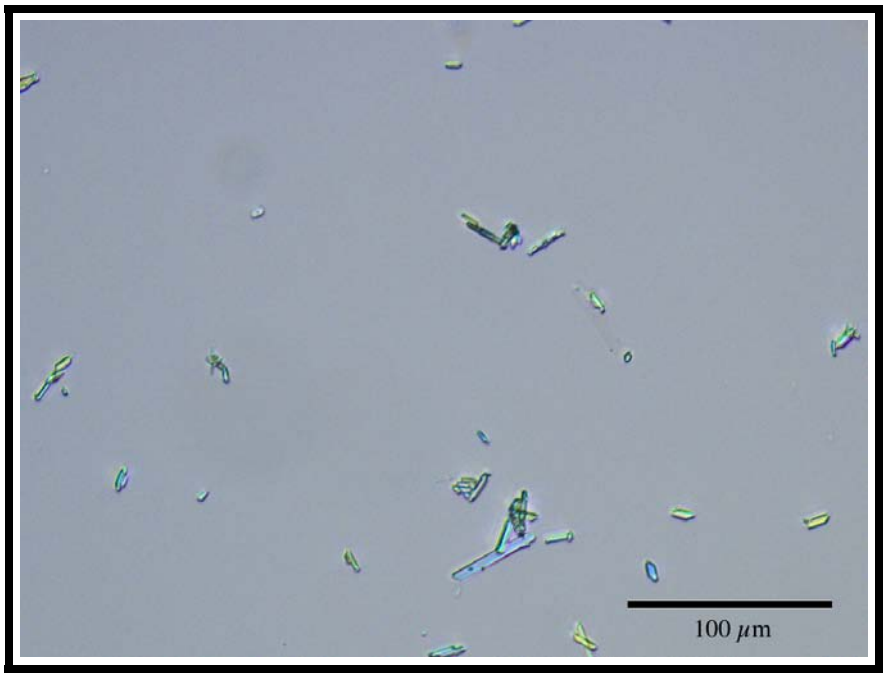

Figure 4.17: Weakly aggregated COM crystals.

Variable	Sample Size	Mean ($\times 10^3$)	Variance ($\times 10^6$)
AAS	7	5.34	9.61
Laser diffraction	54	6.02	2.02
Summary			
Degrees of freedom		59	
Hypothesized difference of the means		0	
Test statistic ($t_{\alpha=0.05} = 2.00$)		1.02	
p-value		0.31	

Table 4.8: t-test to ascertain whether the volume of solids derived from the AAS results is the same as that from the laser diffraction results.

results is the function to be minimised. It can be described as follows,

$$\min[C_i = \sum_{1}^{k}(E(x) - O(x))^2]. \tag{4.4}$$

Where i represents the i'th value of β_0 tested, k, is the number of experimental data point, $E(x)$ and $O(x)$ are the expected values obtained from the model and the observed values respectively. The minimum value for C is found and it can be related back to the optimal aggregation rate constant for a given experiment. The numerical algorithm is shown in appendix C, algorithm C.2. An example of the type of graph representing the how the algorithm will find the optimal value of β_0 for a given set of data is shown in figure 4.20. The algorithm uses a log transform to test the aggregation rate constant

Figure 4.18: Mostly COM crystals weakly aggregated and some needle like COT crystals.

and because of this the abscissa of figure 4.20 are given as $\log_{10}(\beta_0)$. The single minima of the optimisation function is clearly visible, and is at a value of $\log_{10}(\beta_0) = -14.23$. This was transformed by finding the inverse of the log and an aggregation rate constant of $\beta_0 = 10^{-14.23}$ or $5.88 \times 10^{-15} m^3.s^{-1}$ was determined.

The optimal aggregation rates for each shear rate at which the experiment was operated are shown in figure 4.22 and 4.21. The best-fit curves all find excellent agreement ($r^2 \geq 0.95$) with the experimental data as represented by the goodness-of-fit parameter, r^2.

The shear rates against which the aggregation rate constant plotted were calculated as an average of the shear rates between 0.01m and 0.02m above the center point for each oscillating grid using the integral from equation (2.36). The aggregation rates are depicted in figure 4.23, and the same data is shown in table 4.9.

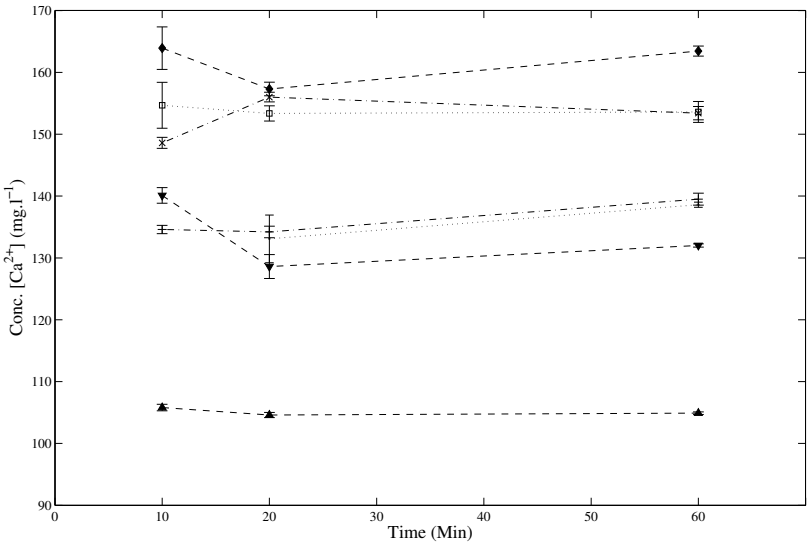

Figure 4.19: The concentration of calcium remaining in solution at 10 min, 20 min and 60 min.

$\langle\dot{\gamma}\rangle$ (s^{-1})	β_0 $(m^3.s^{-1})(\times 10^{15})$
10.0	2.512
30.0	2.042
40.0	53.703
60.1	40.580±7.400
72.1	5.888
91.4	2.570
126.8	5.495

Table 4.9: The aggregation rate constant of calcium oxalate precipitates as a function of the average shear rate.

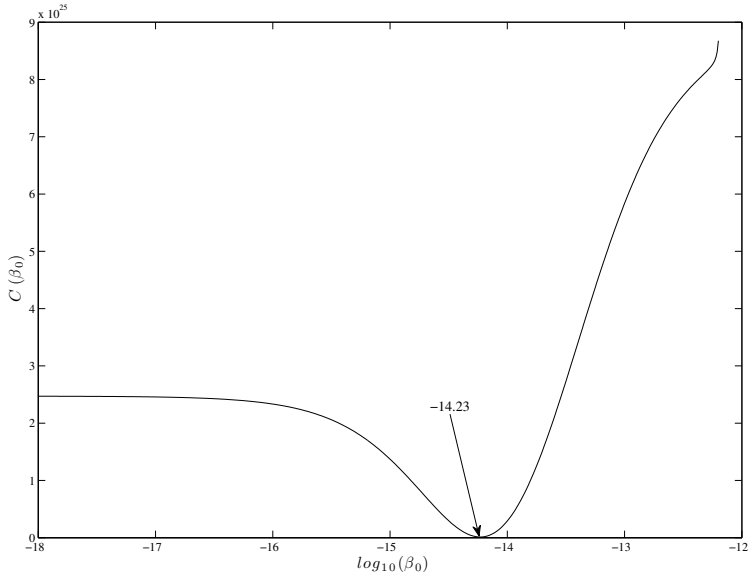

Figure 4.20: The cost function for the data representing a shear rate of $72.1s^{-1}$ as described in equation (4.4). The minimum can be seen to occur at -14.23, which relates to an aggregation rate constant of $10^{-14.23}$, or $\beta_0 = 5.88 \times 10^{-15} m^3.s^{-1}$.

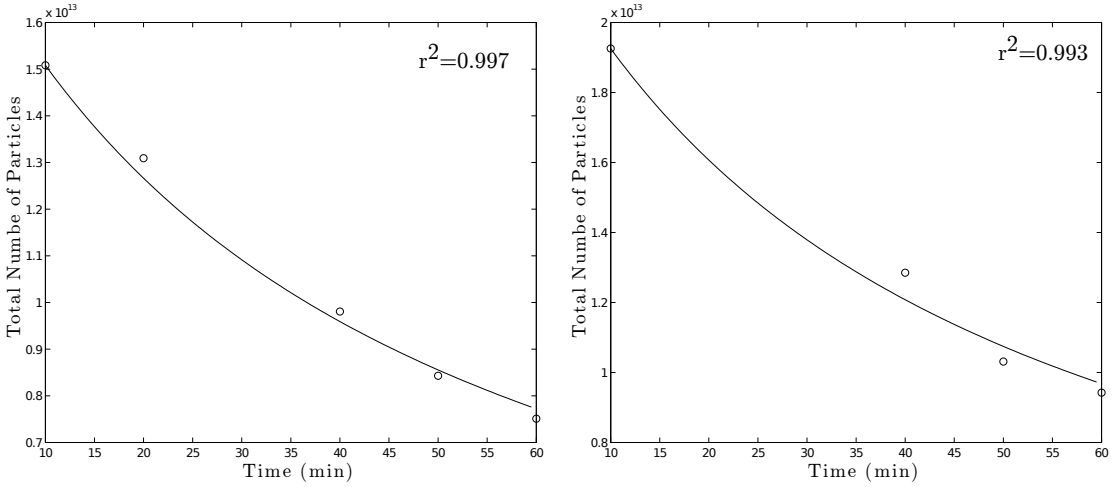

(a) A shear rate of 10 s^{-1} with an optimized $\beta_0 = 2.512 \times 10^{-15} m^3.s^{-1}$

(b) A shear rate of 30 s^{-1} with an optimized $\beta_0 = 2.042 \times 10^{-15} m^3.s^{-1}$

Figure 4.21: The resultant best-fit curves for each shear rate.

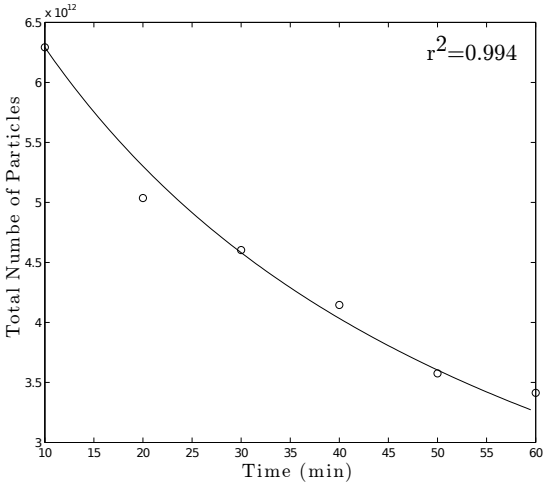

(a) A shear rate of 40 s^{-1} with an optimized $\beta_0 = 5.370 \times 10^{-14} m^3.s^{-1}$

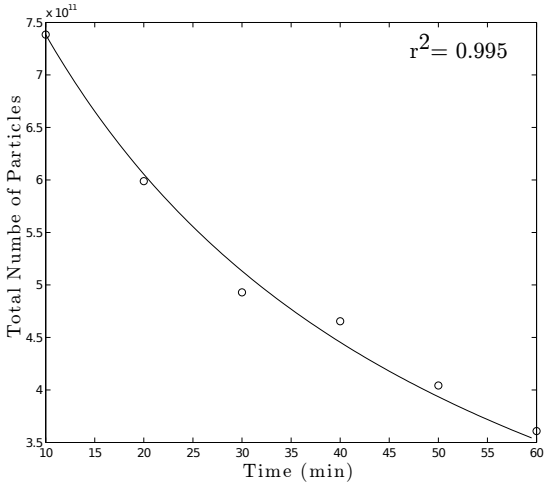

(b) A shear rate of 60.1 s^{-1} with an optimized $\beta_0 = 4.580 \times 10^{-14} m^3.s^{-1}$

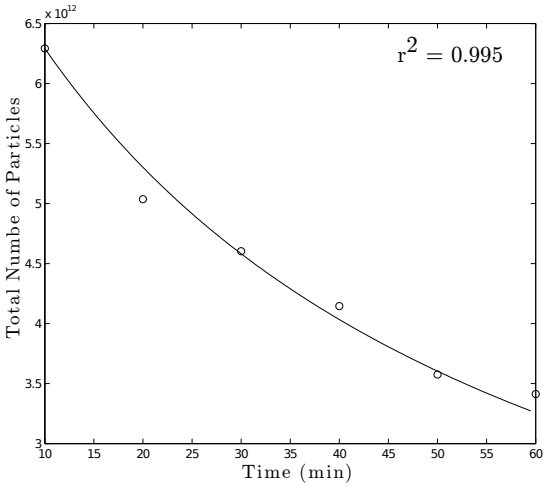

(c) A shear rate of 72 s^{-1} with an optimized $\beta_0 = 5.888 \times 10^{-15} m^3.s^{-1}$

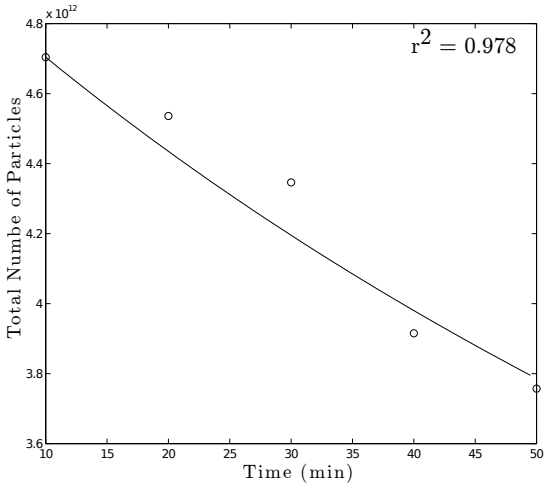

(d) A shear rate of 91.4 s^{-1} with a optimized $\beta_0 = 2.570 \times 10^{-15} m^3.s^{-1}$

Figure 4.22: The resultant best-fit curves for each shear rate.

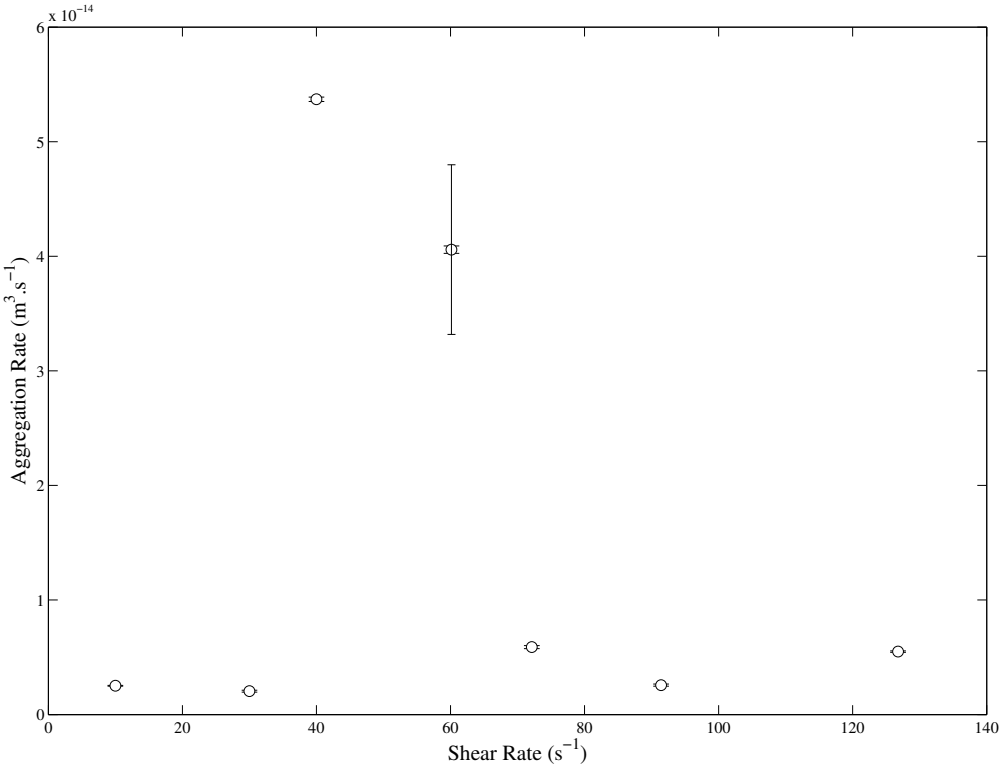

Figure 4.23: The aggregation rate constant of calcium oxalate precipitates as a function of the average shear rate.

Chapter 5

Discussion

5.1 Induction Time

The induction time experiments were simple bench top experiments conducted with Erlenmeyer flasks and magnetic stirrers. The purpose was to obtain some indication of the length of time it takes for visible nucleation to occur. It is easy to observe when nucleation has occurred since calcium oxalates precipitates as white crystals, and the turbidity of the solution increases significantly. From figure 4.1 it is clear that even with relatively small increases in the concentration, the induction times decrease rapidly. The induction time can be shown to decrease exponentially with increasing concentrations. The following parameters were found when fitting the exponential function of

$$t_{induction} = Ae^{-Bc},$$

where $A = 1054$ and $B = -1.361$ and an R^2-value of 0.9998. c is the product of the activities of the calcium and oxalate ions, otherwise known as the ion activity product ([IAP]). At the low concentration which the experiments were conducted at, those of 0.01M[Ca^{2+}]and 0.001M[$C_2O_4^{2-}$], the induction time was shown to be about 270 seconds. These concentrations are the ones generally used in the literature which will allow for , and also at these very long induction times, the need to have sufficient mixing becomes less important when compared to extremely rapid induction times where micro mixing would have a significant impact on the formation of the products. This long induction time is beneficial to the experimental setup as the reactor takes approximately nine and a half minutes to fill. It can be assumed that the two solutions are mixed well upon entering the reactor because the length of the tubing and the Y-mixer.

5.2 Characterisation of Hydrates

As expressed in chapter 2, there exist different hydrates and polymorphs of calcium oxalate. From the bench top experiments it was easy to identify them. Being able to clearly identify them using optical techniques was important as it would allow for a greater understanding of the mechanisms involved in the aggregation of the particles. Figures 4.2 to 4.7 clearly show that it is possible to identify the various hydrates of calcium oxalate. For example in figure 4.2, it can be seen that there is a single COM crystal. This crystal was formed shortly after the solutions were mixed and nucleation occurred. It can be compared to (a) in figure 2.11. Aggregates of COM are observed in figure 4.3 . This is an aggregate of the crystal shown in figure 4.2. It is likely to only be weakly aggregated. The information garnered from those preliminary experiments and from the literature, allowed for the identification of COM and COT crystals from samples taken from the OMR as evidenced in figures 4.16, 4.17 and 4.18, with the monohydrate being in the majority.

5.3 The Effect of Energy Input on Aggregation Rates

The effect of the energy input, or, as a proxy, the shear rate, upon the aggregation rate and aggregation rate constant is quantified through a series of calculations and transformation. The analysis eventually requires the analysis of the moments of number based particle size distributions, and in particular, how the moments changed with respect to time. The discussion below follows the order in which the experimental data was processed and used to eventually find the aggregation rate constant for a particular shear rate.

The transformation from a volume based PSD to a number based one, requires the used of a shape factor. The shape factor is necessary because the volume of any object is inherently dependent on the shape of the object. In this case, the object is the particle which is being measured. An appreciation of the shape of the particles is essential before making the transformation. Unless the particles are very dissimilar to a sphere, a typical shape factor of $\pi/6 \approx 0.5236$ is used. This shape factor relates the volumes of a cube which would completely contain the sphere within it. The proof of this relationship is shown in appendix D.

From the optical microscopy data in table 4.5, a calculated average shape factor was found by measuring the various characteristics of 36 randomly selected particles. It was found to be $f_{circ} = 0.53$. This is nearly identical to the standard shape factor, and justifies the use of using $\pi/6$ when making the transformations from the volume to the number based distributions.

The number based particle size distributions shown in figure 4.9 clearly show a decrease in the number of particles with respect to time. The peak size of the distributions decreases significantly as the experiments progress from the initial sample at t_0 to the final sample which is taken at 60 minutes. The decrease in the number of particles can only be due to the process of aggregation since dissolution is not present. It is the rate in the decrease in the total number of particles which is measured, and ultimately used to determine the aggregation rate constant. Besides just a decrease in the number of particles, an increase in particle size is also expected, or a shift in the peak of the particle size distributions towards larger sizes. The particle size is increasing because two or more smaller particles aggregate, to form a single larger particle, resulting in fewer particles in total, however the particles will have on average increased in size. The shift of the peak of the PSD is best represented in figure 4.10. It is clear that the peak of both the particle size distributions shifts to larger particle sizes as the time increases. The colour scale represents the number of particles for a particular size and time. The darker colours (black-red) represent a greater number of particles, and the lighter colours (blue-green) represent a lower numbers of particles. It shows a decrease in the number of particles and is equivalent to what was shown in figure 4.9. When comparing the two figures represented in figure 4.10, there a noticeable difference between them. The rate of the decrease in the number of particles, or as it is visualised in the plots, the rate at which the colours change from the dark to the light colours is much more rapid for the plot representing the shear rate of $60s^{-1}$ when compared to the change for a shear rate of $91s^{-1}$. This indicates that the decrease in the total number of particles occured more rapidly at a shear rate of $60s^{-1}$ than at a shear rate of $91s^{-1}$ and it offers an early indicator as to which shear rate will produce the highest aggregation rate constant, namely that of between 40 and $60s^{-1}$.

The moments for every number based particle size distribution as depicted in figure 4.9 were found. The zeroth moments, which represents the total particle numbers for each sampling time, are shown in figure 4.11 and 4.12. The zeroth moment is the sum of the total number of particles. It is convenient when comparing the data from different experiments to first normalise the total particle numbers with respect to the result from the t_0 sample. This is because the set of results with the largest rate of change in the zeroth moment, would imply the most rapid decrease in the number of particles and indicate a high aggregation rate. Though when calculating the aggregation rate constant the un-normalised data needs to be used as well since there is a dependence on the total number of particles. The greater the number of particles, the higher the chance of a possible collision to occur, as shown by the following equation for the aggregation rate

constant

$$\frac{dm_0}{dt} = -\frac{1}{2}\beta_0 m_0^2 \tag{5.1}$$

There will be an increase in the aggregation rate constant with an increase in the number of particles. The most important qualitative result to take from figure 4.11 and figure 4.12 is that the zeroth moment is decreasing with respect to time. This means that the total number of particles are decreasing, and this is an indication that aggregation is occurring, with an average decrease in the number of particles of 0.44 when comparing the total number of particles at the start and the end of an experiment. There are of course other reasons as to why a decrease may be observed, however, those can be discounted when additional data such as the concentration of calcium in the solution, is presented further on.

The volume of solids in solution is represented in numerous ways as shown in figure 4.13, 4.14 and 4.15. The total volume of solids should remain constant, unless the density of the particles changes as the particle increases in size. Very small changes may occur due to the growth of the crystalline bridge between collided particles. In general it is assumed not to be the case for calcium oxalate. Figure 4.13 is the volume of solid fraction data directly obtained from the Malvern Mastersizer. The results from all of the experiments indicate that total volume of the particles increases or remains the same for at least the first 30 minutes, whereupon, graphical analysis indicates there may be a decrease in the total volume. This is counter-intuitive to what is expected. The volume should remain relatively constant for the dura. Two ANOVA analysis tests were performed on the solids volume concentration data from the laser diffraction results. The ANOVA tests allow for us to test whether the means calculated for certain data sets remain constant, such as testing if the total volume of precipitates formed is constant between experiments. We perform an F-test on the data which allows us to evaluate the difference between an explained variance, such as the expected uncertainty in measurements, as compared to the unexplainable variance due to experimental error. The first test was on all the data, testing whether the volume remains constant for the duration of the experiment within a 2.5% statistical significance level. The results attained from the F-test at the 2.5% significance level for all the data are given in table 4.3. The F-statistic is 2.78 which is below the critical value of $F_{crit} = 2.99$. The p-value is 0.028, slightly above the 2.5% level. This implies that, at the 2.5% significance level, the solid volume fraction remains constant for the duration of the experiment, and the null hypothesis is excepted. A second F-test performed at the 5% significance level on the data for the first 30 minutes of the experiments, resulted in a F-statistic of 0.088 with a $F_{crit} = 3.40$ and a p-value of 0.91. What these results indicate is that the data is excellent up to the 30 minute mark, and

there is a decrease in the quality of the solids volume fraction data attained from the laser diffraction technique at the 50 and 60 minute samples. When considering all of the data for the full duration of each experiment, the null hypothesis still holds at the 2.5% significance level, and it can be assumed that the solids volume fraction data remains constant for the duration of the experiments.

The variability in the quality of the data for the volume of solids attained using laser diffraction techniques is assumed to depend significantly on the way the volume of solids is measured. The measurement technique relies on applying the Beer-Lambert law, and compares the amount of light energy from the laser before a sample is introduced into the sample cell to when a sample is tested. As explained in §2.5.1.1, the particles will absorb light energy, thereby reducing the number of photons which hit the detectors. The particles will also scatter the light, however, the Malvern Mastersizer has back scatter detectors to also measure the scattered light. This reduction in the light energy is correlated to the volume of solids in the solution. The Beer-Lambert law only applies to homogenous solutions, such as when it is typically used to find the absorbance of solutions. It can be assumed that the longer the experiments run, the less homogenous the solutions becomes, because of the effect of aggregation is one that results in larger particles being formed. At the latter stages of the experiment there will be fewer particles when compared to the beginning of the experiment, and ultimately this can be considered to be a less homogenous mixture. Lots of smaller particles can be considered to be more homogenous when compared to fewer larger particles if the volume is conserved. This can result in the what is observed in the solids volume fraction data, which is a small decrease in the volume of solids during the later stages of the experiment[1].

The aggregation rate constant was determined using the moment transformations of the the PSDs as described in §2.2.6. The aggregation rate constant is plotted against the shear rate which has been overaged over a small region within the reactor. The formulation for calculating the shear rate at any distance away from a oscillating grid was given in §2.3.4.1. The average shear rate was calculated over a region of 0.01 to 0.02 m above the grid. It is appropriate to estimate the shear rate in this manner because the turbulence generated in an OMR is considered to be isotropic and homogenous. This means that averaging the shear rate across a representative region within one of the regions through which a grid oscillates will provide a valid indication of the shear forces applied to the particles in solution. This region was considered large enough to be representative of the shear forces experienced by all of the particles suspended in the solution. At the

[1]The samples tested using the Malvern Mastersizer are not diluted. Hence it is not possible to increase the number of particles and obtain a more homogenous mixture for the latter parts of the experiment. All the samples also fall within the correct obscuration limits for the equipment.

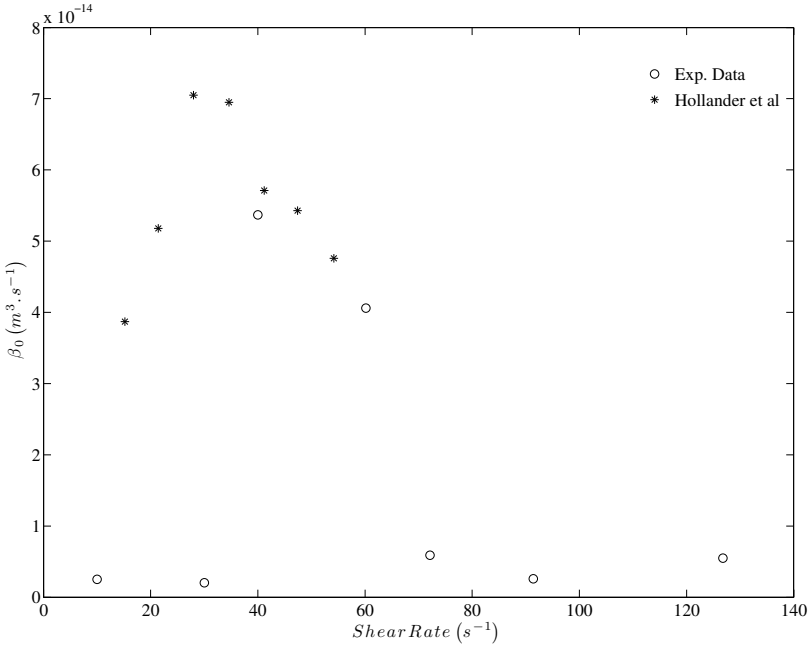

Figure 5.1: The aggregation rate constants found by Hollander et al. (2002) are compared to the current work.

lowest shear rates of $10s^{-1}$ and $30s^{-1}$, there is a minimum aggregation rate constant of $2.51\times10^{-15}m^3.s^{-1}$ and $2.04\times10^{-15}m^3.s^{-1}$ respectively. From $30s^{-1}$, the aggregation rate increases up to a maximum aggregation rate constant of between 5.37 and $4.04 \times 10^{-14}m^3.s^{-1}$. The increase in the aggregation rate constant is an expected phenomenon. The aggregation rate is directly proportional to the number of collisions for low energy inputs, up until a maximum aggregation rate is found. This is confirms to the trends found by Hollander et al. (2002) and Mumtaz and Hounslow (2000). All of the aggregation rate constants also fall within the range of values found in the literature as well.

The aggregation rate constant at a shear rate of $20s^{-1}$ does not appear to follow this trend. The calculation of the shear rates may not apply at low energy inputs and frequencies of oscillation. At lower energy inputs, it is possible that the type of turbulence generated inside the OMR is less homogenous and isotropic when compared to higher energy inputs. This could result in more localised conditions, and less frequent and effective collisions. The validity of this is difficult to ascertain until such a time as simulations or indirect measurements of the shear rates can be attained, however it should be considered that if in fact the data point was positioned at a shear rate of $10s^{-1}$ or even $15s^{-1}$, then it certainly would not be considered to be out of the norm.

As previously stated, a maximum aggregation rate constant is found between 5.37 and $4.04\times10^{-14}m^3.s^{-1}$ is attained at shear rates of between 40 and $60.1s^{-1}$. At shear rates

greater than $60.1s^{-1}$ there is a decrease in the aggregation rate constant. The existence of an energy input, which maximises the aggregation was theorised by Mumtaz et al. (1997). The maximum exists because the efficiency of the collisions remains constant at the lower shear rates, and therefore the aggregation rate will be directly proportional to the rate of collisions which is directly proportional to the shear rate, hence the aggregation rate is directly proportional to the shear rate as well. If the shear rate is increased past the point at which the maximum aggregation rate constant is observed, the efficiency of the collisions decreases as the shear forces becomes strong enough to disrupt the temporary bridges formed between collided particles. This theory was later confirmed in the experimental work of Mumtaz and Hounslow (2000) and Hollander et al. (2002), as well as Zauner and Jones (2000). At a shear rate of $25s^{-1}$, the lowest at which Mumtaz and Hounslow (2000) worked, they found the aggregation rate constant to be $\sim 3.00\times10^{-15}m^3.s^{-1}$. This increased to a maximum of $3.44\times10^{-14}m^3.s^{-1}$ at a shear rate of $307s^{-1}$, decreasing thereafter. Hollander et al. (2002) found that at a shear rate of $15s^{-1}$, β_0 was $4.02\times10^{-14}m^3.s^{-1}$ increasing to a maximum of $7.32\times10^{-14}m^3.s^{-1}$ at a shear rate of $28s^{-1}$. The same trend is observed in this work as well and the results are compared to literature in figures 5.1 and 5.2. Figure 5.1 shows the comparison between the current work and that of Hollander et al. (2002). The determined maximum aggregation rate constant does indeed overlap all of the results from Mumtaz and Hounslow (2000) as well as most of Hollander et al. (2002) albeit a few being slightly higher than that of the current work, and the work of Mumtaz and Hounslow (2000). The shear rates at which the maximum aggregation rate constant is achieved vary greatly between the various experimental setups. Most notable are those of Mumtaz and Hounslow (2000) which are shown in figure 5.2. Their shear rates are significantly greater than any other literature values and those of the current work. As mentioned previously, the calculation of the shear rate is at best only a reasonable estimation of the instantaneous shear forces experienced by the particles in solutions.

The hydrodynamic environment provided by operating these experiments within the OMR allow for the assumption that the data attained will be representative of the bulk. The energy dissipation within the OMR is the uniform throughout the volume. All the particles will experience similar shear forces because of the homogenous and isotropic turbulence produced in this reactor.

5.4 Concentration of Calcium in Solution

The concentration of calcium remaining in solution after precipitation has occurred is depicted in figure 4.19. The main purpose of performing this analysis was to make certain that the concentration remaining in solution is constant throughout the experiment as well

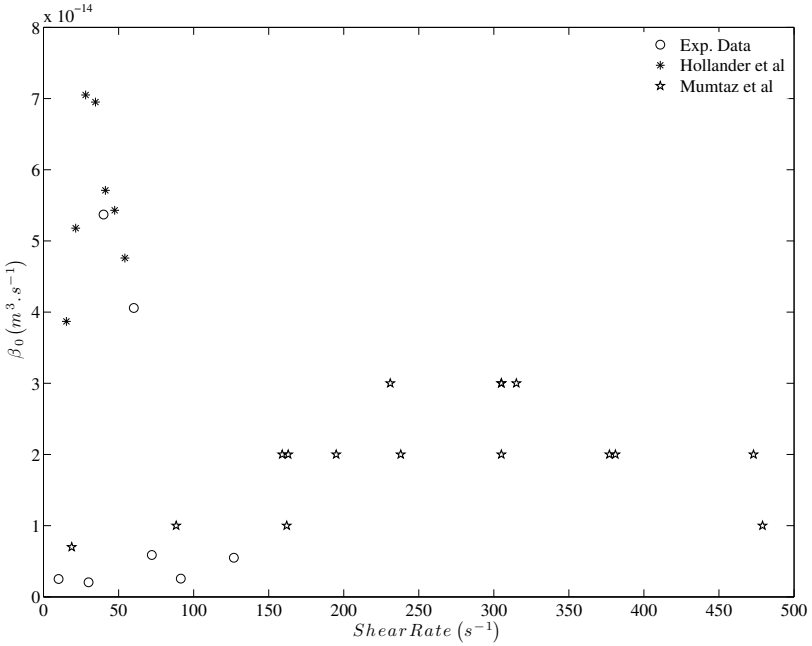

Figure 5.2: The aggregation rate constants found by Mumtaz and Hounslow (2000) as compared to Hollander et al. (2002) and the current work.

as perform a mass balance which was used to derive a volume of COM precipitated into the solution. This is what is observed from the data. The concentrations for 10, 20 and 60 minute samples remain constant for each experiment. It can therefore be assumed that if there is a decrease in the total number of particles numbers as indicated by the plots of m_0, it is as a results of aggregation and not dissolution, or other mechanisms. Secondly, any particle size increases must be due to aggregation and not growth via deposition, as that would result in a continuously decreasing calcium concentration. In the work by McComas and Rieman (1942), they determine the solubility of COM in water and NaCl solutions at 25 $^\circ$ C. It was found that in pure water, the solubility of COM was $4.55 \times 10^{-5} M$, or 6.64 mg/l. In an NaCl solutions of 0.1 M and 0.2 M ionic strengths, they found solubilities of $11.79 \times 10^{-5} M$ and $15.47 \times 10^{-5} M$ or 17.23 mg/l and $15.47 mg/l$. The lowest concentration of calcium after precipitation had occurred was 105.1 mg/l, with a mean concentration between all the experiments of $139.6 mg/l$. There is a significant amount of calcium ions, and hence oxalate ions, in the solution after precipitation. This is important, as it is necessary to build the bridges between aggregated particles, and the material needs to be deposited onto the aggregates.

5.4.1 Derived volume fraction

It was possible to estimate the volume of the solids precipitated in the form of calcium oxalate monohydrate by using a simple mass balance on the amount of dissolved calcium remaining in solution after precipitation has occurred, and the density of COM. The amount of calcium precipitated was determined by finding the difference in the initial concentration of calcium in the feed solutions with the calcium that remained in solution after precipitation had occurred. The calcium precipitated mostly in the form of COM, hence the density of COM was used to estimate the volume of solids. The value calculated from this method was 0.0053% ± 0.0011%. This results can be directly compared to the results obtained from the laser diffraction method. The average volume of solids fraction over all the data from the laser diffraction results was 0.0060% ± 0.0002%. The two means overlap, which gives a good indication that they are similar. Further statistical analysis reveals that at the 5% significance level, the p-value and T-value for a 2-sides t-test are 0.31 and 1.02 respectively. This indicates that there is no significant statistical difference between the volume of solids fraction from the laser diffraction results when compared to the derived volumes from the AAS data. The results of the volume of solids fraction attained from the laser diffraction and the derived volume from the AAS results can be considered equivalent. This result along with the previously conducted ANOVA analysis's, provide certainty in this data.

Chapter 6

Conclusions and Recommendations

6.1 Conclusions

The aggregation rate constant of calcium oxalate precipitates, in particular that of the monohydrate, was found while operating the oscillating multi-grid reactor at a range energy inputs (shear rates). This was done to study the effect of the energy input on the aggregation rate. It was concluded from the literature that energy input, turbulence and shear rates have significant effects on the rate of aggregation of particles. Such forces play a role in the collisions of two or more particles, as well as affecting the efficiency of those collisions and whether or not they will results in aggregates being successfully formed. The oscillating multi-grid reactor was chosen to perform these experiments in because of its ability to produce nearly homogenous and isotropic turbulence, which is considered ideal for studies into aggregation rates.

$$\frac{dm_0}{dt} = -\frac{1}{2}\beta_0 m_0^2 \tag{6.1}$$

The aggregation rate constant was determined by finding the moments transformations of particle size distributions and then performing an optimisation procedure to fit a size independent model, equation (6.1), to the derived experimental data. To do so, PSDs of samples were taken at 10 minute intervals for a total of 60 minutes. The PSDs were initially volume based and obtained using laser diffraction measurement techniques. The PSDs had to first be transformed to number based distributions, using the volume of solids concentration results. These figures were checked for consistency within the results and against atomic absorption data which allowed for estimation of the volume of calcium oxalate monohydrate precipitated. Excellent agreement was found between the two data sets, and this provided assurance that the data from both methods was accurate. Once the number based particle size distributions were obtained, the zeroth and third moments

were found. These moments represent the total number of particles and the total volume of particles respectively.

The zeroth moment shows a decrease in the total particle numbers with respect to increase time. This is entirely expected, as the mechanism of aggregation is the coming together of two or more particles, to form a single larger particle. It was also shown that the concentration of calcium remaining in solutions was constant for the duration of the experiment. This confirms that dissolution of calcium oxalate back into solution was not occurring, and reaffirming that aggregation must be the only mechanism for reducing the total number of particles. A narrowing of the particle size distribution as well a shift to larger particles with increasing time also indicated that aggregation was occurring. Early observations of the effects of the various shear rates on the rate of aggregation could be noticed in the PSD plots. The rate of decrease in the peak height of the PSDs which represent the shear rate that maximises the aggregation rate constant, were noticeably greater than those of higher shear rates.

Theory and literature indicates that there is an optimum shear rate (in a turbulent environment) which will maximise the aggregation rate. The lowest shear rates at which the OMR operated was of $10s^{-1}$. It resulted in an aggregation rate constant of $2.04\times10^{-15}m^3.s^{-1}$. β_0 increased to a maximum between $5.37\times10^{-14}m^3.s^{-1}$ and $4.04\times10^{-14}m^3.s^{-1}$ at shear rates of 40 and $60.1s^{-1}$ respectively. At shear rates above the maximum β_0 was found, the aggregation rate constant decreased. The trends observed are similar to what was found in the literature, as well as the aggregation rate constants falling within the range of most of the literature values.

Images of the crystals obtained from optical microscopy allowed it to be determined that most, if not all, of the crystals precipitated were that of COM. Weak aggregates of COM were also seen which are similar to that as depicted in literature. From the images, shape factors could be determined. This allowed for the verification of the typical shape factor of $\pi/6$ to be used when performing transformations from volume to number based distributions.

6.2 Recommendations

Calcium oxalate is a system which has been extensively studied because it is the main constituent of kidney stones and hence it is a medical problem for humans. It also forms a good test case for experiments which wish to measure growth and aggregation. Calcium oxalate does however have some draw backs. The most important of which is the various hydrations and the numerous morphologies of the salt. This problem was highlighted in §2. Experiments were conducted at the exact same operating conditions, except for changing

the method of agitation magnetic stirrer to a mechanical impeller. This change resulted in different hydrations of the salt being precipitated. Such a problem is a difficult one to resolve and understand. Numerous papers avoided this by seeding the system with pre-prepared COM crystals. The seeds would have to be prepared externally in another reactor and then introduced into the OMR The feasibility of seeding in the current experimental setup should be considered as a means to force the precipitation of only COM.

The experiments should be repeated on a second test system such as calcium carbonate. The results from the calcium oxalate experiments can be compared. If the same conclusions can be drawn from both, then there may be application of the results to other slightly soluble salts as well.

Sampling currently takes place from the base of the reactor. Since there is no agitation in the conical base of the reactor, there is potential for aggregation due to gravitational settling. It would be beneficial to be able to sample from between the oscillating grids, and obtain representative sample from within the zone wherein the aggregation is taking place.

Ideally, online sampling and measurements should take place. A continuous flow of sample from the reactor into the sample cell of the Malvern Mastersizer is possible. Samples can then be measured every 30 seconds, instead of every 10 minutes. This will improve the certainty of the calculated results. In addition to using laser diffraction, some experiments should be conducted using methods which produce number based particle size distributions, such as electrozone counting. This would be useful as the number based PSDs could be compared to the volume based PSDs obtained using laser diffraction, which have subsequently been transformed to number based PSDs. Even though the lower bounds of the different methods do not overlap completely, it would still be possible to directly compare the various bins which do overlap. This technique would give a good indication as to whether the transformation from a volume based PSD to a number based one can be trusted. Additionally, a method such as the FLS measurement which also uses obscuration measurement can be used to measure the total crystal volume(Brown and Felton 1985). This method does not simply use the Beer-Lambert law for measuring the total crystal volume and should result in improved results, especially when converting from a volume based distribution to a number based one.

In situ techniques to determine PSDs as well as directly observe numerous additional fluid properties can be implemented. The predictable flows within the OMR would allow for many additional fluid dynamic properties to be determined. From particle tracking and particle image velocimetry it would be possible to find the length of the biggest and smallest eddies, render the flow patterns and visualise the turbulence as well as measure the shear rates. This technique can provide instantaneous results without ever having the

need to take a physical sample.

Besides the potential issues with sampling methods, the way that the particle sizes are measured is also problematic. The manner in which the sample is introduced into the sample cell can cause different results to be attained. The sample are introduced into the sample cell by means of a low shear stirrer and pump. As mentioned in the materials and method, the stirrer is operated at 2500 rpm. It would be ideal to operate the stirrer at a much lower speed, however the dispersion of the sample into the sample cell becomes poor, and will not be representative of the actual sample. A comprehensive study was complete by Storti and Balsamo (2010), which solely considered how the operating conditions of the Malvern Mastersizer can effect the results. They used samples of both low and high-strength granular material, and tested the effect of pump, stirrer speeds and measurement durations among other variables. Of particular interest were their results on the effect of stirrer speed. At low speeds (below 1000 rpm) , they found a tendency for the method to be biased towards fine material, indicating sedimentation may be occurring. Between 1000 rpm and 2000 rpm there was a bias towards large particles, this indicates that the large particles are now suspended in the solution, however they are traveling slower than the fine particles. Above 2000 rpm the results are consistent, and reproducible, with only very negligible size reduction. Above 3000 rpm there is significant size reduction, and the operating conditions are now affecting the samples. Their study shows that it is possible to unknowingly affect the PSD results simply by operating the equipment at the incorrect speeds. Therefore, an initial study into the effect of the stirrer speed on the consistency and reliability of particle sizing data should be undertaken.

$$J_{ij}^{0} = 1.30 \left(\frac{\epsilon}{\nu}\right)^{1/2} (r_i + r_j)^3 n_i n_j. \tag{6.2}$$

The differences in the number of calculated particles between experimental runs is not always apparent, especially considering every effort was put in place to reduce the effect of environmental variables. The only data showing a significant difference was the $10s^{-1}$ shear rate experiment, the lowest shear rate at which the experiments were operated at. The initial particle numbers were significantly higher. Fortunately, in the theory of collisions, particles numbers are not raised to any power, equation (6.2), so any error here will not be compounded further.

Reference List

Babić-Ivančić, V., Füredi-Milhofer, H., Purgaric, B., Brnicevic, N., and Despotovic, Z.(1985). Precipitation of calcium oxalates from high ionic strength solutions. III: The influence of reactant concentrations on the properties of the precipitates. *Journal of Crystal Growth*, 71(3):655–663.

Bache, D. H. and Rasool, E.(1996). Measurement of the rate of energy dissipation around an oscillating grid by an energy balance approach. *The Chemical Engineering Journal and the Biochemical Engineering Journal*, 63(2):105–115.

Bache, D. H. and Rasool, E.(2001). Characteristics of turbulence in a multigrid mixer. *Chemical Engineering Journal*, 83(2):67–78.

Bramley, A. S., Hounslow, M. J., and Ryall, R. L.(1996). Aggregation During Precipitation from Solution: A Method for Extracting Rates from Experimental Data. *Journal of Colloid and Interface Science*, 183:155–165.

Bramley, A. S., Hounslow, M. J., and Ryall, R. L.(1997). Aggregation during precipitation from solution. Kinetics for calcium oxalate monohydrate. *Chemical Engineering Science*, 52(5):747–757.

Brečević, L.,Š krtić, D., and Garside, J.(1986). Transformation of calcium oxalate hydrates. *Journal of Crystal Growth*, 74(2):399–408.

Brown, D. and Felton, P.(1985). Direct measurement of concentration and size for particles of different shapes using laser light diffraction. *Chemical engineering research & design*, 63(2):125–132.

Brunk, B. K., Koch, D. L., and Lion, L. W.(1998). Direct numerical simulations of aggregation of monosized spherical particles in homogeneous isotropic turbulence. *Journal of Fluid Mechanics*, 371:81–107.

Collier, A. P. and Hounslow, M. J.(1999). Growth and aggregation rates for calcite and calcium oxalate monohydrate. *AIChE Journal*, 45(11):2298–2305.

de Silva, I. P. D. and Fernando, H. J. S.(1994). Oscillating grids as a source of nearly isotropic turbulence. *Physics of Fluids*, 6(7):2455–2464.

Derksen, J. and Van den Akker, H. E. A.(1999). Large eddy simulations on the flow driven by a rushton turbine. *AIChE Journal*, 45(2):209–221.

Derksen, J. J.(2012). Direct numerical simulations of aggregation of monosized spherical particles in homogeneous isotropic turbulence. *AIChE Journal*, 58(8):2589–2600.

Finlayson, B.(1978). Physicochemical aspects of urolithiasis. *Kidney Int*, 13(5):344–360.

Garside, J., Brečević, L., and Mullin, J.(1982). The effect of temperature on the precipitation of calcium oxalate. *Journal of Crystal Growth*, 57(2):233 – 240.

Hollander, E.(2002). *Shear Induced Agglomeration and Mixing*. PhD thesis, Delft University.

Hollander, E. D., Derksen, J. J., Kramer, H. J. M., and den Akker, H. E. A. V.(2002). Developing a non-intrusive measuring technique for determining orthokinetic agglomeration rate constants. *Measurement Science and Technology*, 13(5):807.

Hopfinger, E. J. and Toly, J.-A.(1976). Spatially decaying turbulence and its relation to mixing across density interfaces. *Journal of Fluid Mechanics*, 78(01):155–175.

Hounslow, M. J., Mumtaz, H. S., Collier, A. P., Barrick, J. P., and Bramley, A. S.(2001). A micro-mechanical model for the rate of aggregation during precipitation from solution. *Chemical Engineering Science*, 56:2543–2552.

Hounslow, M. J., Ryall, R. L., and Marshall, V. R.(1988). A Discretized Population Balance for Nucleation, Growth, and Aggregation. *AIChE Journal*, 34(11):1821–1832.

Jiang, Q. and Logan, B. E.(1991). Fractal dimensions of aggregates determined from steady-state size distributions. *Environmental Science and Technology*, 25(12):2031–2038.

Koh, P. T. L., Andrews, J. R. G., and Uhlherr, P. H. T.(1984). Flocculation in stired tanks. *Chemical Engineering Science*, 39(6):975–985.

Kusters, K. A.(1991). *The influence of turbulence on aggregation of small particles in agitated vessels*. PhD thesis, Technische Universiteit Eindhoven.

Kusters, K. A., Wijers, J. G., and Thoenes, D.(1997). Aggregation kinetics of small particles in agitated vessels. *Chemical Engineering Science*, 52(1):107–121.

Lindenberg, C., Schöll, J., Vicum, L., Mazzotti, M., and Brozio, J.(2008). Experimental characterization and multi-scale modeling of mixing in static mixers. *Chemical Engineering Science*, 63(16):4135–4149.

Madhrani, D. R.(2008). Experimental Investigation Of The Fluid Velocity Distribution In Stirred Tank Reactors Equipped With Retreat-Blade Impellers Using Laser Doppler Velocimetry. Master's thesis, New Jersey Institute of Technology.

McComas, W. H. and Rieman, W.(1942). The solubility of calcium oxalate monohydrate in pure water and various neutral salt solutions at 25°. *Journal of the American Chemical Society*, 64(12):2946–2947.

Mumtaz, H. S. and Hounslow, M. J.(2000). Aggregation during precipitation from solution: an experimental investigation using Poiseuille flow. *Chemical Engineering Science*, 55(23):5671–5681.

Mumtaz, H. S., Hounslow, M. J., Seaton, N. A., and Paterson, W. R.(1997). Orthokinetic Aggregation During Precipitation: A Computational Model for Calcium Oxalate Monohydrate. *Institution of Chemical Engineers*, 75:152–159.

Nancollas, G. and Gardner, G.(1974). Kinetics of crystal growth of calcium oxalate monohydrate. *Journal of Crystal Growth*, 21(2):267–276.

Nepf, H.(2002). Transport processes in the environment. *Massachusetts Institute of Technology: MIT OpenCouseWare*, http://ocw.mit.edu [accessed:20/06/2012].

Pope, S. B.(2001). *Turbulent Flows*. Cambridge University Press, United Kingdom.

Prien, E. L. and Jr., E. L. P.(1968). Composition and structure of urinary stone. *The American Journal of Medicine*, 45(5):654 – 672. Symposium on Stones.

Randolph, A. D. and Larson, M. A.(1988). *Theory of Particulate Processes*. Academic Press INC, 2 edition.

Rielly, C. D., Habib, M., and Sherlock, J.-P.(2007). Flow and Mixing Characteristics of a Retreat Curve Impeller in a Conical-Based Vessel. *Chemical Engineering Research and Design*, 85(7):953–962.

Rodriguez-Pascual(2013). Meetings.

Rouse, H. and Dodu, J.(1955). Diffusion turbulente {à} travers une discontinuit{é} de densit{é}. *La Houille Blanche*, 4:522–532.

Saffman, P. G. and Turner, J. S.(1956). On the collision of drops in turbulent clouds. *Journal of Fluid Mechanics*, 1:16–30.

Skrit, D., Furedi-Milhofer, H., and Markovic, M.(1987). Precipitation of calcium oxalates from high ionic strength solutions. V: The influence of precipitation conditions and some additives on the nucleating phase. *Journal of crystal growth*, 80(1):113–120.

Smoluchowski, M.(1918). Study of a Mathematical Theory for the Coagulation Kinetics of Colloidal Solutions. *Zeit. fur Physikalische Chemie*, 92(2).

Storti, F. and Balsamo, F.(2010). Particle size distributions by laser diffraction: Sensitivity of granular matter strength to analytical operating procedures. *Solid Earth*, 1(1):25–48.

Tambo, N. and Hozumi, H.(1979). Physical characteristics of flocs—II. Strength of floc. *Water Research*, 13(5):421–427.

Thompson, S. M. and Turner, J. S.(1975). Mixing across an interface due to turbulence generated by an oscillating grid. *Journal of Fluid Mechanics*, 67:349–368.

Thongboonkerd, V., Semangoen, T., and Chutipongtanate, S.(2006). Factors determining types and morphologies of calcium oxalate crystals: Molar concentrations, buffering, ph, stirring and temperature. *Clinica Chimica Acta*, 367(1–2):120–131.

Vermeulen, C. and Lyon, E.(1968). Mechanisms of genesis and growth of calculi. *The American Journal of Medicine*, 45(5):684 – 692. <ce:title>Symposium on Stones</ce:title>.

Zauner, R. and Jones, A. G.(2000). Determination of nucleation, growth, agglomeration and disruption kinetics from experimental precipitation data: the calcium oxalate system. *Chemical Engineering Science*, 55(19):4219 – 4232.

Appendix A

Risk Assessment

Standard Anglo Risk Matrix Loss Type (Additional 'Loss Types' may exist for an event; identify & rate accordingly)	Hazard Effect / Consequence (Where an event has more than one 'Loss Type', choose the 'Consequence' with the highest rating)				
	1 Insignificant	2 Minor	3 Moderate	4 Major	5 Catastrophic
(S/H) Harm to People (Safety / Health)	First aid case / Exposure to minor health risk	Medical treatment / Exposure to major health risk	Loss time injury / Reversible impact on health	Single fatality or loss of quality of life / Irreversible impact on health	Multiple fatalities / Impact on health ultimately fatal
(EI) Environmental Impact	Minimal environmental harm - L1 incident	Material environmental harm - L2 incident remediable short term	Serious environmental harm - L2 incident remediable within LOM	Major environmental harm - L2 incident remediable post LOM	Extreme environmental harm - L3 incident irreversible
(BI/MD) Business Disruption / Material Damage & Other Consequential Losses	No disruption to operation / R500k to less than R5m	Brief disruption to operation / R5m to less than R50m	Partial shutdown / R50m to less than R500m	Partial loss of operation R500m to less than R5bn	Substantial or total loss of R5bn and more
(L&R) Legal & Regulatory	Low level legal issue	Minor legal issue; non compliance and breaches of the law	Serious breach of law; investigation/report to authority, prosecution and/or moderate penalty possible	Major breech of the law; considerable prosecution and penalties	Very considerable penalties & prosecutions. Multiple law suits & jail terms
(R/S/C) Impact on Reputation/Social/Community	Slight impact - public awareness may exist but no public concern	Limited impact - local public concern	Considerable impact - regional public concern	National impact - national public concern	International impact - international public attention

Likelihood	Examples (Consider near-hits as well as actual events)	Risk Rating				
5 Almost Certain	The unwanted event has occurred frequently; occurs in order of one or more times per year & is likely to reoccur within 1 year	11 (M)	16 (H)	20 (H)	23 (Ex)	25 (Ex)
4 Likely	The unwanted event has occurred infrequently; occurs in order of less than once per year & is likely to re-occur within 5 years	7 (M)	12 (M)	17 (H)	21 (Ex)	24 (Ex)
3 Possible	The unwanted event could well have occurred in the business at some point within 10 years	4 (L)	8 (M)	13 (H)	18 (H)	22 (Ex)
2 Unlikely	The unwanted event has happened in the business at some time; or could happen within 20 years	2 (L)	5 (L)	9 (M)	14 (H)	19 (H)
1 Rare	The unwanted event has never been known to occur in the business; or is highly unlikely that it could ever occur beyond 20 years	1 (L)	3 (L)	6 (M)	10 (M)	15 (H)

No	Sub System	Hazard -"What if"	Risk	Current Controls	Loss Type	C	L	R
1	Operating a 10 Liter OMR in the CPU Lab	Damaged hoses may cause spills or leaks. Potential risk of slipping and falling.	Injury to head and body	1. PPE (Lab shoes, coat, gloves, glasses) 2. Check for damaged hoses. 3. Apply fastening clamps to hose ends	S/H	2	2	5(L)
2	Taking of samples of solution.	Potential risk of slipping and falling.	Injury to head and body	1. PPE (Lab shoes, coat, gloves, glasses) 2. Minimize the number of samples to be taken.	S/H	2	2	5(L)
3	Transporting 20 liter waste buckets	Spillage can easily occur. Potential risk of slipping and falling.	Injury to head and body	1. PPE (Lab shoes, coat, gloves, glasses) 2. Use two hands to carry the bucket. 3. Do not fill the bucket above 50%.	S/H	2	2	5(L)
4	Contact with moving parts	Hands, gloves caught in moving parts	Injury to body or hands	1. PPE (Lab shoes, coat, glasses, not gloves) 2. Do not wear gloves near moving parts. 3. Barrier around moving parts. 4. emergency shut off switches.	S/H	3	1	6(M)

Table A.1: Risk assessment conducted according to the Anglo risk matrix.

Appendix B

Uncertainty Calculations for the AAS Data.

The uncertainty of the AAS results is determined by the calibration of the equipment against standards to form a standard curve. Each result is given with an RSD value, an uncertainty in each measurement. This uncertainty can be propagated to the calculation of the mean and is a better estimation of the error due to the measurement instead of finding the variance in the mean. If the error in each measurement is defined as δx_i where for n measurements, i is of the range $1 \leq i \leq n$ and $i \in \mathbb{N}$, then the measurement error in the mean can be found

$$\begin{aligned} \delta\bar{x} &= \frac{1}{n}\sum_{i=1}^{n}\delta x_i \\ &= \frac{1}{n}\left(\delta x_1 + \delta x_2 + ... + \delta x_{n-1} + \delta x_n\right). \end{aligned}$$

Appendix C

Numerical Algorithms for Moment Transformations and Optimization

Two numerical algorithms are shown in tables C.1 and C.2. The first algorithm is one which processes the data from the Malvern Mastersizer, and transforms the volume based particles size distributions to a number based distribution, and then the moments (zeroth, to the fourth) for each particle size distribution is found. The moments are then stored and will be used in the next algorithm. The optimization algorithm for finding the aggregation rate constant which best fits the experimental data is shown in table C.2. aggregation rate constants varying from $\beta_0 = 1 \times 10^{-18}$to 1×10^{-10}, are tested, and the model is used to predict the values of m_0. For each β_0 tested, an optimization function is used to determine how well the resulting curve fitted the data. This is typically known as the cost function. In this case, the cost function, and it is the function to be minimised.

$$\min[C_i = \sum_{1}^{k}(E(x) - O(x))^2].$$

Where i represents the i'th value of β_0 tested, k, is the number of experimental data point, *E(x)* and *O(x)* are the expected values obtained from the model and the observed values respectively. The minimum value for C is found and it can be related back to the optimal aggregation rate constant for a given experiment.

Algorithm C.1 Moment transformation from volume based particle size distributions.

```
%%required inputs and variiables to set up%%
%conc (given in %)  ie remember to divide by 100
%particle_sizes_mic (covernt into L_bar and delta L)
%results (given as %)
%sample volume
%water volume,    sample+water = cell volume

runs=1; %number of repeats at the same shear rate
data(1:63,1:6,1) = run1(1:63,1:6); %experimental data
%data(1:63,1:6,2) = run2(1:63,1:6);
%data(1:63,1:6,3) = run3(1:63,1:6);
particle_sizes=particle_sizes_mic*(1e-6);
delta_L = particle_sizes(2:64)-particle_sizes(1:63); %bin sizes
L_bar = (particle_sizes(2:64)+particle_sizes(1:63))/2; %bin centers
sample_vol=0.05.*ones(runs,6); %samle volumes
cell_vol=sample_vol;%+water_vol;
conc_malvern=conc/100; %convert to decimal
shape = pi/6; %shape factor for a sphere
vol_solids = cell_vol.*conc_malvern;
dt=600; %time between samples
for j=1:runs

    m_0(j,1:6)=0;m_1(j,1:6)=0;m_2(j,1:6)=0;m_3(j,1:6)=0;
    m_4(j,1:6)=0; #initialise variables for the moments
    for i = 1:63
        N(i,:,j)=data(i,:,j)/100.*vol_solids(j,:)...
                 .../shape./(L_bar(i).^3)./cell_vol(j,:);
        n(i,:,j)=N(i,:,j)/delta_L(i);
        m_0(j,:)=m_0(j,:)+(L_bar(i).^0)*n(i,:,j).*delta_L(i);
                 %calculation of the moments
        m_1(j,:)=m_1(j,:)+(L_bar(i).^1)*n(i,:,j).*delta_L(i);
        m_2(j,:)=m_2(j,:)+(L_bar(i).^2)*n(i,:,j).*delta_L(i);
        m_3(j,:)=m_3(j,:)+(L_bar(i).^3)*n(i,:,j).*delta_L(i);
        m_4(j,:)=m_4(j,:)+(L_bar(i).^4)*n(i,:,j).*delta_L(i);
    end
    store(j,1:6)=m_0(j,1:6); %store each moment
    store_m3(j,1:6)=m_3(j,1:6); %store the third moment.
end
```

Algorithm C.2 Optimization scheme to determine the value of β_0 which minimises the distance between the observed and expected values of a size-independent model

```
%input will be m_0, initial value = m_0(0), %set up time variables
delta_t=0.5; time=[10:10:60]; counter=1;
m_0_store=(store(3,1:6)); %transfer experimental data
mean_m_0=mean(m_0_store); middle=median(m_0_store);
          for i=1:6 %for loop to remove outliers
              if m_0_store(i)>(middle+middle*1e2)
                  time(i)=[];
                  m_0_store(i)=[];
                  i=i-1;
              else if m_0_store(i)<(middle-middle*1e2)
                  time(i)=[];
                  m_0_store(i)=[];
                  i=i-1;
                  end
              end
           end
time_to_run=max(time)-min(time); %update the time to run
num_steps=time_to_run/delta_t; %number of iterations
m_0_predict=zeros(1,(max(time)-min(time))/delta_t);
m_0_predict(1)=m_0_store(1);
for t=-18:0.01:-10  %test aggregation rates from 1e-18 to 1e-10
         initial_beta_0=10^(t);
         for i=2:num_steps
         m_0_predict(i)=m_0_predict(i-1)-(1/2)*initial_beta_0...
                  ...*delta_t*m_0_predict(i-1)*m_0_predict(i-1);
         end
         m_0_opt(1)=m_0_predict(1);
         for i=2:length(time)
         m_0_opt(i)=m_0_predict(1,(time(i)-time(1))/delta_t);
         end %classical cost function
         cost(counter)=sum(((m_0_opt-m_0_store).*(m_0_opt-m_0_store)));
         beta_storage(counter)=initial_beta_0;
         if cost(counter)==inf
             break
         end
         counter=counter+1; %test the next value
end
[Value,Index]=min(cost); %find the smallest cost (optimal beta_0)
initial_beta_0=beta_storage(Index)
         for i=2:num_steps %use it again to define the curve
         m_0_predict(i)=m_0_predict(i-1)-(1/2)*initial_beta_0...
                  ...*delta_t*m_0_predict(i-1)*m_0_predict(i-1);
         end
```

Appendix D

Proof of $\pi/6$ Shape Factor

The over estimation of the volume of a particle can be taken into account by applying a shape factor. The most typical of which, is that for comparing the volume of a sphere to a cube which would encase a sphere. The relationship between the two forms is a factor of $\pi/6$. The proof is shown below.

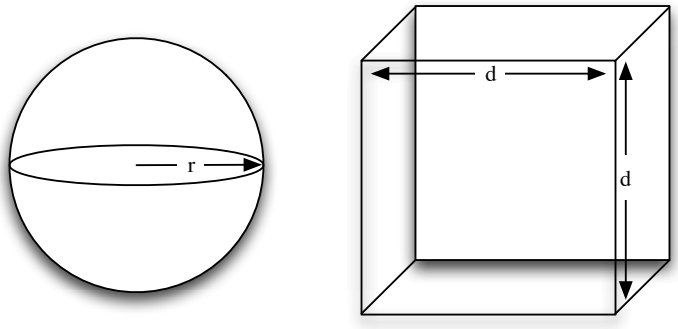

Figure D.1: Sphere of radius r with a cube with diameter of $d = 2r$. The sphere would be completely contained within the cube.

In figure D.1, is a sphere of radius r. The smallest cube which the sphere could be completely contained within has to have sides of length no less than $d = 2r$. The volume of the sphere is

$$\begin{aligned} v_{sphere} &= \frac{4}{3}\pi r^3 \\ &= \frac{4}{3}\pi\left(\frac{d}{2}\right)^3 \\ &= \frac{4}{3\cdot 8}\pi d^3 \\ &= \frac{\pi}{6}d^3. \end{aligned}$$

The volume of the cube is simply

$$v_{cube} = d^3.$$

Therefor the volume of the sphere compared to the volume of the cube is,

$$\begin{aligned} \frac{v_{sphere}}{v_{cube}} &= \frac{\frac{\pi}{6}d^3}{d^3} \\ &= \frac{\pi}{6}. \end{aligned}$$

The shape factor is $\pi/6$.